Structure and thermomechanics of selective laser melted nickel-titanium

Inauguraldissertation

zur

Erlangung der Würde eines Doktors der Philosophie
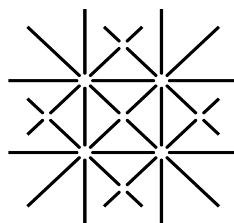
vorgelegt der

Philosophisch-Naturwissenschaftlichen Fakultät

der Universität Basel

von

Anna Therese Bormann

aus Deutschland

UNI
BASEL

Basel, 2015

Genehmigt von der Philosophisch-Naturwissenschaftlichen Fakultät auf Antrag von:

Prof. Dr. Bert Müller, Fakultätsverantwortlicher
Prof. Dr. Thomas Jung, Korreferent
Prof. Dr. Martin Bram, Korreferent

Basel, den 17. September 2013

Prof. Dr. Jörg Schibler, Dekan

Contents

Summary

NiTi has been established for applications in load-bearing implants due to its mechanical properties, which mimic the characteristics of bone better than any other known biocompatible metal or metallic alloy. Further, NiTi is well known for pseudoelasticity and pseudoplasticity, i.e. the possibility for shape recovery after deformation. Both macroscopic effects are based on a thermoelastic martensitic phase transformation, i. e. rearrangement of atoms on the sub-nanometer scale. For load-bearing implants, the appropriate mechanical stimulation of bony tissue enhances osseointegration. NiTi scaffolds exhibiting pseudoelasticity allow the cyclic mechanical stimulation of tissue in its proximity, as an induced deformation is recovered if the stress is removed. This is hypothesized to lead to improved bone ingrowth, better bonding between implant and surrounding tissue and ultimately to an enhanced implant performance. As the additive manufacturing technique of selective laser melting (SLM) allows the straightforward fabrication of dense as well as porous NiTi constructs, this work deals with SLM-processing of the NiTi alloy regarding scaffolds as medical implants.

The first part of the thesis is concerned with the impact of processing parameters onto the resulting material properties, because selective laser melting is known to alter material characteristics in an anisotropic manner. In dense parts, variation of the processing parameters shifted the phase transformation temperatures of up to 50 K. This shift resulted from preferential nickel evaporation and allowed the fabrication of parts with pseudoelastic and with pseudoplastic properties at body temperature from the same lot of powder.

While the scanning speed determined the amount of lost Ni, the laser power applied was crucial for the resulting microstructure. The grain size increased about a factor of 3 and the grain width increased about a factor of 10 with raised applied laser power. Also the crystallographic texture, i.e. a preferred <111> crystal orientation in the building direction, increased. The grain size distribution changed thereby from

unimodal to bimodal. The enlargement of grains > 40 m and the bi-modal grain size ditribution indicateded secondary grain growth, i.e. Ostwald-ripening, during SLM fabrication. In case of the unimodally distributed grain sizes, the microstructure was in accordance to the ASTM standard F2063-05 regarding medical applications of NiTi alloys.

The second part of the thesis deals with the characterization of SLM-built porous NiTi scaffolds. The scaffolds morphology showed deviations from the intended design, as excess material was accumulated particularly underneath the struts. This led to increased material volume and decreased porosity within the scaffold. The actual porosity of the investigated specimen corresponded to about 76 %, while an open pore volume of about 84 % was aspired.

As the scaffolds are intended to mechanically stimulate surrounding tissue by mechanical micro-motions, the local deformations upon uniaxial scaffold compression were analyzed by synchrotron radiation based micro computed tomography in combination with three-dimensional non-rigid registration. Displacements and strains within the scaffold were identified on the micrometer scale and visualized. Compressive and tensile strains occurred simultaneously during scaffold deformation. Uniaxial compression of 6 % led to local compressive and tensile strains of up to 15 %. In addition, an in-situ SRμCT setup was applied to study the shape recovery process of the pseudoplastic scaffold during heating. The inhomogeneous shape recovery process starting on the scaffolds' bottom, proceeding up towards the top and terminating at the periphery of the scaffold was demonstrated.

List of Publications

T. Bormann, B. Müller, M. Schinhammer, A. Kessler, P. Thalmann, M. de Wild. Microstructure of selective laser melted nickeltitanium. Materials Chracterization 94 (2014) 189-202.

W. Hoffmann, T. Bormann, A. Rossi, B. Müller, R. Schumacher, I. Martin, M. de Wild, D. Wendt. Rapid prototyped porous NiTi scaffolds as bone substitutes. Journal of Tissue Engineering 5 (2014) 1-14.

T. Bormann, F. Beckmann, M. Schinhammer, H. Deyhle, M. de Wild, B. Müller. Assessing the grain structure of highly X-ray absorbing metallic alloys. International Journal of Materials Research 105(7) (2014) 692-701.

M. de Wild, F. Meier, T. Bormann, C. Howald, B. Müller. Damping of selective-laser-melted NiTi for medical implants. Journal of Materials Engineering and Performance 23(7) (2014) 2614-2619.

T. Bormann, G. Schulz, H. Deyhle, F. Beckmann, M. de Wild, J. Küffer, C. Münch, W. Hoffmann, B. Müller. Combining micro computed tomography and three-dimensional registration to evaluate local strains in shape memory scaffolds. Acta Biomaterialia 10(2) (2014) 1024-1034.

T. Bormann, M. de Wild, F. Beckmann, B. Müller. Assessing the morphology of selective laser melted NiTi-scaffolds for a three-dimensional quantification of the one-way shape memory effect. Proceedings of SPIE 8689 (2013) 868914.

T. Bormann, R. Schumacher, B. Müller, M. de Wild. Controlling Mechanical Properties of NiTi Scaffolds built by Selective Laser Melting. Biomedizinische Technik 57 (1) (2012) 568.

T. Bormann, R. Schumacher, B. Müller, M. Mertmann, M. de Wild. Tailoring selective laser melting process parameters for NiTi implants. Journal of Materials Engineering and Performance 21(12) (2012) 2519-2524.

B. Müller, H. Deyhle, S. Lang, G. Schulz, T. Bormann, F. Fierz, S. Hieber. Three-dimensional registration of tomography data for quantification in biomaterials science. International Journal of Materials Research 103(2) (2012) 242-249.

Y.-C. Brogle-Kim, H. Deyhle, B. Müller, G. Schulz, T. Bormann, F. Beckmann, K. Jäger. Evaluation of oral scanning in comparison to impression using three-dimensional registration. Proceedings of SPIE 8506 (2012) 85061R.

T. Bormann, R. Schumacher, B. Müller, M. de Wild. From powder to complex-shaped NiTi structures by selective laser melting. Proceedings Euro PM2012 Volume 1 (2012) 193-197.

T. Bormann, R. Schumacher, B. Müller, M. de Wild. Crystallographic phases of NiTi scaffolds fabricated by selective laser melting. European Cells and Materials 22 (2011) 14

T. Bormann, S. Friess, M. de Wild, R. Schumacher, G. Schulz, B. Müller. Determination of strain fields in porous shape memory alloys using micro computed tomography. Proceedings of SPIE 7804 (2010) 78041M.

T. Bormann, R. Schumacher, B. Müller, M. Mertmann, U. Pieles, M. de Wild. Properties of NiTi-structures fabricated by selective laser melting. European Cells and Materials 20 (2010) 13.

B. Müller, G. Schulz, J. Herzen, S. Mushkolaj, T. Bormann, F. Beckmann, K. Püschel. Morphology of urethral tissues. Proceedings of SPIE 7804 (2010) 78040D.

1 Introduction

The shape memory alloy NiTi is widely used as medical implant within the human body. Though the most prominent example for a NiTi implant is the self-expanding stent, the alloy has been established for the use in load-bearing implants recently [1, 2]. Reason is that in comparison to other biocompatible metals or alloys, the mechanical properties of NiTi are considerably closer to that of bone [3]. The pseudoelastic properties of NiTi allow for a recovery of deformations of up to about 8 %, while bone can recover more than 1 % strain [1]. The elastic modulus of bulk-NiTi in its martensitic state is referred to reach down to values of about 20 GPa [4], which is close to the elastic modulus of bone of about 18 GPa [5]. In addition, the damping capacity of NiTi is beneficial for shock absorption in bone implants [6].

These observed - for a metal rather unusual - properties arise from a thermoelastic martensitic phase transformation between two distinct crystalline phases [7]. The high-temperature austenite phase has a body-centered cubic crystalline lattice (B2) while the low-temperature phase, the martensite, is monoclinic (B19'). Upon cooling, the austenitic phase starts to transform into martensite at the martensite start temperature (M_s). During further cooling the more and more austenite is transformed into martensite, until at the martensite finish temperature (M_f) the crystalline lattice is completely martensitic. Upon heating, the reverse transformation from martensite to austenite starts at the austenite start temperature (A_s) and terminates at the austenite finish temperature (A_f). The two transformation ranges are divided by a temperature hysteresis, as the energy for nucleation and for compensation of the elastic deformation is provided by sufficient undercooling of the material. Transformation from one phase into the other takes place without diffusion, by a coordinated shearing movement of the atoms within the crystalline lattice. Shearing of atoms involves high strains. In shape memory alloys, these strains are compensated by twinning of

the martensite phase and by self-accumulation of favored martensite variants. As these mechanisms for counterbalancing strains ideally do not involve irreversible lattice defects, the phase transformation is reversible, i.e. thermoelastic.

The mentioned phenomenon on the nanometer-scale or even below determines the observed macroscopic effects of pseudoelasticity and the one- or two-way shape memory effect: Is the material in the austenitic phase and the temperature above A_f, pseudoelasticity, i.e. the shape recovery of up to 8 % strain upon stress-relive occurs: Upon loading, stress-induced martensite is formed within the austenitic matrix. The formation of martensite is energetically less expensive than the creation or movement of lattice defects, such as dislocations. If the stress is relieved, the martensitic phase is reversed into the austenitic one, because the martensite is instable at temperatures above A_f.

Is the material in the martensitic phase, pseudoplasticity also known as the one-way shape memory effect occurs. An induced deformation leads now to the movement of martensite twin boundaries, which again is energetically favored over the creation and movement of lattice defects. The deformation persists, until the element is heated into the temperature range above A_f. As during the phase transformation the initial crystalline lattice is restored, the macroscopic deformation is recovered as well.

During the two-way shape memory effect, the NiTi element appears in distinct macroscopic shapes depending on the temperature. The low-temperature macroscopic shape has to be induced by thermo-mechanical training of the element. During this procedure, irreversible lattice defects or precipitates are induced in the NiTi-matrix. These defects favor the formation of specifically oriented martensite variants. These oriented, de-twinned martensite variants result in the deformation of the material in the low temperature-regime during repeated thermal cycling. During each heating-cycle above A_f, the crystalline lattice is transformed into austenite, which in turn restores the original macroscopic shape. The low elastic moduli, which are referred to broad ranges of 55 to 80 GPa for the austenite phase [8] and of 20 and 50 GPa for the martensite phase [4], are caused by the induction of stress-induced martensite and movement of twin boundaries, respectively. Both mechanisms can occur prior to the actual plateau-regions

in the stress-strain curve, which lowers the slope during actual 'elastic' deformation [9]. As these mechanisms cannot be considered as actual elastic ones, the theoretical elastic modulus of the austenite and martensite phases in NiTi differs from the elastic modulus derived from static mechanical testing [4, 10]. The temperature for the phase transformation ranges from -100 to about +100 °C [11]. It can be adjusted to a desired temperature range via the Ni/Ti-ratio in the NiTi-matrix. As a rough estimate, the transition temperatures shift about 10 K as result of changes in the NiTi-ration of about 0.1 at.% [12]. As the body temperature lies within the temperature for the phase transformation, medical devices and implants take advantage of the above-mentioned effects [11].

Selective laser melting (SLM) is an additive manufacturing technique, allowing a wide geometrical freedom for the fabrication of sound elements from loose powder. For SLM fabrication a computer-aided design (CAD) model of the intended part is virtually cut into horizontal slices of typically 30 - 100 m thickness. During the manufacturing process, a focused laser beam transmits the contour information of each virtual slice into the bed of metallic powder, which locally melts and solidifies. After scanning of one slice, the building platform is lowered about the slice thickness and re-coated by powder. The scanning of each subsequent slice by the laser and re-coating of the platform is repeated until all slices have been processed. A more detailed description of the SLM fabrication process can be found in literature, e.g. [13-15]. Additive manufacturing techniques like SLM allow for an efficient manufacturing of patient-specific implants according to the three-dimensional patient data acquired via computed or magnetic resonance tomography [16, 17]. Furthermore, the techniques are outstanding to create porous, complex-shaped constructs, hard or even impossible to manufacture by conventional techniques such as machining or casting [13, 15, 18]. Still, as selective laser melting is based on the local melting of powder, high temperatures and the associated thermal gradients lead to stresses during fabrication [19]. As the parts are built up slice-wise from the bottom to the top, an anisotropic microstructure with elongated grains in the building direction develops due to epitaxial grain growth from the preceding, partially re-molten slice [19-22]. The continuous exposure to heating for the time of the production can fur-

ther lead to segregation and the formation of precipitates within the microstructure [19, 23]. Also, the mechanical properties of SLM-built parts are known to differ along the individual directions with respect to the building process [22]. For building an element with SLM, the processing parameters have to be selected carefully. This includes a multitude of parameters, namely the slice thickness, laser power, scanning speed and geometrical arrangement of the laser paths, which have to be optimized according to the specific material needs. Furthermore, the condition of the powder plays an important role regarding the properties of resultant parts.

NiTi as shape memory alloy, i.e. with functional pseudoelastic or pseudoplastic properties, is only stable in a narrow range near the equiatomic composition [7, 8]. On the Ni-rich side, the phase transformation temperatures strongly depend on the Ni-content [24]. As impurities such as Ti_4Ni_2O and TiC as well as precipitates like for example Ni_4Ti_3 shift the atomic composition of the binary NiTi-matrix, they have great impact on the resulting phase transformation behavior [24, 25]. Additionally, internal stresses resulting for example from coherency fields around Ni-rich precipitates, impact the phase transformation and therefore the pseudoelastic or pseudoplastic response [26]. Selective laser melting, which involves local melting and solidification can therefore considerably impact the functional properties of NiTi [27, 28]. SLM processing of NiTi has recently gained attention with respect to the application as actuator within micro-electromechanics or micro-fluidics [28, 29] and especially regarding medical applications [30, 31]. Porous NiTi scaffolds combine the remarkable properties of pseudoelasticity, pseudoplasticity or the high damping capacity with a three-dimensional construct suitable for cell or tissue ingrowth [3]. The SLM fabrication of porous NiTi scaffolds allows further to tailor properties regarding to the biomechanical needs. By controlling the scaffolds architecture, for example via the strut size, pore geometry, pore size or pore size distribution, scaffolds can be adapted to the anisotropic and mechanical properties of hard tissue [13, 15]. If cells within a scaffold are mechanically stimulated, the response, like for example cell differentiation and proliferation, depends on the magnitude of the stimulus [32-34]. For load-bearing implants, the appropriate mechanical stimulation gives rise to enhanced osseointegration [35-37].

NiTi scaffolds exhibiting pseudoelasticity allow the cyclic mechanical stimulation of cells and tissue in its proximity [38], because the induced deformation is recovered upon unloading. This was hypothesized to lead to improved bone ingrowth and better bonding between implant and surrounding tissue. Such NiTi scaffolds can be beneficial for example for treating large bone defects.

As the remarkable properties of NiTi in combination with a complex, tailor made scaffold architectures promises sophisticated porous bone implants with an enhanced performance, this work deals with the characterization of dense and porous NiTi-parts processed by selective laser melting.

The first part of this work *Processing of NiTi by selective laser melting* investigates the impact of the fabrication process onto the material properties and microstructure. As a focused laser beam melts the powder locally, significant effects on several length-scales can alter the material within the fabrication process. This holds especially true in case of NiTi, where just a slight shift in the atomic composition can lead to strong deviations in the intended material properties.

The first chapter *Tailoring selective laser melting process parameters for NiTi implants* deals with the impact of a varied energy density during SLM processing. It further investigates the effects of different annealing procedures subsequent to the fabrication onto the phase transformation and the resulting crystalline structure. The microstructure and the crystalline phases of as-built and annealed specimens were investigated by light optical microscopy and X-ray diffraction, respectively. The pseudoelastic behavior was demonstrated in static tensile tests. Specimen production and post-processing as well as all measurements and data analysis within this chapter were carried out by the applicant. As starting point for the specimen fabrication served SLM process parameter sets, which were evaluated during a semester-project supervised by R. Schumacher at the University of Applied Sciences Northwestern Switzerland, School of Life Sciences.

As a significant effect of the processing parameters onto the resulting material properties was found, the second chapter *Microstructure of selective laser melted NiTi* focuses on the microstructural evolution of NiTi during the SLM processing in more detail. Extended sets of process parameters were applied, while in particular laser power and scan-

ning speed were examined. Metallographic investigations were supplemented by electron backscatter diffraction (EBSD), which revealed the crystallographic orientation of individual grains. EBSD was carried out at the ETH Zürich in cooperation with P. Uggowitzer and M. Schinhammer. The detailed analysis of the light optical micrographs gave insight into the microstructural evolution during SLM. Metallographic analysis including specimen preparation was accomplished by the applicant.

The second part of this work *Analysis of porous NiTi scaffolds by micro-computed tomography* is concerned with the three-dimensional analysis of porous NiTi scaffolds applying synchrotron radiation-based micro-computed tomography (SRμCT)and three-dimensional data registration. The scaffolds were prepared by SLM by the applicant for the purpose of cell experiments involving the mechanical scaffold stimulation in a compressive bioreactor system.

In the third chapter *Assessing the morphology of selective laser melted NiTi-scaffolds for a three-dimensional quantification of the one-way shape memory effect*, the scaffold's morphology was assed on the micrometer scale. To do so, established tools for the quantification of the geometrical quality in comparison with the initial CAD-design were applied. The tools were extended to asses the geometry at individual locations within the three dimensional scaffold by the applicant, as the SLM process leads to orientation dependent deviations of the real, materialized part from the intended design. In order to investigate the shape recovery process of a pseudoplastic scaffold, SRμCT data was acquired continuously during the heating-induced shape recovery. The SRμCT data involving an in-situ heating stage was acquired cooperation with F. Beckmann from the Helmholtz-Zentrum Geesthacht at the HASYLAB, DESY in Hamburg, Germany. F. Beckmann also reconstructed the individual three-dimensional data sets out of the continuously collected radiographs. The geometrical parameters extracted from affine registration of the CT-data sets with the initial CAD-file for scaffold fabrication were then applied to relate the integral scaffold height change during heating to seven data sets gained from the variable-temperature SRμCT. As the data was accompanied by artifacts such as blurring due to the continuous data acquisition, a method for consistent segmentation of the individual data sets was

established prior to the actual data analysis. Both was accomplished by the applicant.

The fourth chapter *Combining micro computed tomography and three-dimensional registration to evaluate local strains in shape memory scaffolds* evaluates the local effects during scaffold compression and the shape recovery process. The datasets from the variable temperature SRμCT were analyzed applying non-rigid three-dimensional registration. The tools for non-rigid three-dimensional data registration have been established at the Biomaterials Science Center. Still, different data sets for registration require specific pre- and post processing procedures, which have to be newly generated or adapted according to the peculiarities of the analyzed data and the research questions to be solved. These procedures were established by the applicant in collaboration with G. Schulz and H. Deyhle. From the registration, the local displacement and strain fields were derived individually for (i) the scaffold deformation and (ii) during the shape recovery process upon compression and heating, respectively. The strain field was derived by a software tool developed by G. Schulz. As the scaffold is built up from repeated unit cells, which all behave slightly different due to the geometrical deviations, average strain and displacement fields for a single scaffold unit cell were derived by the applicant. The resulting strain fields were compared to finite element modeling (FEM) applying the initial CAD-designed scaffold design. FEM analysis was conducted by J. Küffer and C. Münch at the University of Applied Sciences Northwestern Switzerland, School of Engineering in Windisch, Switzerland. The damping capacity of SLM-NiTi as well as the development of a thermo-mechanical training procedure to induce the two-way shape memory effect were and are issue of investigation at the University of Applied Sciences Northwestern Switzerland in the context of a bachelor- and a master-thesis, respectively. The damping capacity of SLM-NiTi is comparable to that of conventional NiTi and a manuscript entitled "Damping of NiTi implants produced by selective laser melting" for publication in the Journal of Materials Engineering and Performance is in preparation.

2 Results

2.1 Processing of NiTi by selective laser melting

2.1.1 Tailoring selective laser melting process parameters for NiTi implants

The chapter deals with the fabrication of NiTi parts by selective laser melting. The effects of different processing and heat treatment conditions were investigated by differential scanning calorimetry, X-ray diffraction and light optical microscopy. It was shown that phase transformation temperatures can be altered directly in the selective laser melting process. In addition, the pseudoelastic behavior of SLM-NiTi was demonstrated.

Published in Journal of Materials Engineering and Performance

Tailoring Selective Laser Melting Process Parameters for NiTi Implants

Therese Bormann, Ralf Schumacher, Bert Müller, Matthias Mertmann, and Michael de Wild

Complex-shaped NiTi constructions become more and more essential for biomedical applications especially for dental or cranio-maxillofacial implants. The additive manufacturing method of selective laser melting allows realizing complex-shaped elements with predefined porosity and three-dimensional micro-architecture directly out of the design data. We demonstrate that the intentional modification of the applied energy during the SLM-process allows tailoring the transformation temperatures of NiTi entities within the entire construction. Differential scanning calorimetry, x-ray diffraction, and metallographic analysis were employed for the thermal and structural characterizations. In particular, the phase transformation temperatures, the related crystallographic phases, and the formed microstructures of SLM constructions were determined for a series of SLM-processing parameters. The SLM-NiTi exhibits pseudoelastic behavior. In this manner, the properties of NiTi implants can be tailored to build smart implants with pre-defined micro-architecture and advanced performance.

1. Introduction

Laser-based additive manufacturing processes such as selective laser melting (SLM) allow for the straightforward fabrication of metallic parts with complex three-dimensional architectures directly out of powder (Ref 1). For SLM fabrication, a CAD model of the intended part is virtually cut into horizontal slices of typically 30-100 μm thickness. During the manufacturing process, a focused laser beam transmits the contour information of each virtual slice into the bed of metallic powder, which locally melts and solidifies. After scanning of one slice, the building platform is lowered about the slice thickness and re-coated by powder. The scanning of each subsequent slice by the laser and re-coating of the platform is repeated until all slices have been processed. The part is attached to the building platform via support-structures and can be removed from the machine directly after part completion. A more detailed description of the SLM fabrication process can be found in literature (Ref 2). As the preparation is simple and fast compared to conventional production methods like turning and milling, the SLM process allows fabricating patient-specific implants including dental and cranio-maxillofacial solutions for patients with special anatomical characteristics (Ref 3). In addition to dense constructions, filigree scaffold geometries with struts as small as 200 μm in diameter can be manufactured, impossible to do so with conventional mechanical machining. Hence, the generative process of SLM permits the realization of open porous structures to meet specific demands. To optimize, for example, osseointegration of bone implants, pore sizes and shapes, size distributions, and gradients have to be tailored (Ref 4). With fabrication methods, like CVD coating of vitreous carbon scaffolds (Ref 5), self-propagating high-temperature synthesis (Ref 6), or placeholder methods (Ref 7-9), the fabrication of such entities with micrometer precision is impossible. By SLM, the mechanical properties of porous bone scaffolds can be adjusted to the biomechanical needs by controlling lattice geometry, strut size, and porosity. Bone scaffolds should be further optimized by a local adaptation of scaffold architecture to the anisotropic and mechanical properties of the hard tissue (Ref 10). Implants with reduced stiffness, for example, facilitate physiological load transfer and reduce the risk of stress shielding (Ref 11).

For example, besides well-established steel, aluminum, and titanium, NiTi was recently successfully processed using SLM and laser-engineered net shaping (Ref 12-19). As a biocompatible, FDA-approved material (Ref 20), which exhibits superelasticity, shape memory effects, and high damping capacities, NiTi is a promising candidate for medical implants with extraordinary performance. Furthermore, the remarkable difference between the Young's moduli of the austenite and the martensite enables the realization of relatively soft implants

Therese Bormann, Institute for Medical and Analytical Technologies, University of Applied Sciences Northwestern Switzerland, Gründenstrasse 40, 4132 Muttenz, Switzerland; and Biomaterials Science Center, University of Basel, c/o University Hospital Basel, 4031 Basel, Switzerland; **Ralf Schumacher** and **Michael de Wild**, Institute for Medical and Analytical Technologies, University of Applied Sciences Northwestern Switzerland, Gründenstrasse 40, 4132 Muttenz, Switzerland; **Bert Müller**, Biomaterials Science Center, University of Basel, c/o University Hospital Basel, 4031 Basel, Switzerland; and **Matthias Mertmann**, Memry GmbH, Am Kesselhaus 5, 79576 Weil am Rhein, Germany. Contact e-mail: michael.dewild@fhnw.ch.

with properties close to bone (Ref 21). As shown previously (Ref 15, 22), we successfully built complex NiTi-structures with shape memory properties. In the present article, we report on SLM fabrication of dense NiTi products with intentionally modified thermo-mechanical properties by altering the applied laser energy density. In this manner, biomimetic NiTi implants with anisotropic, gradually changing thermo-mechanical properties can be built.

2. Experimental Procedure

2.1 Specimen Preparation

Cylindrical specimens with diameters of 5 and 7 mm and height of 15 mm were produced in a vertical direction from pre-alloyed NiTi-powder (MEMRY GmbH, Weil am Rhein, Germany) by the SLM-Realizer 100 (SLM-Solutions, Lübeck, Germany). The powder with a D_{50} value of 60 μm was produced by gas atomization from starting material with a nominal Ni-content of 56.1 wt.%. Particle size analysis was done by laser diffraction (HELOS/BR, Sympatec GmbH, Clausthal-Zellerfeld, Germany). The cylinders were fabricated by four sets of processing parameters. Laser power and scanning velocity were varied from 60 to 80 W and from 171 to 133 mm/s, respectively. This choice resulted in energy densities of 60, 70, 84, and 100 J/mm³. As given by Eq 1, the energy density E_v depends on the laser power P, the scanning velocity v, the spacing between laser vectors h, and the layer thickness d. Equation 1 estimates the overall energy input into the powder-bed during SLM processing (Ref 23).

$$E_v = \frac{P}{h \cdot d \cdot v} \qquad \text{(Eq 1)}$$

The powder layer thickness in the experiments was set to $d = 50$ μm. The laser vector spacing for the hatch was $h = 120$ μm. Subsequent to SLM fabrication, the specimens were removed from the building platform and cut transversally into three parts using a low-speed diamond saw (IsoMet®, Buehler). One part of each was kept for investigating as-built specimens (''SLM''). The second part was solution annealed at a temperature of 800 °C for a period of 30 min and subsequently water-quenched. The last specimen part was annealed at a temperature of 500 °C for a period of 20 min followed by slow cooling. In addition to the cylinders, tensile test specimens according to shape D specified in the DIN 50125 (Ref 24) were manufactured with the processing parameter set corresponding to 70 J/mm³. SLM processing and heat treatments took place under protective Ar atmosphere.

Data on transformation temperatures as presented in Fig. 1 and 2 include measurements on cylinders 5 and 7 mm in diameter. The measurements of cylinders with 5 mm in diameter annealed at 500 °C were skipped, because the cooling rates in this case during furnace cooling were not reproducible enough.

2.2 Specimen Characterization

The phase transformation temperatures for martensite start (M_s), martensite peak (M_p), martensite finish (M_f), austenite start (A_s), austenite peak (A_p), and austenite finish (A_f) were determined using differential scanning calorimetry (DSC, DSC

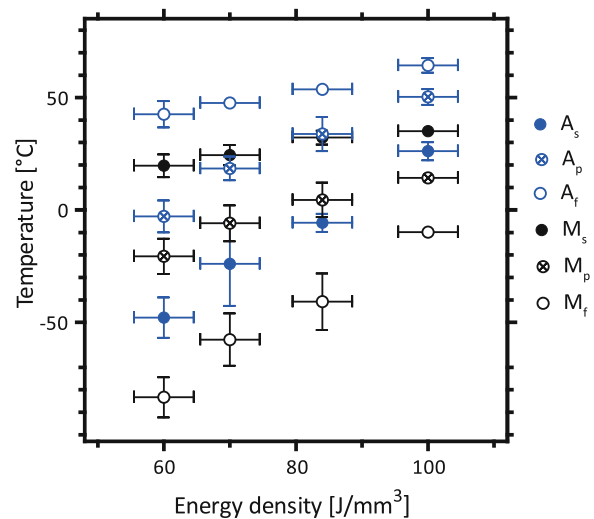**Fig. 1** Phase transformation temperatures of SLM-specimens fabricated with different energy densities
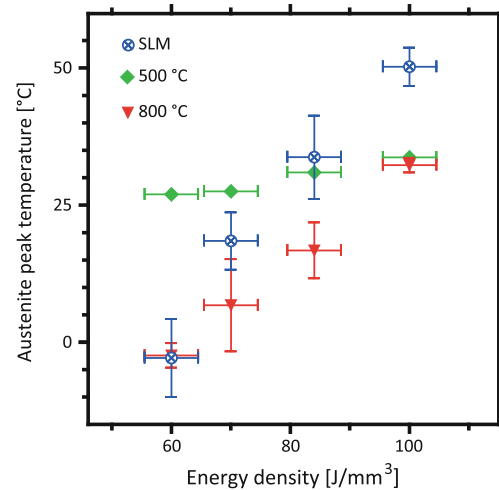

Fig. 2 Austenite peak temperatures for as-built and heat-treated SLM-specimens fabricated with different energy densities. Heat treatments were done at 800 °C and 500 °C

30, Mettler-Toledo) in the temperature range between +100 and −125 °C with heating and cooling rates of 10 K/min. X-ray diffraction (XRD) was carried out on the specimens 7 mm in diameter with grinded and electro-polished surfaces (details see below) using the D2-Phaser system (Bruker, Karlsruhe, Germany) equipped with a Co x-ray tube (K_α-radiation, $\lambda = 1.78897$ Å). The temperature during XRD measurements was about 32 °C. Before the XRD investigations, specimens were heated above A_f to ensure a well-defined primarily austenitic sample state.

The oxygen contents of the as-built and annealed specimens were measured by the inert gas fusion method (Galileo G8, Bruker, Karlsruhe, Germany). Before analyzing the oxygen-content, we removed the oxide surface layer by means of mechanical grinding and electro-polishing. Position-controlled tensile testing was performed in cyclic manner at room
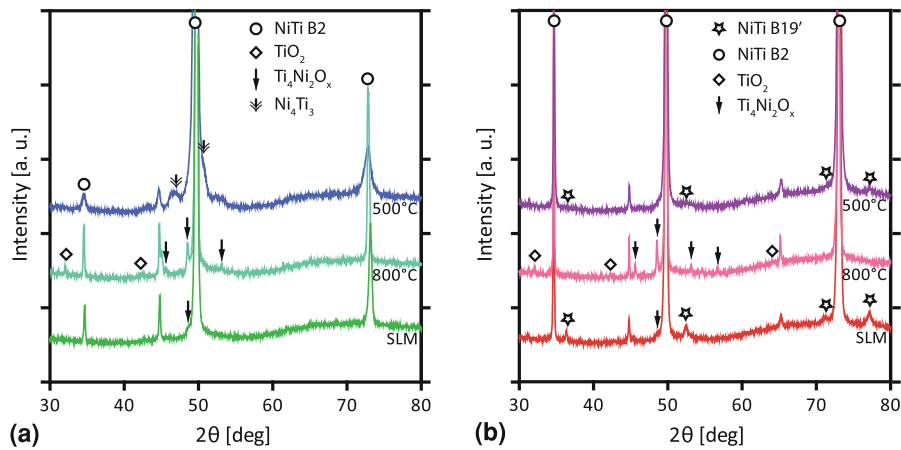
Fig. 3 XRD patterns of SLM-specimens in as-built and annealed conditions. (a) Specimens prepared with an energy density of 70 J/mm^3 and (b) specimens built using an energy density of 100 J/mm^3

temperature with a constant testing speed of 0.25 mm/min by means of a universal testing machine (Z100, Zwick/Roell, Ulm, Germany). Again, we heated the specimen before cyclic tensile testing above A_f to ensure a primarily austenitic sample state. The preparation procedure for the microstructural investigations by optical microscopy included grinding (MetaServ®, Buehler), polishing with colloidal SiO$_2$-solution (Mastermet®, Buehler), and electro-polishing using a voltage of 20 V and a temperature of 22 °C for a period of 30 s with final etching during 60 s. The electrolyte for electro-polishing consisted of 3 M H$_2$SO$_4$ in 1:1 ethanol-methanol (Ref 25) and the chemical etchant of distilled water, HCl, Na$_2$S$_2$O$_5$, K$_2$S$_2$O$_5$, and NH$_4$HF, according to Escher and Hühner (Ref 26).

3. Results and Discussion

3.1 Characterization of Phase Transformation Temperatures

The SLM processing parameters determine the phase transformation temperatures as displayed in Fig. 1. The step-wise variation of the energy density between 60 and 100 J/mm^3 led to an increase of the transformation temperatures of up to 75 K. A_s, for example, increased from −50 to 25 °C. Figure 2 presents the austenite peak temperatures of the as-built and annealed specimens. In specimens solution annealed at 800 °C, we still found increased transformation temperatures with rising energy densities. Nevertheless, the austenite peak temperatures of the specimens produced with 70, 84, and 100 J/mm^3 shifted about 12-18 K toward lower values. After annealing at 500 °C, the austenite peak temperatures leveled off at about 30 °C. Only a slight variation of about 5 K was detected among the specimens. The error bars for the energy density in Fig. 1 and 2 are caused by variations in layer thickness and laser power during processing.

3.2 XRD Study

Figure 3 shows the XRD patterns for specimens prepared with energy densities of 70 J/mm^3 (a) and of 100 J/mm^3 (b). The as-built specimens exhibit mainly peaks of the austenite

phase B2. The small peak at 2θ = 48.5° reflects the presence of Ti$_4$Ni$_2$O$_x$ and/or Ti$_2$Ni. No differences in terms of precipitates and impurities were found in the as-built specimens. The as-built specimen prepared with 100 J/mm^3 represents additional peaks at 36.4°, 52.5°, 71.4°, and 77.3° marked by stars in Fig. 3(b), which arise from the martensite phase B19′. The martensite phase originates from the phase transformation B2 → B19′, which starts at the temperature M_s = 35 °C. Note that XRD investigations were carried out at ∼32 °C. The reflections at 44.7° and 65.3° could not definitely be identified; possibly they refer to elemental titanium. Besides, from SLM specimens, both peaks are present in powder and starting material before atomization (data not shown), i.e., they do not refer to precipitates or impurities caused by SLM fabrication.

XRD investigations of specimens annealed at 800 °C show the formation of Ti-rich phases. The reflections at 32.0°, 42.2°, and 64.1°, marked by open diamonds in Fig. 3, refer to TiO$_2$, while the reflections at 45.6°, 48.5°, and 53.1° marked by arrows, refer to Ti$_2$Ni and oxygen-rich inclusions like Ti$_4$Ni$_2$O$_x$. As we detected oxygen contents of (0.102 ± 0.019) wt.% in as-built, of (0.101 ± 0.005) wt.% in 500 °C annealed and of (0.118 ± 0.003) wt.% in 800 °C annealed specimens (Ref 22), the oxygen content increased by about 0.02 wt.% after solution annealing. One can, therefore, reasonably assume that the reflections at 45.6°, 48.5°, and 53.1° rather originate from Ti$_4$Ni$_2$O$_x$ than from Ti$_2$Ni.

The phase transformation temperatures in Ni-rich NiTi, as is well known, depend on the Ni/Ti ratio (Ref 27, 28). Ni-loss leads to an increase, whereas Ti-loss leads to a decrease of the transformation temperatures. As no evidence for Ni-consuming phases could be found in the as-built and the 800 °C-treated specimens, we hypothesize that Ni evaporated during the processing causing the increased transformation temperatures with applied energy density. This hypothesis is in accordance with findings of Meier et al. (Ref 12). Two explanations can be used to understand the decrease in phase transformation temperatures after 800 °C annealing. First, the formation of Ti-rich impurities during solution annealing (cp. Fig. 3) leads to Ti-reduction in the NiTi-matrix, which reduces the transformation temperatures. Secondly, Ni$_4$Ti$_3$-precipitates in quantities below the detection limit of XRD were formed during SLM
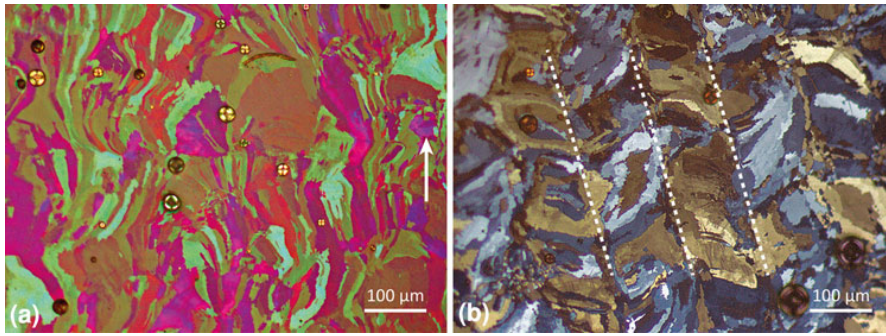
Fig. 4 Optical micrographs of SLM-NiTi. (a) Image along building direction (indicated by arrow). (b) Image perpendicular to the building direction. The laser paths are indicated by dotted lines

processing—in addition to the evaporation of Ni. Their dissolution during solution annealing results in an increased Ni-content in the NiTi-matrix, which would also lead to decreasing transformation temperatures. Both mechanisms may coexist. Because the $Ti_4Ni_2O_x$-reflections developed in the XRD-patterns, their amount must be considerably high. Consequently, the first explanation should be dominant.

Further work is required to fully uncover the mechanisms of impurity formation during SLM fabrication and annealing processes and their influence on the phase transformation temperatures. Usage of a vacuum-furnace might be beneficial in avoiding the formation of Ti-rich impurities during solution annealing.

The increase of the transformation temperatures of the 60 and 70 J/mm^3 specimens, which were annealed at 500 °C, is caused by the formation of Ni-rich Ni_4Ti_3-precipitates detected by means of XRD analysis (see Fig. 3(a), reflections marked by double-lined arrows). In specimens prepared at 84 and 100 J/mm^3 and annealed at 500 °C, the transformation temperatures did not increase. Consequently, XRD investigations did not show Ni_4Ti_3-precipitates. This is in accordance with the higher transformation temperatures (in the as-built state) and the reduced Ni-content in the NiTi-matrix, respectively, as more Ni should have evaporated at elevated energy densities and the formation of Ni_4Ti_3-precipitates is known to occur only in NiTi exceeding a nominal Ni-content of 50.5 at.% and 55.57 wt.%, respectively (Ref 29).

3.3 Microstructure

Metallographic analysis on specimens produced at 70 J/mm^3 revealed columnar grains with lengths up to several hundred micrometers (see Fig. 4(a)), which proceed along several powder layers. The grains are oriented in building direction because of epitaxial growth in the direction of heat transfer (Ref 30). In cross sections perpendicular to the building direction, we found elongated, platelet-shaped grains that extend to 150 µm (see Fig. 4 (b)). Their arrangement refers to the alternating laser route with a vector spacing of 120 µm, as indicated in Fig. 4 (b). A broad size distribution of the grains is observed. Similar anisotropic microstructure caused by SLM fabrication have been reported, e.g., for TiAl6V4 (Ref 30) and TiAl6Nb7 (Ref 31).

3.4 Mechanical Characterization

Figure 5 displays three cyclic tensile tests of a selected specimen produced at 70 J/mm^3. At room temperature, the specimen was basically in austenitic state, but since M_s was
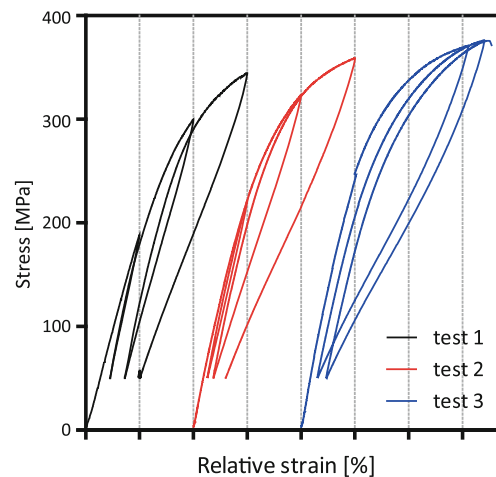
Fig. 5 Loading-unloading cycles of an SLM tensile test specimen produced with an energy density of 70 J/mm^3. Each increment on the x-axis represents 1% relative strain
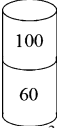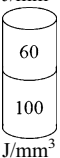
approximately 25 °C, also the martensitic phase was expected. The load-relief curves show clearly the characteristic pseudo-elastic behavior. Note that the specimen was in the as-built condition, i.e., no additional heat treatment was applied. From Fig. 5, it is apparent that the first cycle exhibited a residual deformation of about 0.7% strain after maximal straining to 3%. As the sample was kept at a minimum stress of 50 MPa, we derived the plastic deformation by extrapolating the relief curve to σ = 0 MPa. Martensite de-twinning most probably caused the residual strain of 0.7% after the first cycle. After straining the specimen for a second time to 3%, we calculated only 0.2% deformation after specimen relief, which shows that nearly the entire martensite were de-twinned already during the first cycle. In the third cycle, the specimen was strained up to 3.4%, whereupon we detected a complete shape recovery.

Further, to evaluate the pseudoelastic properties at higher strain levels, improvement of the mechanical properties of specimens in SLM tensile testing is necessary, as our specimens fail usually at around 4% strain.

3.5 Varying Processing Parameters Within One Construct

As the processing parameters influence the phase transformation temperatures, we conducted preliminary experiments on

Table 1 **Difference in transformation temperatures of specimens produced with two distinct sets of process parameters (cp. scheme); ΔT represents the difference between upper and lower entities**

	ΔA_s, K	ΔA_p, K	ΔA_f, K	ΔM_s, K	ΔM_p, K	ΔM_f, K
100 / 60 J/mm^3	29 ± 6	35 ± 3	20 ± 6	12 ± 6	17 ± 3	48 ± 6
60 / 100 J/mm^3	13 ± 3	13 ± 1	14 ± 3	14 ± 3	15 ± 1	8 ± 3

NiTi specimens consisting of two regions built with distinct SLM parameters. As listed in Table 1, lower and upper parts of cylindrical specimens were produced with 100 and 60 or 60 and 100 J/mm^3, respectively. The processing by varying SLM parameters led to NiTi-parts with regions of different phase transformation temperatures. Differences in the observed phase transformation temperatures are summarized in Table 1. This difference, however, is smaller than expected from the experiments presented above, in which differences of up to 75 K were detected. The entities prepared with 60 J/mm^3 show considerable differences in their transformation temperatures, possibly caused by modified cooling rates within the specimens during the building process. For a better control, further dependencies of transformation temperatures on the process parameters have to be examined.

4. Conclusions

Using different sets of process parameters, the phase transformation temperatures of SLM built NiTi entities can be directly tailored. The reason behind is most likely the Ni loss by evaporation, which increases with applied energy density. Solution annealing leads to a decrease of the phase transformation temperatures in the specimens produced with energy densities of 70, 84, and 100 J/mm^3, associated with the formation of Ti-rich phases including $Ti_4Ni_2O_x$ and TiO_2. Nevertheless, the increase in transformation temperatures with applied energy densities is preserved. After annealing at 500 °C, the specimens did not show remarkable differences in their transformation temperatures anymore. Cyclic loading proved that SLM-built specimens exhibit pseudoelastic behavior directly after manufacturing, i.e., without additional heat treatments. A shape recovery of up to 3% strain was demonstrated.

The application of varied SLM process parameters, therefore, allows for the fabrication of pseudoelastic and pseudoplastic NiTi-structures from the same starting material. In addition, constructions consisting of several regions with distinct phase transformation temperatures can be built. This approach permits manufacturing implants with locally pre-defined anisotropic properties. SLM-produced implants could, for example, consist of pseudoelastic, shock-absorbing regions, on the one hand; pseudoplastic regions, on the other hand, would offer a reduced Young's modulus and the possibility to facilitate the one-way shape memory effect.

References

1. I. Yadroitsev, L. Thivillon, P. Bertrand, and I. Smurov, Strategy of Manufacturing Components with Designed Internal Structure by Selective Laser Melting of Metallic Powder, *Appl. Surf. Sci.*, 2007, **254**(4), p 980–983
2. D.K. Pattanayak, A. Fukuda, T. Matsushita, M. Takemoto, S. Fujibayashi, K. Sasaki, N. Nishida, T. Nakamura, and T. Kokubo, Bioactive Ti Metal Analogous to Human Cancellous Bone: Fabrication by Selective Laser Melting and Chemical Treatments, *Acta Biomater.*, 2010, **7**(3), p 1398–1406
3. L. Mullen, R.C. Stamp, W.K. Brooks, E. Jones, and C.J. Sutcliffe, Selective Laser Melting: A Regular Unit Cell Approach for the Manufacture of Porous, Titanium, Bone In-Growth Constructs, Suitable for Orthopedic Applications, *J. Biomed. Mater. Res. Part B*, 2009, **89**(2), p 325–334
4. F.C. Fierz, F. Beckmann, M. Huser, S.H. Irsen, B. Leukers, F. Witte, O. Degistirici, A. Andronache, M. Thie, and B. Müller, The Morphology of Anisotropic 3D-Printed Hydroxyapatite Scaffolds, *Biomaterials*, 2008, **29**(28), p 3799–3806
5. B.R. Levine, S. Sporer, R.A. Poggie, C.J. Della Valle, and J.J. Jacobs, Experimental and Clinical Performance of Porous Tantalum in Orthopedic Surgery, *Biomaterials*, 2006, **27**(27), p 4671–4681
6. J.S. Kim, S.H. Lee, J.H. Kang, V.E. Gjunter, S.B. Kang, T.H. Nam, and Y.S. Kwon, The Effect of Processing Variables on the Microstructure and Mechanical Property of a Porous Body Produced by the SHS Method, SMST-2000, *Proceedings of SMST 2000*, 2000, p 77
7. T. Imwinkelried, Mechanical Properties of Open-Pore Titanium Foam, *J. Biomed Mater. Res. Part A*, 2007, **81**(4), p 964–970
8. A. Bansiddhi and D.C. Dunand, Shape-Memory NiTi Foams Produced by Replication of NaCl Space-Holders, *Acta Biomater.*, 2008, **4**(6), p 1996–2007
9. R. Singh, P.D. Lee, T.C. Lindley, R.J. Dashwood, E. Ferrie, and T. Imwinkelried, Characterization of the Structure and Permeability of Titanium Foams for Spinal Fusion Devices, *Acta Biomater.*, 2009, **5**(1), p 477–487
10. R. Schumacher, A. Yildiz, M. Näf, M. de Wild, and E. Schkommodau, Manipulation of the Elastic Behaviour of Artificial Titanium Bone Grafts, *Eur. Cells Mater.*, 2011, **22**(Suppl. 1), p 10
11. R. Huiskes, H. Weinans, and B. Van Rietbergen, The Relationship Between Stress Shielding and Bone Resorption Around Total Hip Stems and the Effects of Flexible Materials, *Clin. Orthop. Rel. Res.*, 1992, **274**, p 124–134
12. H. Meier, C. Haberland, J. Frenzel, and R. Zarnetta, Selective Laser Melting of NiTi Shape Memory Components, *Innovative Developments in Design and Manufacturing: Advanced Research in Virtual and Rapid Prototyping*, CRC Press-Taylor & Francis Group, 2010, p 233–238
13. A.T. Clare, P.R. Chalker, S. Davies, C.J. Sutcliffe, and S. Tsopanos, Selective Laser Melting of High Aspect Ratio 3D Nickel–Titanium Structures Two Way Trained for MEMS Applications, *Int. J. Mech. Mater. Des.*, 2008, **4**, p 181–187
14. S. Dudziak, M. Gieseke, H. Haferkamp, S. Barcikowski, and D. Kracht, Functionality of Laser-Sintered Shape Memory Micro-Actuators, *Laser Assisted Net Shape Engineering 6, Proceedings of the Lane 2010, Part 2*, Elsevier Science Bv, 2010, p 607–615
15. T. Bormann, S. Friess, M. de Wild, R. Schumacher, G. Schulz, and B. Müller, Determination of Strain Fields in Porous Shape Memory Alloys

Using Micro Computed Tomography, *Proc SPIE*, 2010, **7804**, p 78041M

16. A. Bandyopadhyay, B.V. Krishna, W.C. Xue, and S. Bose, Application of Laser Engineered Net Shaping (LENS) to Manufacture Porous and Functionally Graded Structures for Load Bearing Implants, *J. Mater. Sci. Mater. Med.*, 2009, **20**, p 29–34

17. B.V. Krishna, S. Bose, and A. Bandyopadhyay, Laser Processing of Net-Shape NiTi Shape Memory Alloy, *Metall. Mater. Trans. A Phys. Metall. Mater. Sci.*, 2007, **38**(5), p 1096–1103

18. B.V. Krishna, S. Bose, and A. Bandyopadhyay, Fabrication of Porous NiTi Shape Memory Alloy Structures Using Laser Engineered Net Shaping, *J. Biomed. Mater. Res. Part B*, 2009, **89**(2), p 481–490

19. H. Meier, C. Haberland, and J. Frenzel, Structural and Functional Properties of NiTi Shape Memory Alloy Produced by Selective Laser Melting, *Innovative Developments in Design and Manufacturing: Advanced Research in Virtual and Rapid Prototyping*, CRC Press-Taylor & Francis Group, 2012, p 291–296

20. ASTM, *Standard Specification for Wrought Nickel-Titanium Shape Memory Alloys for Medical Devices and Surgical Implants*, F2063, ASTM International

21. T.W. Duerig and A.R. Pelton, Ti-Ni Shape Memory Alloys, *Materials Properties Handbook: Titanium Alloys*, R. Boyer, G. Welsch, and E.W. Collings, Ed., ASM International, Materials Park, 1994

22. T. Bormann, R. Schumacher, B. Müller, and M. de Wild, Fabricating NiTi Shape Memory Scaffolds by Selective Laser Melting, *Eur. Cells Mater.*, 2011, **22**(Suppl. 1), p 12

23. H. Meier and C. Haberland, Experimental Studies on Selective Laser Melting of Metallic Parts, *Materialwiss. Werkst.*, 2008, **39**(9), p 665–670

24. Prüfung metallischer Werkstoffe - Zugproben, DIN 50125:2004-01, Deutsches Institut für Normung e.V

25. H. Schumann and H. Oettel, *Metallografie*, Wiley-VCH, Weinheim, 2005

26. K. Escher and M. Huhner, Metallographical Preparation of NiTi Shape Memory Alloys, *Prakt. Metallogr.*, 1990, **27**(5), p 231–235

27. J. Khalil-Allafi, A. Dlouhy, and G. Eggeler, Ni_4Ti_3-Precipitation During Aging of NiTi Shape Memory Alloys and its Influence on Martensitic Phase Transformations, *Acta Mater.*, 2002, **50**(17), p 4255–4274

28. J. Frenzel, E.P. George, A. Dlouhy, C. Somsen, M.F.-X. Wagner, and G. Eggeler, Influence of Ni on Martensitic Phase Transformations in NiTi Shape Memory Alloys, *Acta Mater.*, 2010, **58**, p 3444–3458

29. E. Schuller, M. Bram, H.P. Buchkremer, and D. Stover, Phase Transformation Temperatures for NiTi Alloys Prepared by Powder Metallurgical Processes, *Mater. Sci. Eng. A Struct. Mater. Prop. Microstruct. Process.*, 2004, **378**(1–2), p 165–169

30. L. Thijs, F. Verhaeghe, T. Craeghs, J.V. Humbeeck, and J.-P. Kruth, A Study of the Microstructural Evolution During Selective Laser Melting of Ti-6Al-4V, *Acta Mater.*, 2009, **58**(9), p 3303–3312

31. E. Chlebus, B. Kuznicka, T. Kurzynowski, and B. Dybala, Microstructure and Mechanical Behaviour of Ti-6Al-7Nb Alloy Produced by Selective Laser Melting, *Mater. Charact.*, 2011, **62**(5), p 488–495

2.1.2 Microstructure of selective laser melted nickel-titanium

The following article describes the impact of the selective laser melting processing parameters on microstructural properties such as grain size, grain arrangement, texture and phase transformation temperatures of SLM NiTi. The preferential loss of Ni depends on the scanning speed, while grain sizes, grain size distribution and the degree of crystallographic texture can be altered by variation of the laser power. The bimodal grain size distribution in coarse-grained specimens indicates Ostwald-ripening of the crystallites during SLM processing.

Published in Materials Characterization

Available online at www.sciencedirect.com

ScienceDirect

www.elsevier.com/locate/matchar

Microstructure of selective laser melted nickel–titanium

Therese Bormann[a,b], Bert Müller[a,*], Michael Schinhammer[c], Anja Kessler[b],
Peter Thalmann[a], Michael de Wild[b]

[a]Biomaterials Science Center, University of Basel, c/o University Hospital Basel, 4031 Basel, Switzerland
[b]Institute for Medical and Analytical Technologies, School of Life Sciences, University of Applied Sciences and Arts Northwestern Switzerland, Gründenstrasse 40, 4132 Muttenz, Switzerland
[c]ETH Zürich, Department of Materials, Wolfgang-Pauli-Strasse 10, 8093 Zürich, Switzerland

ARTICLE DATA

ABSTRACT

In selective laser melting, the layer-wise local melting of metallic powder by means of a scanning focused laser beam leads to anisotropic microstructures, which reflect the pathway of the laser beam. We studied the impact of laser power, scanning speed, and laser path onto the microstructure of NiTi cylinders. Here, we varied the laser power from 56 to 100 W and the scanning speed from about 100 to 300 mm/s. In increasing the laser power, the grain width and length increased from (33 ± 7) to (90 ± 15) μm and from (60 ± 20) to (600 ± 200) μm, respectively. Also, the grain size distribution changed from uni- to bimodal. Ostwald-ripening of the crystallites explains the distinct bimodal size distributions. Decreasing the scanning speed did not alter the microstructure but led to increased phase transformation temperatures of up to 40 K. This was experimentally determined using differential scanning calorimetry and explained as a result of preferential nickel evaporation during the fabrication process. During selective laser melting of the NiTi shape memory alloy, the control of scanning speed allows restricted changes of the transformation temperatures, whereas controlling the laser power and scanning path enables us to tailor the microstructure, i.e. the crystallite shapes and arrangement, the extent of the preferred crystallographic orientation and the grain size distribution.

1. Introduction

Selective laser melting (SLM) is an additive manufacturing technique that allows the near-net-shape production of con-structional elements with a wide geometrical freedom. During SLM, a focused laser beam melts the powder locally and layer-wise. Thereby, a CAD-defined design is transferred into super-imposed powder layers [1,2]. With medical applications in mind, SLM permits manufacturing of patient-specific implants taking advantage of three-dimensional medical data and of micro-porous scaffolds for tissue engineering [3,4]. Therefore, the SLM technique shows great potential to build medical implants, for example using the shape memory alloy NiTi [5–7]. This alloy has been established for load-bearing implants, owing to the pseudoelasticity, the elastic modulus, the damping capa-city, the biocompatibility and the corrosion resistance [8–11]. For these medical applications, well-defined guidelines concerning the microstructure of implant material exist, as the structural

* *Corresponding author.*
  E-mail address: bert.mueller@unibas.ch (B. Müller).

properties determine the static and dynamic mechanical behavior. Because the grain size in metals is crucial for toughness, strength and resistance to crack initiation, described with the Hall–Petch relation [12], the ASTM standard F2063-05 defines a minimum grain size (G) of 4 for NiTi in medical applications [13]. This means that the average diameter of equiaxed grains should not exceed 90 μm [14]. Furthermore, rather small grains and a narrow grain size distribution are beneficial for adequate fatigue strength [15–17]. In order to obtain such microstructural properties, as-cast NiTi is usually post-processed by hot- and cold-working and heat treatments [18].

SLM leads to anisotropic microstructures with elongated grains. The reason behind is the layer-wise melting and solidification, which comes along with epitaxial grain growth in the building direction [6,19–21]. Melt pool shape, heat transfer processes and thus grain growth mechanisms show similarities to classical welding [22]. As in the SLM fabrication process a multitude of molten tracks is combined to form a three-dimensional part, heat transfer and grain growth are often complex and the repeated energy input during SLM causes effects that can play a dominant role for the evolving microstructure [23]. Despite the anisotropic microstructures, SLM-built near-net-shape parts are typically not intended for post-processing including hot- or cold-working as the shape is pre-defined and the avoidance of post-processing ensures efficient fabrication. The understanding on how to control crystallization and grain growth during SLM is therefore essential to realize the full potential of this sophisticated fabrication method.

The microstructure of the built constructional element depends on the SLM process parameters including powder layer thickness, laser power, scanning velocity, distance between the individual laser vectors, size and location of the focus of the laser beam as well as scanning path [21,24]. In order to simplify the approach, certain parameters are linked. The energy density combines laser power, scanning speed, separation distance between the scanning tracks and layer thickness [2]. We hypothesize that such a combination is meaningful, since the energy deposition yields the determining factor for the grain formation. To corroborate our hypothesis, the grain sizes have to be determined as a function of laser power and scanning speed. For such experiments one has to take into account the higher vapor pressure of nickel compared to titanium, both present in the alloy. The related nickel loss is determined from the transformation temperatures measured by means of differential scanning calorimetry according to Frenzel et al. [25].

The present study should sustain and improve the understanding of the microstructures formed as the result of the SLM process. The gained knowledge will allow choosing optimized parameters for preparing technically mature, selective laser-melted, medical implants.

2. Material and methods

2.1. NiTi cylinder preparation

Selective laser melting by means of the SLM Realizer 100 (SLM-Solutions, Lübeck, Germany) served for the fabrication of NiTi cylinders [6,26]. The NiTi powder particles had sizes

between 35 and 180 μm. According to the specification of the manufacturer (Memry GmbH, Weil am Rhein, Germany) the composition of the starting NiTi material prior to atomization was determined to 55.96 wt.% Ni, 0.0151 wt.% O, 0.033 wt.% C, 0.0017 wt.% H and balance Ti.

Table 1 lists the two groups of cylinders each 7 mm in diameter and 14 mm high, which were fabricated to investigate the microstructure of the selected laser-melted NiTi as a function of the selected process parameters. Group A refers to the controlled increase of the laser power with constant exposure time while groups B and C correspond to dedicated alterations of the exposure time with constant laser power. The longitudinal axes of the cylinders were perpendicular to the building direction, as outlined in Fig. 1. Each slice is scanned by specifically arranged laser vectors, of which the confining, outermost path is termed *boundary* while all vectors lying inside of the boundary are termed *hatch*. The energy density E describes the energy input per volume during SLM [5,19]:

$$E = P/vhd \tag{1}$$

where P denotes the laser power, v the scanning velocity, h the distance between the individual hatch vectors and d the slice thickness of the individual layers. The scanning velocity v is determined by

$$v = p_d/t_e \tag{2}$$

with the point distance p_d and the exposure time t_e.

In this study, the hatch spacing h always corresponded to 120 μm, the slice thickness d to 50 μm and the point distance p_d to 30 μm. For group A the energy density increased because of the laser power elevation. In the same manner, the exposure time extension caused the energy density increase for group B, cp. Table 1. The window of the process parameters investigated has been defined as well-suited for the production of sound NiTi parts [27]. For the NiTi cylinders of groups A, B and C the laser beam for the hatch of each slice was guided along parallel and linear paths as represented in the scheme on the left of Fig. 1. The scanning direction within the working plane alternated from slice-to-slice

Table 1 – List of selective laser-melted NiTi cylinders 7 mm in diameter and 14 mm in height with the related processing parameters.

Specimen	Laser power (W)	Exposure time (10^{-6} s)/scanning speed (mm/s)	Energy density (J/mm^3)
A1[a]	56	225/133	70
A2	68	225/133	85
A3[a]	80	225/133	100
A4	92	225/133	115
A5	100	225/133	125
C1[b]	80	101/297	45
C2[b]	80	134/224	60
B1[a]	80	158/190	70
B2	80	191/157	85
B3[a]	80	225/133	100
B4	80	259/116	115
B5	80	281/107	125

[a] Specimens, where two batches are available.
[b] Specimens only prepared during the second batch.
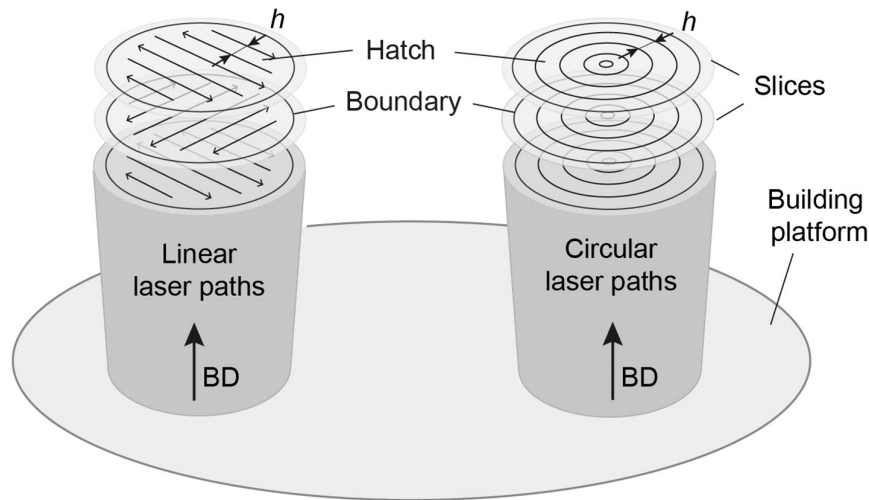
Fig. 1 – Scheme of the layer-wise selective laser melting fabrication process. The laser melts the inner section, the so-called hatch, according to linear (left) and circular (right) scanning paths, respectively. In each slice, the hatch is scanned prior to the boundary featuring a laser vector spacing h = 120 μm. Arrows indicate the building direction (BD) normal to the building platform.

by 90°. The circular boundary path determined the outer shape of the NiTi cylinder. It was scanned subsequent to the hatch in each slice. In order to demonstrate reproducibility, for selected specimens the fabrication process was repeated after an interruption for preparation of 19 batches for other purposes, see Table 1. It should be mentioned that for the two batches the NiTi-powder originated from the same powder lot.

A fourth group of cylindrical specimens, group D, with a diameter of 1 mm and a height of 15 mm was fabricated. Specimens D1 and D2 were fabricated using linearly arranged hatch vectors (cp. Fig. 1, left) with the processing parameters of specimens A4 and B4 given above. Specimen D3 was scanned with circularly arranged hatch vectors that were scanned from the inside to the outside and had a spacing of 120 μm (see right part of Fig. 1). The processing parameter set of specimen B4 was used. For both scanning strategies applied, the scanning of the boundary was performed subsequent to scanning of the hatch in each slice.

The specimens produced within this study were built with a fixed lens position for a laser beam focused onto the powder bed.

2.2. Characterization of selective laser-melted NiTi in as-built state

Differential scanning calorimetry (DSC) enabled us to determine the phase transformation temperatures martensite start (M_s), martensite finish (M_f), austenite start (A_s) and austenite finish (A_f) of the starting material prior to atomization and the SLM-fabricated cylinders. For this purpose, the DSC30 system of Mettler-Toledo GmbH (Greifensee, Switzerland) was used in the temperature range between −125 and +100 °C with heating and cooling rates of 10 K/min. The cylinders did not receive any additional treatment after the SLM fabrication process and are therefore termed *as-built*. In order to determine the phase transformation temperatures of the starting material

prior to atomization, the bar stock was solution annealed at a temperature of 800 °C for a period of 30 min followed by water quenching previous to DSC. This procedure reduces the artifacts owing to precipitates.

The relative densities of the specimens of groups A and B were determined according to Archimedes principle using a tensiometer (K11, Krüss, Nürnberg, Germany). The oxygen-content was determined by inert gas fusion method (Galileo G8, Bruker, Kalkar, Germany) on electro-polished specimens, details on electro-polishing are given below.

For the microstructural characterization of the layer-wise prepared NiTi cylinders, longitudinal sections (plane in building direction) and cross sections perpendicular to the longitudinal cylinder axis (slice plane) were prepared. For this purpose, the cylinders of groups A and B were sectioned 4.5 mm from the top. In the next step, the 4.5 mm long part was cut in building direction. One of the two cut parts served for the investigation of the microstructure in the slice plane, the other for the investigation of the microstructure parallel to the building direction. The two surfaces were prepared for the metallographic examination by means of mechanical grinding, polishing and etching. The grinding step was based upon abrasive SiC paper (Buehler, Düsseldorf, Germany) to a grit size of P1200. Subsequently, mechanical polishing employed the colloidal silica suspension MasterMet2® (Buehler, Düsseldorf, Germany). The following electro-polishing with the electrolyte consisting of 3 M H_2SO_4 in 1:1 ethanol–methanol [28] was carried out at a temperature of 22 °C and a voltage of 20 V for a period of 30 s. For the optical micrographs, the final color-etching step of the surfaces with a duration of 60 s was performed according to the procedure described by Escher and Hühner [29]. This etching solution consisted of 120 ml pure water, 15 ml HCl (Merck), 15 g $Na_2S_2O_5$ (Fluka), 10 g $K_2S_2O_5$ (Merck) and 2 g NH_4HF (Sigma-Aldrich). The microscope BX61 using linearly polarized light (Olympus Schweiz AG, Volketswil, Switzerland) was applied to

optically acquire the micrographs of the polished and etched surfaces with the aim of indentifying the grains.

Electron backscatter diffraction (EBSD) measurements were conducted in a Hitachi SU-70 scanning electron microscope (SEM) equipped with a Nordlys camera (Oxford Instruments) [30] to relate the grains to their crystallographic orientation. The SEM operated at an acceleration voltage of 20 kV and a probe current of about 2 nA. EBSD grain maps of (2.5×1.9) mm^2 were obtained at polished sections of the NiTi cylinders A1, A4 and B1 in the slice plane. The indexing rates corresponded to 65% for specimen A1, 72% for specimen A4 and 57% for specimen B1. The partially inhomogeneous microstructure aggravated the EBSD analysis and hence yielded a decrease in the indexing rate.

On the basis of the light optical micrographs obtained with a magnification of 50 at the specimens of groups A and B, the sizes of the individual grains and their average were measured by the linear intercept procedure [14] from at least 24 lines of 1 mm length for the grain width and from at least 16 lines between 1 and 4 mm length for the grain length. *Grain width* refers to the linear dimension in the slice plane, whereas *grain length* corresponds to the linear dimension in building direction. Since the linear laser-scanning path predetermines the alignment of the grains, the intercept lines were chosen parallel to the scanning path through the center of the grains. The grain size distribution unfolded from 140 ± 2 individual grain widths measured along the intercept lines in the slice plane. Two-dimensional discrete fast Fourier transforms of the optical micrographs were carried out using Matlab (2010b, The MathWorks, Natick, USA).

2.3. Characterization of solution annealed selective laser-melted NiTi

The remaining parts of the cylindrical specimens summarized in Table 1 were solution annealed at 800 °C for 30 min under Ar atmosphere and subsequently water quenched. DSC analysis (Perkin Elmer, DSC 8500) was carried out in the temperature range between -100 and +60 °C with heating and cooling rates of 10 K/min in order to determine M_s, M_f, A_s and A_f of the annealed specimens.

Oxygen and hydrogen contents of the annealed specimens were measured with the inert gas fusion method (Galileo G8, Bruker, Karlsruhe, Germany). The oxide layer was mechanically removed prior to the measurements.

3. Results

3.1. Structural characterization

Fig. 2 shows light optical micrographs perpendicular to the longitudinal axes of the NiTi cylinders (slice plane, left) and parallel to the longitudinal axes, i.e. in the building direction (right). The arrangement and orientation of the grains in the slice plane reflect the linear scanning paths of the laser. As summarized in Table 1, the specimens A1 to A4 were built by increasing laser power and energy density, respectively. This increase led to a change from S-shaped grains to rectangular grains in the slice plane (cp. Fig. 2).

In the building direction, we found elongated grains characteristic for SLM fabrication. Below a laser power of 80 W, their cross-sectional shape was rather irregular, whereas at higher laser powers the columnar microstructure was well established. An increasing amount of pores interrupted the regular columnar grains with increasing energy density. Accordingly, the material densities of the NiTi cylinders of specimens in groups A and B decreased. For specimens A1 to A5, the relative densities corresponded to 99.0, 97.6, 95.9, 91.6 and 89.2%, respectively. The relative densities of the specimens B1 to B5 decreased with the exposure time, here the densities referred to 95.6, 94.6, 94.0, 92.3 and 93.2%, respectively. The experimentally derived maximal error for the relative densities corresponded to ±0.6%.

Fig. 3 summarizes the linear dimensions of the grains, i.e. grain lengths and grain widths as a function of laser power and exposure time. These quantities, represented on a logarithmic scale, increased with the laser power, but not with the exposure time. Resulting from the rise in laser power from 56 to 92 W, the mean grain width increased by a factor of three, from (33 ± 7) to (94 ± 17) μm. The mean grain length even rose by a factor of ten, from (61 ± 19) to (655 ± 220) μm. It should be noted that the micrographs of specimen A5 contained so many pores that a meaningful quantification of the grain size was impossible. The specimens B1 to B5 exhibited mean grain widths independent on the selected exposure times, cp. right graph of Fig. 3. In the group B, the average grain width corresponded to (82 ± 11) μm and the average grain length to (630 ± 270) μm. The grain size G defined by the ASTM E112 [13] accounts to 6 for specimen A1, 4.5 for specimen A2 and to values between 1.5 and 2.5 for the other NiTi cylinders of groups A and B.

The characterization of the microstructure embraces not only the average grain sizes but also their size distribution, here determined in the slice plane, i.e. for the grain widths. For specimen A1 with an average grain width below 40 μm, a declining distribution was found (see Fig. 4, left graph). For specimens with an average grain width of more than 60 μm, i.e. A3, A4, and B1 to B5, the distribution was bimodal (see Fig. 4, right graph). For specimens with a mean grain width between 40 and 60 μm, such as for specimen A2, one may term the behavior transitional, as a peak above the average value of (44 ± 11) μm developed, see graph in the center of Fig. 4. Error bars in the size distribution were determined by varying the class width between 20 and 29 μm.

In order to check, whether the specimens' diameter influences the microstructure of the selective laser melted NiTi, cylinders 1 mm in diameter (specimens D1, D2 and D3) were built as well. As shown in the left optical micrograph of Fig. 5, one finds the checkerboard grain structure for linear laser paths (specimen D2) well comparable to the specimen B4 built with the same set of SLM process parameters but 7 mm in diameter. Using the same SLM process parameters but circular scanning paths within the hatch we have found concentrically arranged grains (specimen D3), as represented in the right optical micrograph of Fig. 5. For the two selected scanning paths, the grains exhibited a shape and size confined by the distance between the individual hatch vectors. Besides these grains of hatch distance width (about 120 μm) in the inner part of the slice plane, a prominent zone

Slice plane	Plane in building direction
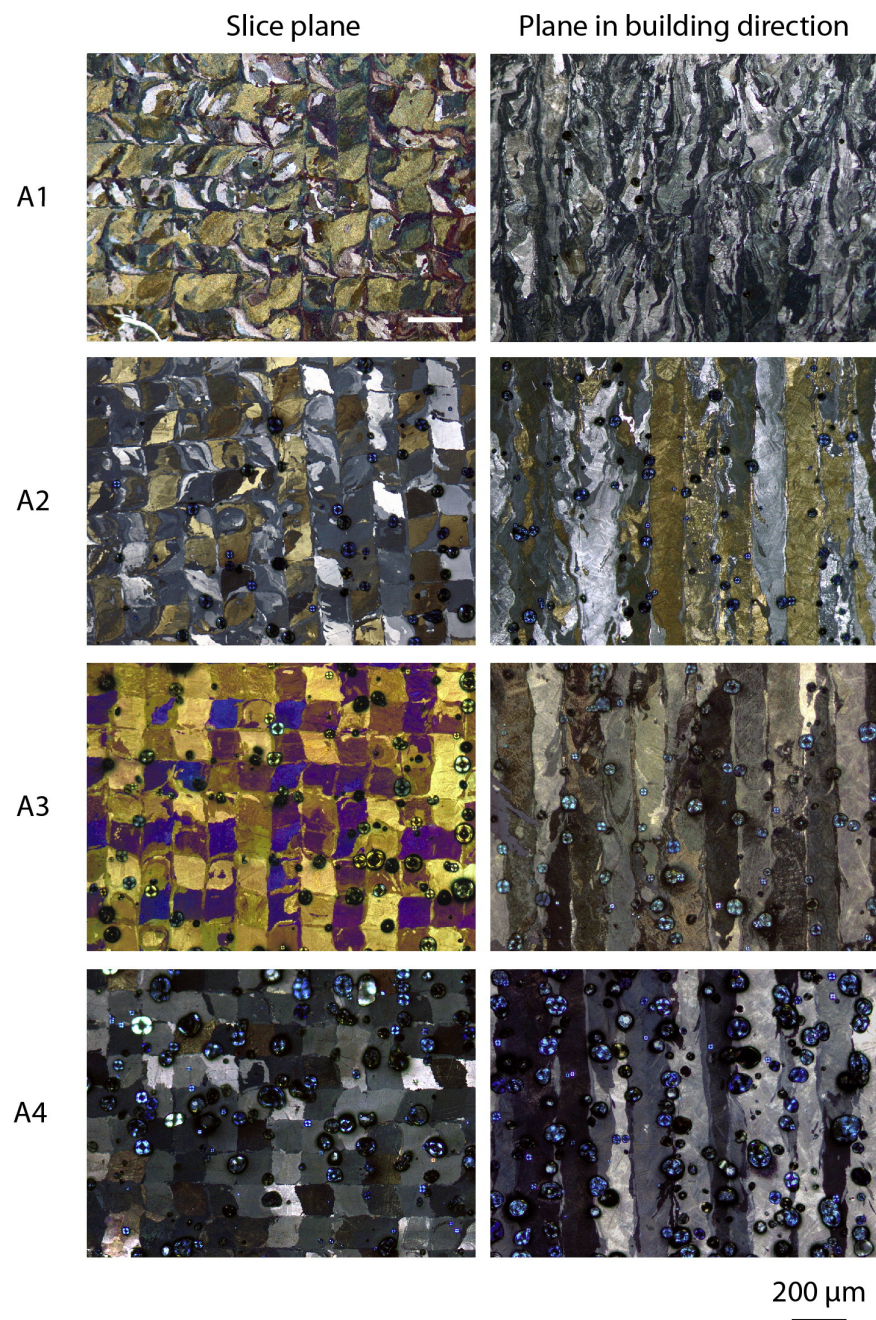
Fig. 2 – The optical micrographs show the anisotropic grain structure of selective laser-melted NiTi cylinders according to the linear laser scanning paths. The laser power was 56, 68, 80 and 92 W for specimens A1 to A4. This increase gives rise to enlarged grain widths and lengths. Simultaneously, the grains elongated along the building direction, became more regular and pores of a significant amount formed.

of relatively small grains (17 ± 5) μm in width appeared at the cylindrical surface of the NiTi cylinders, which corresponds to the scanning path of the boundary.

Another selective laser-melted NiTi cylinder with a diameter of 1 mm (specimen D1, Fig. 6), prepared using the SLM process parameters of specimen A4, was employed to gain insight into the grain orientation by means of EBSD. Fig. 6

contains the optical micrograph as well as the obtained EBSD grain maps according to the inverse pole figures [31] and the Euler angles [32]. The grain maps allow for a clearer discrimination of individual grains. Some grains hardly distinguishable within the optical micrograph come to light. For example, the Euler angle representation allows for the identification of the laser scanning paths even for the interrelated area on the left
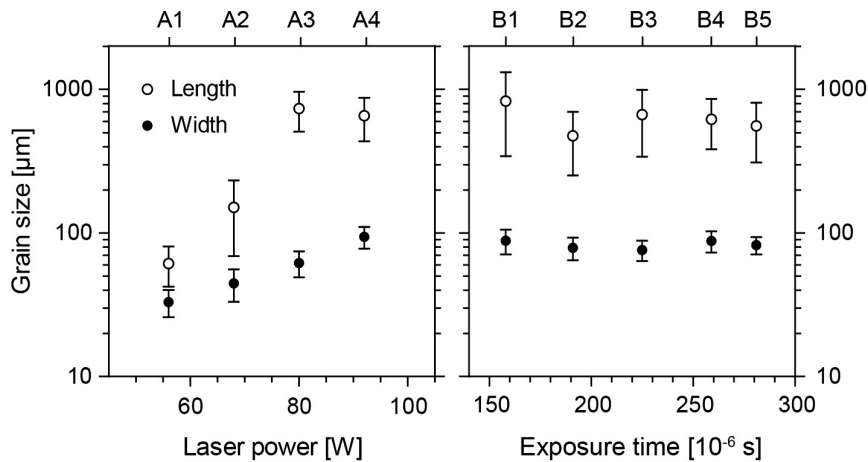
Fig. 3 – Grain sizes derived from the optical micrographs: By increasing the laser power, the grains become larger, whereas the exposure time does not alter the grain size.

(dark blue color in the optical micrograph and red color in the inverse pole figure representation). Further, intra-granular, local variations of the crystal lattice orientation are revealed by the hues within single grains. Nevertheless, the EBSD data confirmed the results obtained by conventional metallography as both techniques visualize the grains and their arrangement in both the large-grained hatch and the fine-grained boundary region. Because of the geometry in the experimental setup, the EBSD grain maps were distorted. Therefore, they were corrected by affine registration [33] with respect to the optical micrograph of the same specimen.

Fig. 7 shows EBSD grain maps of three selected specimens of groups A and B and the related pole figures. For specimens B1 and A4 with the larger grains, the blue color, which corresponds to a <111> alignment in the building direction, is dominant. For the finer grained specimen A1, we did not detect a preferred <111> orientation of crystallites in the building direction. For the three selected specimens, the texture increased with the laser power, since the maximal

multiples of random pole density values raised from 2.47 in specimen A1 via 4.42 in specimen B1 to 6.38 in specimen A4.

Frequently, relatively small, slim grains aligned in between the rectangular ones were found. They occur along the centerlines of the scanning tracks. Their color in the grain maps is generally red, indicating their preferential <100> orientation in building direction.

3.2. Thermal characterization

The SLM-fabricated specimens in as-built and annealed states exhibited transformation temperatures, which were compared to the starting material prior to atomization, see Tables 2 and 3. Errors for the phase transformation temperatures refer to the maximal standard deviation of the phase transformation temperatures of the NiTi cylinders of the two batches produced at the same parameter set. As the phase transformation temperatures depend on the ratio of Ni to Ti, this phenomenon can be mainly attributed to the preferential evaporation of Ni from the NiTi alloy
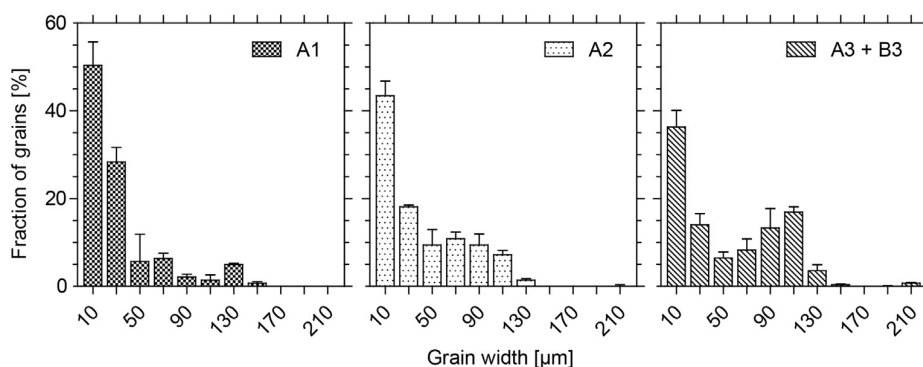
Fig. 4 – Grain-width distributions determined within the slice plane: The average grain widths for specimens A1, A2 and A3 + B3 correspond to (33 ± 7), (44 ± 11) and (68 ± 15) μm, respectively. This increase in average grain width is associated with a change from the uni- to the bimodal distribution.
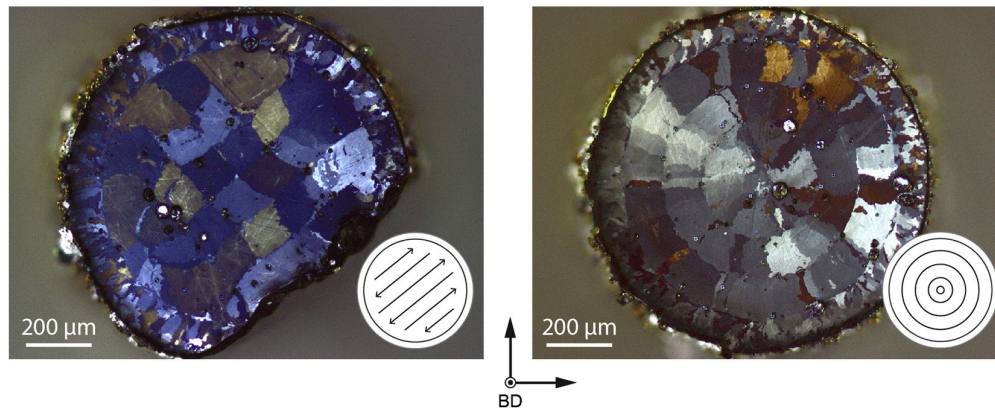
Fig. 5 – The optical micrographs of the slice planes of specimens D2 (left) and D3 (right) exhibit an arrangement of grains approximately 120 μm wide according to the linear and circular scanning paths. The boundaries of the specimens consist of smaller grains with sizes between 12 and 22 μm.

during the laser manufacturing process [5,6]. Heat exchange values during the phase transformation are likewise listed in Tables 2 and 3.

For the as-built specimens, the M_s values of specimens A1 to A5 corresponded to (14 ± 3) °C, while these specimens in solution annealed state showed M_s values of (-2 ± 6) °C. For specimens C1/C2 and B1 to B5, i.e. the specimens where the exposure time was controlled from about 100 to 300 μs, the M_s values in the as-built specimens rose from about 0 to more than 20 °C and in the annealed specimens from about −25 to 6 °C. Hence, the Ni loss does not show a systematic dependency on the applied laser power but on the applied exposure time.

As the relationship between phase transformation temperatures and the Ni-content is well known [25], one can calculate the Ni loss during SLM. The Ni-loss was calculated based on the data of the solution-annealed specimens.

Because the transformation peaks of the SLM-specimens are broad, we determined the maximal amount of the evaporated Ni by using only M_s, which corresponds to the upper limit of the broadened phase transformation range, as starting value for the calculations. From M_s, the relative Ni-content (Ni_{Ms}) in the NiTi-matrix, i.e. the NiTi undergoing the phase transformation, was obtained according to the data given by Frenzel et al. [25]. The relative Ti-content Ti_{Ms} is the result from $Ti_{Ms} = 100\% - Ni_{Ms}$. The obtained Ni_{Ms} and Ti_{Ms} values need to be corrected for Ti-rich inclusions (Ti_4Ni_2O and TiC) and the hydrogen content [25], as these impurities contribute to the atomic composition of the resulting selective laser-melted NiTi but not to the phase transformation.

The oxygen and hydrogen contents were measured at the annealed specimens. The oxygen content referred to (0.13 ± 0.02) wt.% independent on the applied processing parameters and the hydrogen content was found to be negligibly small. For the carbon content, no increase during SLM processing was detected in exemplary measurements. This is the reason why the carbon content of the starting material prior to atomization was used for the estimations.

The actual, corrected composition of the selective laser-melted NiTi was determined in the following way. First, transforming the stoichiometry of the Ti-rich inclusions, Ti_4Ni_2O and TiC, into weight stoichiometry yielded $Ti_{11.97}Ni_{7.34}O$ and $Ti_{3.98}C$, respectively. Second, the additional Ni- and Ti-fractions (Ni_{plus}, Ti_{plus}), which were caused by these impurities, were calculated in weight percent by

$$Ni_{plus} = x_O * 7.34$$
$$Ti_{plus} = x_O * 11.97 + x_C * 3.98$$

where x_O and x_C are oxygen and carbon contents in weight percent, respectively.

Third, the relative fraction X_{NiTi} of the NiTi-matrix was determined by

$$X_{NiTi} = (100 - x_O - x_C - x_H - Ni_{plus} - Ti_{plus})/100$$

with x_H as the hydrogen content in weight percent. Finally, we computed the actual Ni- and Ti-contents by

$$Ni_{SLM} = Ni_{Ms} * X_{NiTi} + Ni_{plus}$$
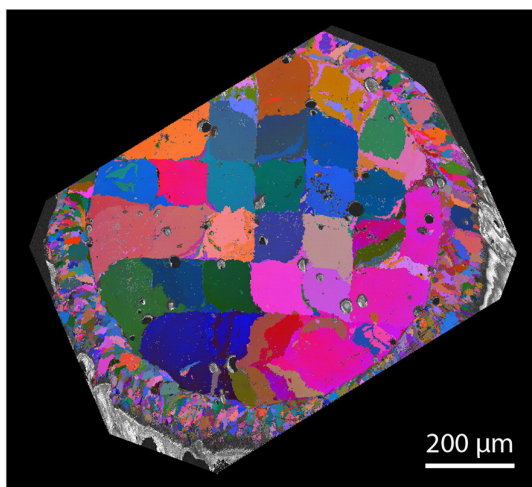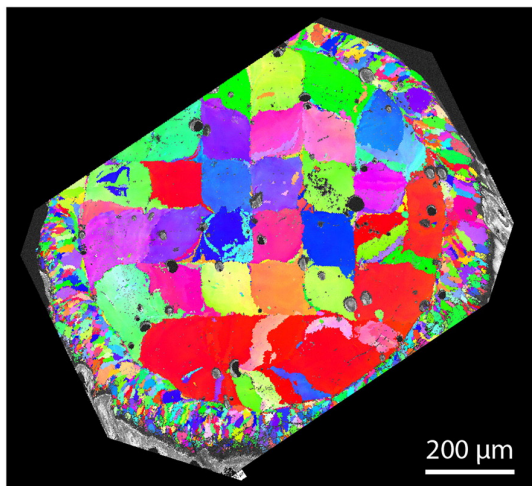$$Ti_{SLM} = Ti_{Ms} * X_{NiTi} + Ti_{plus}.$$

From the calculated composition of the selective laser-melted NiTi and the composition of the starting material, we calculated the Ni-loss caused by SLM relative to the Ni-content of the starting material prior to atomization (ΔNi). Here, we used the normalized amounts of Ni and Ti in selective laser-melted NiTi and in the starting material ($Ni_{SLM-norm}$, $Ti_{SLM-norm}$, $Ni_{start-norm}$, $Ti_{start-norm}$) without the C-, O-, and H-contents. The amount of Ni in the SLM-material supposing no Ni had evaporated ($Ni_{SLM-start}$) was calculated by normalizing the ratio of $Ni_{SLM-norm}/Ti_{SLM-norm}$ to the initial Ti-content by

$$Ni_{SLM-start} = (Ni_{start-norm} * Ti_{SLM-norm})/Ti_{start-norm}.$$

We assumed that the SLM process does not affect the Ti-content. In the final step, we determined the relative Ni-loss (ΔNi) referencing the Ni-fraction of the starting material according to

$$\Delta Ni = (Ni_{SLM-start} - Ni_{SLM-norm})/Ni_{SLM-start}.$$

The obtained quantities of the Ni-content based on M_s (Ni_{Ms}) and the maximal Ni-loss (ΔNi) during the SLM fabrication are listed in Table 3.

Fig. 6 – On top, the optical micrograph of specimen D1 is represented. Below, the electron backscatter diffraction grain maps of this specimen are visualized. The color in the central image relates to the inverse pole figure, explanation given in Fig. 7. The colors in the image on the bottom correspond to the Euler angles. The grain maps were rectified by means of affine registration with the optical micrograph. (For interpretation of the references to color in this figure legend, the reader is referred to the web version of this article.)
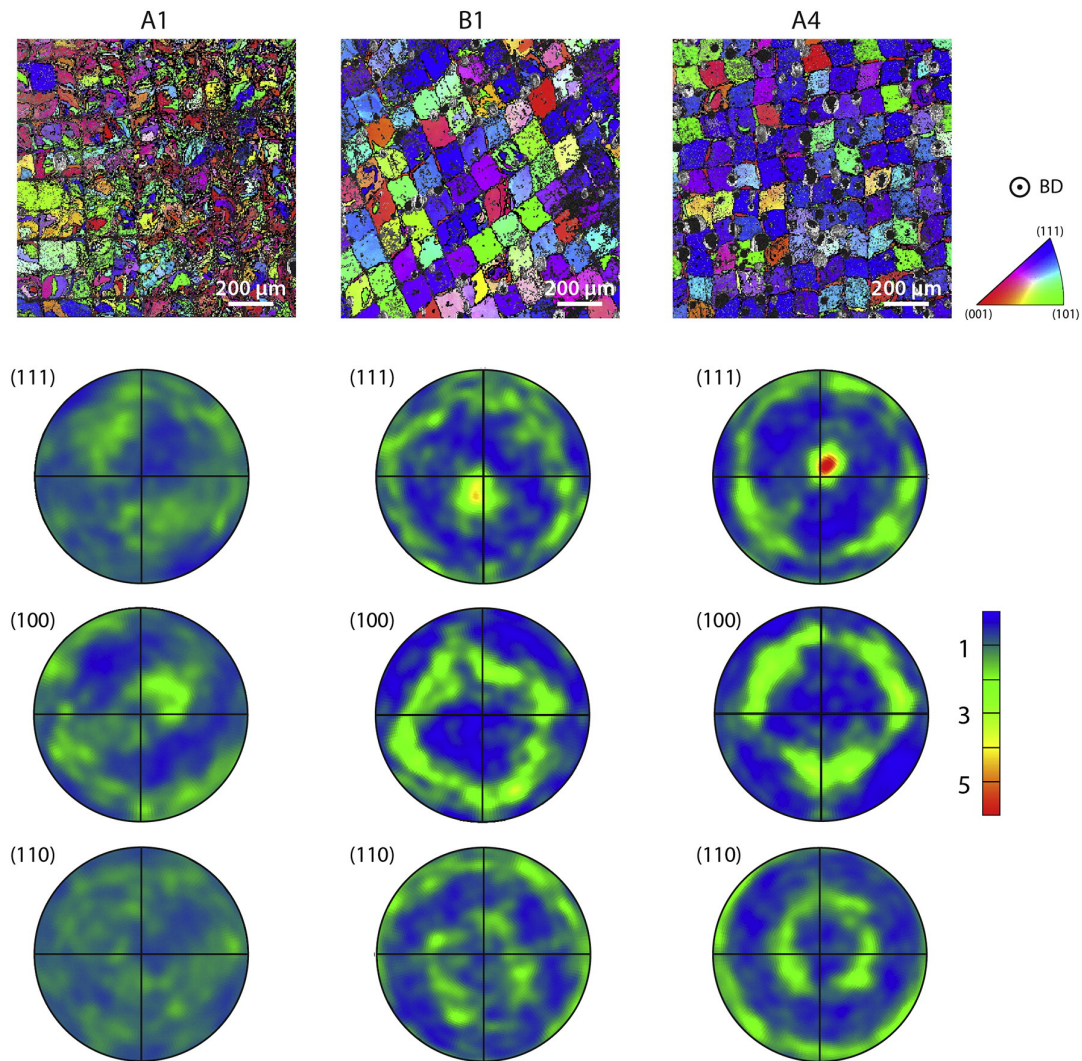
4. Discussion

Evaporation of Ni was demonstrated for all specimens of the groups A, B and C. For the specimens of groups C and B, which showed a rise in Ni-loss with the increasing exposure time, the ratio of evaporated Ni and exposure time ($\Delta Ni/t_e$) decreased with the exposure time. This observation indicates a time-dependent Ni-evaporation, which means that the Ni-loss decreases during laser irradiation. Several scenarios can explain the time-dependence of Ni-evaporation. For example, the formation of oxides on top of the melt pool [34] could impede the Ni-evaporation. Also, depletion of Ni in the surface region of the melt pool might only be incompletely compensated by diffusion processes or Marangoni convection [34] due to the rapid solidification of the melt. Ascending laser power is often associated with increasing track width and melt pool temperatures [35–37]. For both phenomena one expects increasing Ni-evaporation. However, this was not found in this study. Because the vaporization rate is an exponential function of the temperature in the melt [38], we expect that just the hottest area of the melt pool contributes to the evaporation of Ni. As the width of the molten track refers to more than 120 µm, while the diameter of the focused laser beam accounts to 50 to 60 µm [27], we conclude that the evaporation of Ni mainly takes place in the area directly exposed to the laser beam. Track widening due to the higher laser power input would therefore not cause an increase in Ni-evaporation. Consequently, the increasing laser power rather leads to an expansion of the path width than it raises the melt pool temperature.

The preferential Ni depletion from the melt pool surface as well as from the directly irradiated central part of the melt pool would further lead to local differences in the Ni/Ti ratio. The broad transformation peaks of about (41 ± 10) K and (42 ± 10) K for the austenite and martensite transformations in the annealed specimens, respectively, can therefore be explained by local concentration differences in the NiTi matrix. Still, aside from a varying Ni/Ti ratio, also other defects in the specimens, such as the presence of inclusions, dislocations or internal stresses might hamper the phase transformation and therefore attribute to the broad transformation ranges.

The calculated maximal Ni-loss of about 2 to 3 at.% of the Ni-content of the starting material is referring to the local maximum of evaporated Ni atoms, because M_s was utilized to determine the Ni-loss, which corresponds to the upper limit of the broadened phase transformation range. This Ni-loss shifts M_s and A_f in the solution annealed specimens about 30 K towards higher values (cf. Table 3). At first glance, this does not seem reasonable since one would expect clearly

BD

Fig. 7 – Grain maps from electron backscatter diffraction (inverse pole figure color coding in the out-of-plane direction) and derived pole figures of the specimens A1 (left column), B1 (middle column) and A4 (right column). Grain maps and pole figures show an increase of crystals oriented with <111> parallel to the building direction with laser power increasing from 56 to 92 W. The center of the pole figure is oriented in building direction. The color scale refers to multiples of the uniform pole density. (For interpretation of the references to color in this figure legend, the reader is referred to the web version of this article.)

higher transformation temperatures resulting from a Ni-loss of about 1.0 to 1.5 at.% referring to the complete alloy. Yet, the Ni-loss is compensated by the formation of Ti-rich oxides and carbides. Our calculations regarding the Ni-loss are based on the approach of Frenzel et al. [25] to determine the Ni-concentration in the actual NiTi-matrix with respect to titanium and nickel consuming inclusions in the complete alloy. The assumptions are that the solubility of oxygen and carbon in solid NiTi is nearly zero and that oxygen and carbon pick up leads to the formation of Ti_4Ni_2O and TiC, respectively (cf. [25] and references therein). Residual oxygen and carbon atoms in solution, however, might have an influence on the transformation temperatures as well, which was not considered in this study. Even though the tendency for the shift in

the transformation temperatures with increasing exposure times remained after solution annealing, the transformation temperatures in the solution-annealed specimens are generally lower than the transformation temperatures in the as-built specimens. This decrease can be explained by an increase in the oxygen-content during the annealing procedure, as reported previously [6]. Additional oxygen leads to the formation of Ti_4Ni_2O [25], which reduces the Ti-content in the NiTi matrix and lowers the transformation temperatures [6]. Other aspects potentially influencing the phase transformation, for example a change in the number of dislocations, varying grain sizes or residual internal stresses, cannot be fully excluded and may therefore also play a role in the observed variation of the phase transformation temperatures.

Table 2 – The as-built specimens exhibit phase transformation temperatures with errors of ±4 K for M_s, ±5 K for A_s and ±10 K for M_f and A_s. Further, the heat exchange during forward and reverse phase transformation is given.

	M_s [°C]	M_f [°C]	A_s [°C]	A_f [°C]	ΔH_A [J/g]	ΔH_M [J/g]
Starting material	−31	−48	−23	−10	14.6 ± 1.0	14.5 ± 1.0
A1	16	−53	−28	38	17.0 ± 3.0	15.8 ± 3.0
A2	10	−48	−11	29	17.0 ± 3.0	15.4 ± 3.0
A3	18	−37	−6	40	18.5 ± 3.0	17.3 ± 3.0
A4	13	−40	−6	32	12.7 ± 3.0	15.4 ± 3.0
A5	13	−58	−20	32	14.3 ± 3.0	13.7 ± 3.0
C1	0	−84	−37	2	11.4 ± 3.0	8.9 ± 3.0
C2	−3	−81	−34	5	10.9 ± 3.0	9.3 ± 3.0
B1	1	−61	−16	15	15.4 ± 3.0	12.7 ± 3.0
B2	9	−44	−11	27	16.2 ± 3.0	14.3 ± 3.0
B3	16	−39	−10	37	16.4 ± 3.0	13.7 ± 3.0
B4	23	−29	7	47	17.0 ± 3.0	16.8 ± 3.0
B5	21	−41	1	40	15.2 ± 3.0	13.8 ± 3.0

The spherical pores, which go along with increasing porosity due to raised laser power can be prominently seen from Fig. 2. The metallographic preparation for light optical microscopy, however, overestimates the pore sizes, because electro-polishing induces a preferential rounding of edges, which leads to an increase of the pore area visualized in the optical micrographs. The spherical shape and the smooth surface of the pores correspond to the morphology of gas pores. Gases dissolved in the melt pool are segregating because of the decreasing solubility of gases in the melt during solidification. The raised laser power or longer exposure times generate an increasing melt pool volume. This behavior, in turn, causes a higher amount of pores, because the diffusion of emerging gas bubbles towards the melt pool surface is progressively hindered during solidification. We have to clarify, however, that (i) the actual pore size is not measured on non-electro-polished samples, (ii) the origin of the gas inside the melt pool is not determined, and (iii) the possibility of the formation of keyhole melt pools, which may result in large pores, is not considered. Hence, this study only allows for conclusions on the pore density and not on the pore shapes, pore sizes, and pore size distributions.

Intensifying laser power and growing exposure time introduced distinct changes to the NiTi-alloy while both parameters raise the integral parameter energy density E (Eq. (1)). The investigation of the individual SLM processing parameters rather than the investigation of the integral parameter E onto resulting material properties is therefore rational.

The light optical micrographs reveal elongated grains in the building direction, which are characteristic for SLM because the grains grow in the direction opposite to the heat transfer [19]. The length of the observed columnar grains exceeds the slice thickness of 50 μm, which indicates epitaxial grain growth from the partially re-melted substrate during scanning of each slice [21,39]. In the slice plane perpendicular to the building direction, the checkerboard grain arrangement also indicates the epitaxial growth, because the grains adopt the linear arrangement from the preceding layers.

In order to quantify the regularly arranged grains, we analyzed light optical micrographs in the reciprocal space. Light optical images of the specimens A3, A4 and B1–B5, which exhibit the larger columnar grains, were Fourier transformed and averaged to generalize the findings from the individual specimens. Fig. 8 exhibits the averaged two-dimensional fast Fourier transforms (FFT) of eight images each from the slice planes and from the planes in the building direction. The Fourier transform of the slice plane reveals the checkerboard pattern: frequency maxima along both orthogonal directions, q_x and q_y, refer to repetition lengths of 240, 120 and 80 μm. The values of 240 and 120 μm reflect the distance between the scanning paths, which defines the grain width. The repetition length of 80 μm reproduces the average grain width of specimens A3, A4, and B1 to B5 determined via linear interception, which amounts to (81 ± 30) μm. The image analysis in the reciprocal space, therefore, results in additional information on the periodic grain arrangement according to the laser path, while the average grain size determination via linear interception yields only the mean grain size.

The averaged Fourier transform of the light optical micrographs parallel to the building direction (cp. Fig. 8, right)

Table 3 – In the solution annealed specimens, the measured phase transformation temperatures with an error of ±3 K for M_s and A_f and ±10 K for M_f and A_s, and the Ni-contents related to M_s allow for the estimation of the maximal Ni-losses during the SLM process. Further, the heat exchange during forward and reverse phase transformation is given.

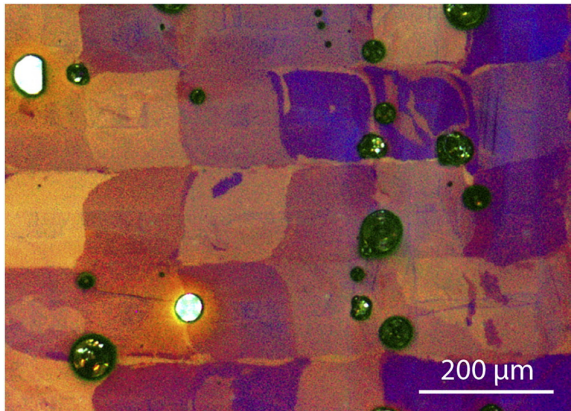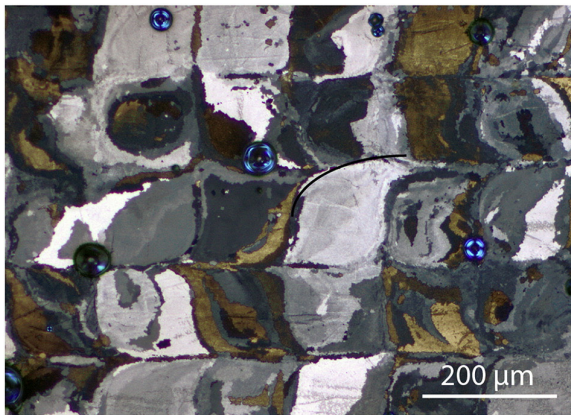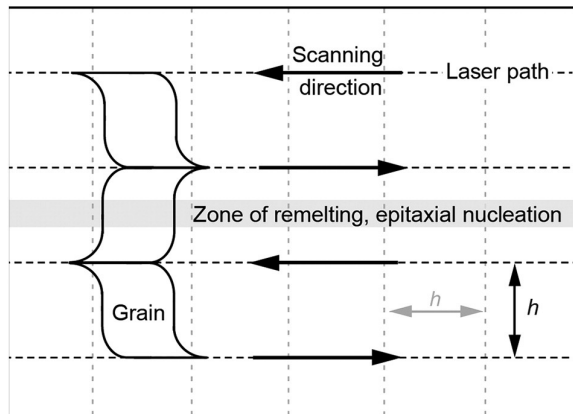|	M_s [°C]	M_f [°C]	A_s [°C]	A_f [°C]	Ni_{Ms} [at.%]	ΔNi_{max} [at.%]	ΔH_A [J/g]	ΔH_M [J/g]
Starting material	−31	−48	−23	−10	51.05		14.6 ± 1.0	14.5 ± 1.0
A1	−6	−54	−28	18	50.83 ± 0.03	2.42 ± 0.39	16.5 ± 2.0	13.6 ± 2.0
A2	−7	−31	−51	16	50.84 ± 0.03	2.37 ± 0.39	8.1 ± 6.0	5.7 ± 6.0
A3	8	−32	−6	30	50.69 ± 0.03	2.95 ± 0.39	18.6 ± 6.0	15.7 ± 6.0
A4	−1	−46	−20	22	50.78 ± 0.03	2.61 ± 0.39	16.3 ± 2.0	12.9 ± 2.0
A5	−2	−61	−15	22	50.79 ± 0.03	2.56 ± 0.39	16.3 ± 2.0	10.6 ± 2.0
C1	−25	−62	−38	−2	50.99 ± 0.03	1.81 ± 0.37	14.7 ± 2.0	9.4 ± 2.0
C2	−22	−63	−41	1	50.97 ± 0.03	1.88 ± 0.37	14.1 ± 2.0	9.2 ± 2.0
B1	−16	−59	−39	9	50.92 ± 0.03	2.09 ± 0.37	14.2 ± 2.0	8.3 ± 2.0
B2	−3	−39	−10	22	50.79 ± 0.03	2.56 ± 0.39	18.3 ± 2.0	16.1 ± 2.0
B3	4	−30	−13	27	50.73 ± 0.03	2.80 ± 0.39	17.8 ± 2.0	14.0 ± 2.0
B4	6	−20	0	30	50.70 ± 0.03	2.90 ± 0.39	17.8 ± 2.0	13.3 ± 2.0
B5	−8	−49	−24	15	50.85 ± 0.03	2.12 ± 0.39	15.0 ± 2.0	9.9 ± 2.0
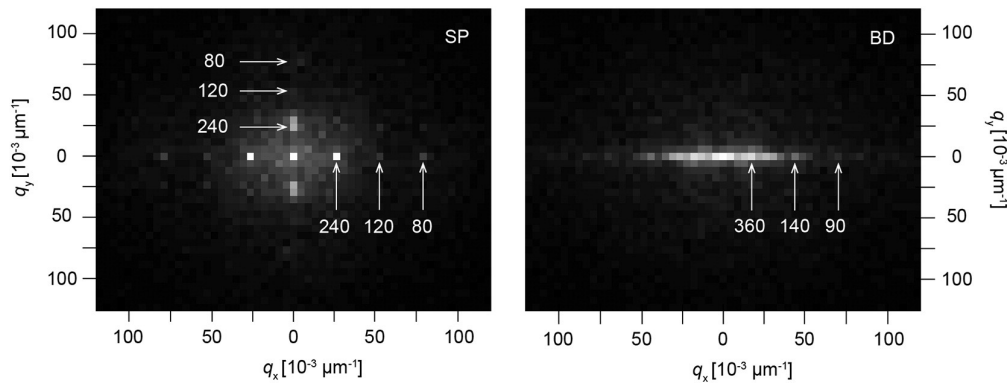
Fig. 8 – Averaged two-dimensional fast Fourier transforms (2D FFTs) of light optical micrographs reflect the checkerboard grain arrangement caused by 120 μm-spaced laser paths and the anisotropic grains of specimens A3, A4 and B1 to B5. The 2D FFTs of eight gray scale images were averaged for both planes, i.e. the slice plane (SP, left) and the plane in building direction (BD, right). Maxima in the frequency domain and associated periods in the real space (in μm) are indicated by arrows. Please refer to Fig. 2 for the light optical micrographs in real space.

clearly reflects the anisotropy of the grains. As the optical micrographs of elongated grains were subjected to FFT, no frequency maxima were detected along the building direction, i.e. along q_y. Transverse to the building direction, i.e. along q_x, frequency maxima corresponding to repetition lengths of 360, 140 and 90 μm occur. The repetition lengths differ from the ones detected in the slice planes, as the longitudinal sections were aligned parallel to the building direction but were not aligned on the orthogonal grid defined by the laser path in the slice plane. This leads to a superposition of apparently different grain widths and results in less pronounced maxima in the frequency domain.

From the rectangular cross sections of the columnar grains, we deduced the scanning pathway and direction of the focused laser beam, as schematically indicated in Fig. 9. Because the scanned tracks re-melt parts of the preceding tracks, the grains grow epitaxially, adopting the orientations of the grains from the preceding track. Grain growth occurs subsequently along the directed heat gradient towards the centerline of the melt pool. In the centerline, the grains, which have grown radially from the border of the curved melt-pool, finally confine each other. The scanned pathway thus refers to the line of grain boundaries stringed together. This observation shows that the solidification during SLM takes place track-wise, i.e. the preceding track is already solid by the time the subsequent track is scanned. Still, Thijs et al. interpreted a similar scanning pattern of SLM-produced Ti6Al4V slightly different. They concluded that the individual tracks of grains represent the scan vectors and that "The herringbone pattern is caused by the alternation of scanning direction. If the laser beam is moved from left to right, the grains are slanted as ///, from right to left as \\\\"[19]. From the reflected S-shape on both sides of the centerline of the scanned track, one can visually deduce the scanning direction of the laser beam (cp. Fig. 9). This is because the moving laser beam leads to a thermal gradient highest in the scanning direction [21,35], which is followed by the crystallizing grains. These mechanisms of grain alignment according to a moving heat source are similar to
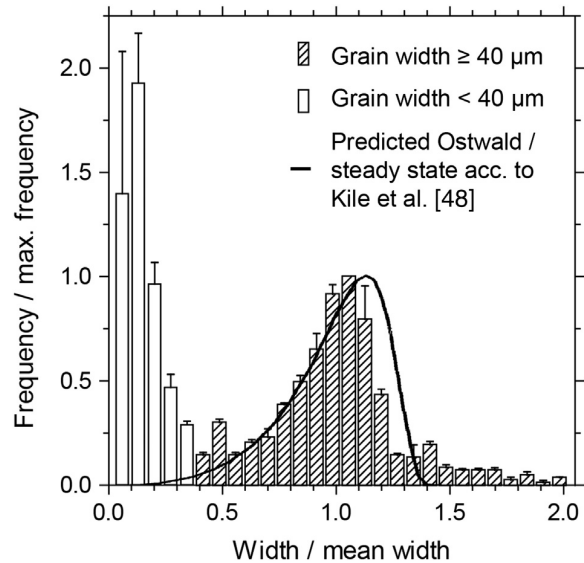
classical welding [22]. Furthermore, the small grains formed in between the square shaped columnar grains are known from welding metallurgy as *axial grains*, as further discussed below [22].

The specimens consist of much smaller grains at their outside, i.e. in the scanning path of the boundary (cp. Figs. 5, 6). This has been also observed by Thijs et al. in SLM-fabricated Ta and by Antonysamy et al. in electron beam melted Ti6Al4V [19,39]. We suspect that grains initially crystallized in the firstly scanned track of a slice are of the same size than the grains observed at the specimens outside. The reason is that the cooling and heat transfer conditions at the very outside of the specimen should be similar to the heat flow condition of the path scanned first in each slice. In both cases the crystallizing track is laterally confined by loose powder, which leads to a reduced heat flow by conduction. In our case, underneath the tracks, solid material is present. We believe that two processes cause the enlargement of the small grains during the SLM process. First, the grains enlarge due to epitaxial grain formation in combination with competitive growth [39,40]. This means that grains, which have a favored crystal orientation with respect to the heat gradient, grow preferentially at the expense of less favorably oriented grains. In cubic metals, the direction of preferential grain growth is generally referred to be <100> [22,41]. Grains with <100> aligned in the direction of the local heat gradient should therefore grow preferentially and enlarge. Second, Ostwald-ripening of crystallites can occur, which means that larger grains grow at the expense of smaller ones to reduce the amount of energy-expensive defects at the grain boundaries. This phenomenon is also studied for NiTi [42] and further binary alloys theoretically [43] and experimentally [44]. It gives rise to characteristic grain size distributions. Such a secondary grain growth (coarsening) is reasonable, as the crystallites adjacent to and underneath of the molten zones are repeatedly heated during the manufacturing process [35]. During nucleation and growth, i.e. a relatively fast process, an unstable solid state of relatively small grains forms. The energetically unstable grains start merging via diffusion and reaction accumulating in relatively large grains consistent with

Fig. 10 – **The integral grain size distribution of specimens A3, A4, B1 to B5 indicates that the grain population with widths above 40 μm evolved by Ostwald-ripening. The grain shape of the second peak can be represented by the predicted asymmetric shape of the crystallite size distribution of Ostwald-ripening according to Kile et al. [48]. For the representation on reduced axes, frequency and width were normalized to the population of larger grains. The mean grain width of this fraction referred to (105 ± 30) μm.**

Fig. 9 – **Top: Scheme to explain the formation of S-shaped grains, which is due to the alternating movement of the focused laser beam. Center: Light optical micrograph from the cross section along the slice plane of specimen A2. Bottom: Cross section along the slice plane of specimen B1, representative for the specimens of group B.**

the predictions of classical theory for one-component materials [43,45,46]. The observed bimodal grain size distribution, can, therefore, be explained by a superposition of conventional formation of relatively small grains during solidification and of Ostwald ripening (coarsening) resulting in relatively large grains.

If only the specimens with average grain widths larger than 60 μm (A3, A4, and B1 to B5) are analyzed, one finds the distribution characteristic for secondary grain growth (cp. Fig. 10) [47,48]. The distinctive feature of the bimodal size distribution is the negative skew towards smaller crystallites of the larger grain size population. This shape can be represented by the theoretical, steady-state curve for Ostwald-ripening as predicted by Kile et al. [48]. This behavior indicates that the grains in selective laser-melted NiTi, exceeding a width of 40 μm, were formed by secondary grain growth of small and energetically unstable grains after repeated heating. The threshold value of 40 μm corresponds to the minimum in between the two grain-size populations. Fig. 10 shows the bimodal grain size distribution on reduced axes, normalized with respect to the grain fraction ≥40 μm because the second peak comprises the enlarged, Ostwald-ripened grains. It should be noted that in the graph of the grain size distribution of Fig. 10, the grains exceeding two times width/mean width (12 out of 978 analyzed grains) were skipped.

Thijs et al. hypothesized that the amount of partial re-melting of neighboring tracks is responsible for the extent of the crystallographic texture [40]. This hypothesis is in line with our results, as we found an accumulation of <111>-oriented crystals in the building direction with increasing laser power. Selective laser-melted Ta also shows the preferred <111> orientation of crystals in the building direction [21]. Thijs et al. explained the orientation of <111> in building direction with the

locally varying heat flow. As the melt pool has a radial form, the dominant heat gradient occurs radially from the centerline to the melt pool border. They calculated the average angle of the local heat gradient and concluded that the alignment of grains with <100> along the averaged heat flow direction could turn the crystallites such that <111> appeared in the building direction [21]. Still, for other additively manufactured cubic metals including AlSi10Mg and β-TiAl6V4, <100> was found as preferred orientation in the building direction [39,40]. One has to note, however, that the formed texture depends on the local heat flow and the solidification mode, which can differ for materials mentioned above.

Another interesting observation from the EBSD grain maps in Fig. 7 is that the axial grains seem to show a preferential orientation in <100>. This means that they have a distinct orientation from the surrounding crystallites, which are preferably oriented along <111>. Antonysamy et al. also observed <100> oriented axial grains in electron beam melted Ti6Al4V growing from the bottom of the melt pool vertically in the building direction. The axial grains orient vertically along the preferred <100> growth direction, because this corresponds to the direction of the local heat flow between melt pool bottom and centerline [39]. As the path between melt pool bottom and centerline corresponds to the highest temperature gradient within the melt pool, the most stable solidification front can be found there. The axial grains might therefore comprise less intra-granular defects making them energetically favorable, which would prevent them from the dissolution and integration by the coarsening grains during the Ostwald-ripening process. The bimodal grain size distribution observed in specimens A3, A4 and B1 to B5 originates therefore from the proliferation of the grains larger than 40 μm due to Ostwald-ripening occurring during the SLM process and from the presence of the remaining rather small axial grains.

5. Conclusions

The control of laser power and scanning speed during SLM processing of NiTi impacts the microstructure in a distinct manner. The evaporation of Ni from the melt and the related phase transformation temperatures can be altered adjusting the scanning speed. The laser power affects grain size and porosity, as both increased considerably with a raise in laser power from 56 to 100 W. The results indicate that the lowest laser power within the investigated frame of processing parameters yields the best result regarding small grain sizes, a narrow grain size distribution and a low porosity of the specimens. Increasing the laser power results in a bimodal grain size distribution with a significant enlargement of grains, most likely due to Ostwald-ripening of crystallites during the SLM process. Despite the anisotropy, grain sizes of specimens A1 and A2 conform to the ASTM standard F2063-05 regarding NiTi alloys for medical devices. For medical applications, however, the oxygen contents should be lowered. Based on our experimental findings, systematic future investigations should be performed to develop a fine-grained, homogeneous microstructure with the mechanical properties required for medical implants.

REFERENCES

[1] Kruth JP, Froyen L, van Vaerenbergh J, Mercelis P, Rombouts M, Lauwers B. Selective laser melting of iron-based powder. J Mater Process Technol 2004;149(1–3):616–22.

[2] Meier H, Haberland C. Experimental studies on selective laser melting of metallic parts. Materialwiss Werkst 2008;39(9):665–70.

[3] Murr LE, Esquivel EV, Quinones SA, Gaytan SM, Lopez MI, Martinez EY, Medina F, Hernandez DH, Martinez E, Martinez JL, Stafford SW, Brown DK, Hoppe T, Meyers W, Lindhe U, Wicker RB. Microstructures and mechanical properties of electron beam-rapid manufactured Ti–6Al–4V biomedical prototypes compared to wrought Ti–6Al–4V. Mater Charact 2009;60(2):96–105.

[4] Mullen L, Stamp RC, Brooks WK, Jones E, Sutcliffe CJ. Selective laser melting: a regular unit cell approach for the manufacture of porous, titanium, bone in-growth constructs, suitable for orthopedic applications. J Biomed Mater Res B 2009;89(2):325–34.

[5] Meier H, Haberland C, Frenzel J, Zarnetta R. Selective laser melting of NiTi shape memory components. Innovative Developments in Design and Manufacturing: Advanced Research in Virtual and Rapid Prototyping. Boca Raton: CRC Press-Taylor & Francis Group; 2010 233–8.

[6] Bormann T, Schumacher R, Müller B, Mertmann M, de Wild M. Tailoring selective laser melting process parameters for NiTi implants. J Mater Eng Perform 2012;21(12):2519–24.

[7] Habijan T, Haberland C, Meier H, Frenzel J, Wittsiepe J, Wuwer C, Greulich C, Schildhauer TA, Köller M. The biocompatibility of dense and porous nickel–titanium produced by selective laser melting. Mater Sci Eng C 2013;33(1):419–26.

[8] Bansiddhi A, Sargeant TD, Stupp SI, Dunand DC. Porous NiTi for bone implants: a review. Acta Biomater 2008;4(4):773–82.

[9] Liu X, Wu S, Yeung KWK, Chan YL, Hu T, Xu Z, Liu X, Chung JCY, Cheung KMC, Chu PK. Relationship between osseointegration and superelastic biomechanics in porous NiTi scaffolds. Biomaterials 2011;32(2):330–8.

[10] Liu Y, van Humbeeck J. On the damping behaviour of NiTi shape memory alloy. J Phys IV France 1997;7:510–24 (Colloque C5, Supplement au, Journal de Physique III).

[11] Es-Souni M, Es-Souni M, Fischer-Brandies H. Assessing the biocompatibility of NiTi shape memory alloys used for medical applications. Anal Bioanal Chem 2005;381:557–67.

[12] Petch NJ. The cleavage strength of polycrystals. J Iron Steel Inst 1953;174:25–8.

[13] ASTM Standard F 2063-05. Standard Specification for Wrought Nickel–Titanium Shape Memory Alloys for Medical Devices and Surgical Implants. Astm International; 2005.

[14] ASTM Standard E 112-96. Standard Test Methods for Determining Average Grain Size. Astm International; 2004.

[15] Thompson AW, Backofen WA. The effect of grain size on fatigue. Acta Metall 1971;19(7):597–606.

[16] Rodopoulos CA, Chliveros G. Fatigue damage in polycrystals — part 1: the numbers two and three. Theor Appl Fract Mech 2008;49(1):61–76.

[17] Mughrabi H, Höppel HW. Cyclic deformation and fatigue properties of very fine-grained metals and alloys. Int J Fatigue 2010;32(9):1413–27.

[18] Elahinia MH, Hashemi M, Tabesh M, Bhaduri SB. Manufacturing and processing of NiTi implants: a review. Prog Mater Sci 2011;57(5):911–46.

[19] Thijs L, Verhaeghe F, Craeghs T, Humbeeck JV, Kruth J-P. A study of the microstructural evolution during selective laser melting of Ti–6Al–4V. Acta Mater 2010;58(9):3303–12.

[20] Chlebus E, Kuznicka B, Kurzynowski T, Dybala B. Microstructure and mechanical behaviour of Ti–6Al–7Nb alloy produced by selective laser melting. Mater Charact 2011;62(5):488–95.

[21] Thijs L, Montero Sistiaga ML, Wauthle R, Xie Q, Kruth J-P, van Humbeeck J. Strong morphological and crystallographic texture and resulting yield strength anisotropy in selective laser melted tantalum. Acta Mater 2013;61(12):4657–68.

[22] Kou S. Welding Metallurgy. second ed. Hoboken, New Jersey: John Wiley & Sons, Inc.; 2003.

[23] Liu ZH, Zhang DQ, Chua CK, Leong KF. Crystal structure analysis of M2 high speed steel parts produced by selective laser melting. Mater Charact 2013;84:72–80.

[24] Ng CC, Savalani MM, Lau ML, Man HC. Microstructure and mechanical properties of selective laser melted magnesium. Appl Surf Sci 2011;257(17):7447–54.

[25] Frenzel J, George EP, Dlouhy A, Somsen C, Wagner MF-X, Eggeler G. Influence of Ni on martensitic phase transformations in NiTi shape memory alloys. Acta Mater 2010;58:3444–58.

[26] Bormann T, de Wild M, Beckmann F, Müller B. Assessing the morphology of selective laser melted NiTi-scaffolds for a three-dimensional quantification of the one-way shape memory effect. Proc SPIE 2013;8689:868914.

[27] Haberland C. Additive Verarbeitung von NiTi-Formgedächtniswerkstoffen mittels Selective Laser Melting [PhD]. Bochum, Germany: Ruhr-Universität Bochum; 2012.

[28] Schumann H, Oettel H. Metallografie. Wiley-VCH; 2005.

[29] Escher K, Huhner M. Metallographical preparation of NiTi shape memory alloys. Prakt Metall Pract Metall 1990;27(5):231–5.

[30] Schinhammer M, Pecnik CM, Rechberger F, Hänzi AC, Löffler JF, Uggowitzer PJ. Recrystallization behavior, microstructure evolution and mechanical properties of biodegradable Fe–Mn–C(–Pd) TWIP alloys. Acta Mater 2012;60(6–7):2746–56.

[31] Garcia CB, Ariza E, Tavaresa CJ, Villechaised P. Electron backscatter diffraction analysis of ZnO:Al thin films. Appl Surf Sci 2012;259:590–5.

[32] König U, Davepon B. Microstructure of polycrystalline Ti and its microelectrochemical properties by means of lectron-backscattering diffraction (EBSD). Electrochim Acta 2001;47:149–60.

[33] Germann M, Morel A, Beckmann F, Andronache A, Jeanmonod D, Muller B. Strain fields in histological slices of brain tissue determined by synchrotron radiation-based micro computed tomography. J Neurosci Methods 2008;170(1):149–55.

[34] Louvis E, Fox P, Sutcliffe CJ. Selective laser melting of aluminium components. J Mater Process Technol 2011;211(2):275–84.

[35] Li R, Shi Y, Liu J, Yao H, Zhang W. Effects of processing parameters on the temperature field of selective laser melting metal powder. Powder Metall Met Ceram 2009;48(3–4):186–95.

[36] Furumoto T, Ueda T, Tsukamoto T, Kobayashi N, Hosokawa A, Abe S. Study on laser consolidation of metal powder with Yb:fiber laser–temperature measurement of laser irradiation area. JLMN 2009;4(1):22–7.

[37] Yadroitsev I, Gusarov A, Yadroitsava I, Smurov I. Single track formation in selective laser melting of metal powders. J Mater Process Technol 2010;210(12):1624–31.

[38] DebRoy T, David SA. Physical processes in fusion welding. Rev Mod Phys 1995;67(1):85–112.

[39] Antonysamy AA, Meyer J, Prangnell PB. Effect of build geometry on the beta-grain structure and texture in additive manufacture of Ti6Al4V by selective electron beam melting. Mater Charact 2013;84:153–68.

[40] Thijs L, Kempen K, Kruth J-P, van Humbeeck J. Fine-structured aluminium products with controllable texture by selective laser melting of pre-alloyed AlSi10Mg powder. Acta Mater 2013;61(5):1809–19.

[41] Glicksman ME. Principles of Solidification. New York Dordrecht Heidelberg London: Springer; 2011.

[42] Kompatscher M. Phase Separation in Ni-rich Ni–Ti: The Metastable States. Zürich, Switzerland: ETH; 2001.

[43] Burlakov VM, Kantorovich L. Ostwald ripening of binary alloy particles. J Chem Phys 2011;134:024521.

[44] Garay-Reyes CG, Hernández-Santiago F, Cayetano-Castro N, López-Hirata VM, Garcia-Rocha J, Hernández-Rivera JL, Dorantes-Rosales HJ, Cruz-Rivera JJ. Study of phase decomposition and coarsening of γ′ precipitates in Ni–12 at.% Ti alloy. Mater Charact 2013;83:35–42.

[45] Lifshitz LM, Slyozov VV. The kinetics of precipitation from supersaturated solid solutions. J Phys Chem Solids 1961;19:35–50.

[46] Wagner C. Theorie der Alterung von Niederschlägen durch Umlösen. Z Elektrochem 1961;65:581–91.

[47] Eberl DD, Drits VA, Srodon J. Deducing growth mechanisms for minerals from the shapes of crystal size distribution. Am J Sci 1998;298:499–533.

[48] Kile DE, Eberl DD, Hoch AR, Reddy MM. An assessment of calcite crystal growth mechanisms based on crystal size distributions. Geochim Cosmochim Acta 2000;64(17):2937–50.

2.2 Analysis of porous NiTi scaffolds by micro-computed tomography

2.2.1 Assessing the morphology of selective laser melted NiTi-scaffolds for a three-dimensional quantification of the one-way shape memory effect

The following section deals with the morphology of NiTi scaffolds produced by selective laser melting. Quality factors were determined by micro computed tomography in combination with sophisticated registration software to assess the geometrical deviations of the SLM fabricated scaffolds from the initial scaffold design. The factors derived were applied to quantify the shape memory effect of the scaffold.

Published in Proceedings of SPIE

Assessing the morphology of selective laser melted NiTi-scaffolds for a three-dimensional quantification of the one-way shape memory effect

Therese Bormann*[a,b], Michael de Wild[b], Felix Beckmann[c] and Bert Müller[a]

[a]Biomaterials Science Center, University of Basel, c/o University Hospital, 4031 Basel, Switzerland;
[b]Institute for Medical and Analytical Technologies, University of Applied Sciences and Arts Northwestern Switzerland, 4032 Muttenz, Switzerland;
[c]Institute of Materials Research, Helmholtz-Zentrum Geesthacht, 21502 Geesthacht, Germany.

ABSTRACT

NiTi is promising for the use as bone scaffold, because the pseudoelasticity or the one- and two-way shape memory effect in the physiological window can mechanically stimulate the adherent cells. Such stimuli can enhance osseo-integration and might reduce stress shielding associated with load bearing implants. The present study is based on the additive manufacturing technique of selective laser melting (SLM) to fabricate three-dimensional NiTi scaffolds. We demonstrate that the morphology of the scaffolds can be quantified using synchrotron radiation-based micro computed tomography (SRμCT) and sophisticated registration software. Comparing the CAD file with the SLM scaffolds, quality factors are derived. With respect to the CAD file, the overlap corresponds to (92.5 ± 0.6) %. (7.4 ± 0.42) % of material was missing and (48.9 ± 2.3) % of excess material found. This means that the actual scaffold is less porous than expected, a fact that has to be considered for the scaffold design. In order to quantify the shape memory effect during the shape recovery process, we acquired radiographs rotating an initially deformed scaffold in angular steps of 0.2 degree during controlled heating. The continuously acquired radiographs were combined to tomography data, showing that the quality factors evolved with temperature as the scaffold height, measured by conventional thermo-mechanical analysis. Furthermore, the data comprise the presence of compressive and tensile local strains in the three-dimensional scaffolds to be compared with the physiological situation.

Keywords: NiTi, scaffold, shape memory effect, selective laser melting (SLM), synchrotron radiation, micro-computed tomography, three-dimensional registration

1.   INTRODUCTION

NiTi is a promising candidate for biocompatible load-bearing bone implants as it combines low stiffness with high strength [1, 2]. Near body temperature, it exhibits characteristic properties including pseudoelasticity, the one-way shape memory effect and high damping capacities caused by a reversible crystalline transformation between the austenite and martensite crystalline phase, which are another advantage for osseo-integration of load-bearing implants [2]. The mechanical stimulation of the bony tissues enhances re-modeling and therefore the osseo-inductive behavior [3, 4]. Selective laser melting is a versatile method to prepare porous scaffolds with a variety of regularly arranged unit cells. These open porous structures are generated using computer aided design (CAD). The designs are materialized applying appropriate precursor powders and suitable laser parameters. The selection of powder and laser parameters enables the operator to tailor the structural and thermal properties of the porous constructs [5, 6].

In a porous system including scaffolds or textiles both tensile and compressive strain simultaneously occur even only compression or tensile load is applied (see Fig. 1). Human cells such as osteoblasts might therefore behave in different fashion depending on their location within the scaffold and might migrate toward the preferred location within the unit cell of the scaffold.

Local strains occurring in a porous NiTi scaffold during shape changes induced by heating should be quantified and visualized taking advantage of synchrotron-based micro computed tomography (SRμCT) and sophisticated software tools for rigid and non-rigid registration [7].

*therese.bormann@unibas.ch; phone +41 61 26 59 127, //www.bmc.unibas.ch

These spatially resolved strains could in a next step be directly compared with strains acting on cells in a physiological environment such as the human body. In bones for example, values for strains induced by normal activity lie between 0.005 % and 0.5 % [8, 9]. The application of such micro-strains during in-growth of implants has shown to increase parameters like bone-to-implant contact [10, 11].
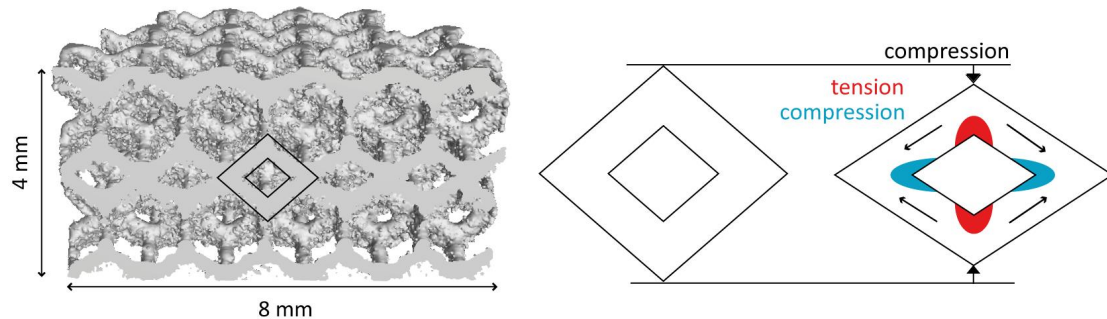

Fig. 1. Three-dimensional rendering of μCT data of a transversally cut NiTi scaffold. The cross section of the unit cells is approximated as diamond shape as indicated. The scheme illustrates the expected local tensile and compressive strains in a unit cell under compression.

We hypothesize that the local strains, which are generated by defined compression of porous NiTi scaffolds prepared by selective laser melting correspond to actual strains occurring in a physiological situation. Cells within the scaffolds should therefore show specific reactions depending on their location and NiTi scaffolds might prove to be clinically relevant for future medical applications.

As a first approach, we are presenting a SRμCT setup to continuously investigate pseudoplastic NiTi scaffolds during their shape recovery process. The method is validated by extracting quantities describing the scaffolds morphology during the heating period and comparing the evolution of these quantities with temperature to conventional thermo-mechanical analysis (TMA) measurements. Furthermore, the scaffolds morphology and deviations from the initial CAD design can be assessed locally and globally by the presented method.

2. MATERIALS AND METHODS

2.1 Scaffold preparation

Selective laser melting (SLM Realizer 100, Realizer, Borchen, Germany) served for the fabrication of scaffolds with sub-millimeter precision from pre-alloyed NiTi powder with a nominal Ni-content of 55.96 wt.-% (Memry GmbH, Weil am Rhein, Germany). The outer dimensions of the scaffolds referred to 8 mm in diameter and 4 mm in height, respectively. The scaffold geometry is defined in a CAD model based on a rhombo-dodecahedral unit cell of $(2 \text{ mm})^3$ with 300 μm thin struts. Subsequent to fabrication, the specimens were subjected to annealing under Ar atmosphere at a temperature of 500 °C for a duration of 25 minutes, which was followed by furnace cooling. The resulting phase transformation temperatures were determined by differential scanning calorimetry (DSC 30, Mettler-Toledo) at a heating rate of 10 K per minute. The austenite start temperature (A_s) corresponded to 25 °C, the austenite peak temperature (A_p) to 35 °C and the austenite finish temperature (A_f) to 41 °C.

For the investigation of the shape recovery process by synchrotron radiation-based micro computed tomography (SRμCT), a scaffold with an original height of 4.01 mm was pseudoplastically deformed by compression along its *z*-axis by 260 μm prior to the SRμCT experiment. To ensure a fully martensitic crystalline structure during deformation, the specimen was cooled down in liquid nitrogen before deformation.

Thermo-mechanical analysis (TMA) of a scaffold, pseudoplastically deformed by compression along its *z*-axis about 265 μm, was done by the TMA 40 (Mettler-Toledo) at a heating rate of 0.083 K per minute in a temperature range from 18 °C to 35 °C.

2.2 Synchrotron radiation-based micro computed tomography setup

SRμCT investigations were carried out on scaffolds prior to deformation, during the shape recovery process induced by controlled heating and subsequent to deformation. The beamline W2 (DESY, Hamburg, Germany) operated by the

Helmholtz-Zentrum Geesthacht served for the tomography data acquisition in the conventional absorption contrast mode [12]. The photon energy was set to 70 keV and projections on a field of 3056*3056 pixels with an effective pixel size of 3.2 μm were recorded in angular steps of 0.2 degrees. Because of the parallel X-rays, the radiographs of the scaffold in original and deformed states were acquired from a 180° rotation. The spatial resolution determined from the modulation transfer function of a highly X-ray absorbing edge [13] corresponded to 7.2 μm.

To investigate the specimen during the one-way shape memory effect, radiographs of the initially deformed scaffold were recorded constantly while the scaffold was subjected to heating. During the heating period 4853 radiographs were obtained, which corresponds to a sample rotation of 970.6 degrees. Heating of the specimen was carried out in a water bath with a rate of 0.067 K per minute, whereas the starting temperature corresponded to 15 °C and the experiment was terminated at a temperature of 37 °C. These thermo-electrically measured temperature values were downwards corrected by about 7.5 K based on a temperature calibration using the TMA measurement of a deformed scaffold from the same processing batch.

2.3 Tomographic reconstruction

Before reconstruction, the recorded radiographs were two-fold binned to improve the photon statistics [14]. The reconstruction was performed by means of the filtered back-projection algorithm [15]. Eleven three-dimensional datasets were reconstructed over the heating period using the 4853 projections in total. The starting angle for each subsequent reconstruction was increased by about 79°. Each of the reconstructed datasets covered a temperature interval of 3 to 5 K. To reduce data size, the datasets were binned after reconstruction for a second time by a factor of two leading to an effective pixel size of 12.93 μm in the datasets used for the 3D registration [16].

2.4 Data treatment

To assess the morphological quality factor of the SLM-fabricated scaffold with regard to the CAD model and to quantify the differences caused by deformation and shape recovery, the tomography datasets were rigidly registered with the CAD design. Rigid registration means, that six independent parameters, three for translation and three for rotation, have to be found.

As the used registration algorithm [17] works on voxel-based three-dimensional data, the CAD data was converted prior to registration, since SLM, as most additive manufacturing methods, is based on a surface triangulated file format (.stl). The CAD file in .stl-format was thus converted into a voxel-based .raw data format using Matlab (2010b, The MathWorks, Natick, USA) code. The voxel size of the dataset was set to $(13\ \mu m)^3$ according to the reconstructed tomography data. The voxel size was further refined to 12.82*12.82*12.99 μm³ to reduce differences between the .stl and .raw-file. All further data processing was done using the Matlab code. For data visualisation, however, we applied VG Studio Max 2.1 (Volume Graphics, Heidelberg, Germany).

2.5 Volume-based segmentation

The reconstructed datasets showed artefacts like blurring and periodic variations in the local absorption values, which were caused by the deformation of the scaffold during the shape recovery. The presence of these artefacts increased the visible strut thickness in the reconstructed data and the background in the histograms of the local X-ray absorption coefficients. The identification of a reasonable threshold for the scaffold segmentation was therefore not straightforward. As the mass of the NiTi scaffolds is known and as we can consider the density and volume to be constant during the measurements, we can reasonably follow a volume-based approach.

As the literature values for the density of NiTi vary between 6.40 and 6.51 g/cm³, we measured the density of the starting material (prior to atomization) by Archimedes principle with a tensiometer (K11, Krüss, Hamburg, Germany), which returned a value of (6.52 ± 0.02) g/cm³. Based on the specimen weight of 0.3 g, the scaffold volume corresponds to (46.0 ± 0.7) mm³. Segmentation between material and background was than accomplished by choosing the threshold such that the volume of the segmented data matched the specimens calculated volume.

3.   RESULTS AND DISCUSSION

3.1 Quality assessment via 3D registration

To assess the overall quality of the SLM fabricated scaffold, the SRμCT dataset of the non-deformed scaffold was rigidly registered with the 3D dataset of the design (CAD model). Figure 2 displays the .stl-file of the CAD model (A),

the SLM-built NiTi scaffold (B) prior to deformation and an overlay of the .stl-file and the scaffold after registration (C, D). From first glance, the lattice shape was matched well by the SLM scaffold. Nevertheless, the main difference of the SLM specimen in comparison to the initial file is protruding material along the struts, as visible from the images in Figure 2 (C) and (D).
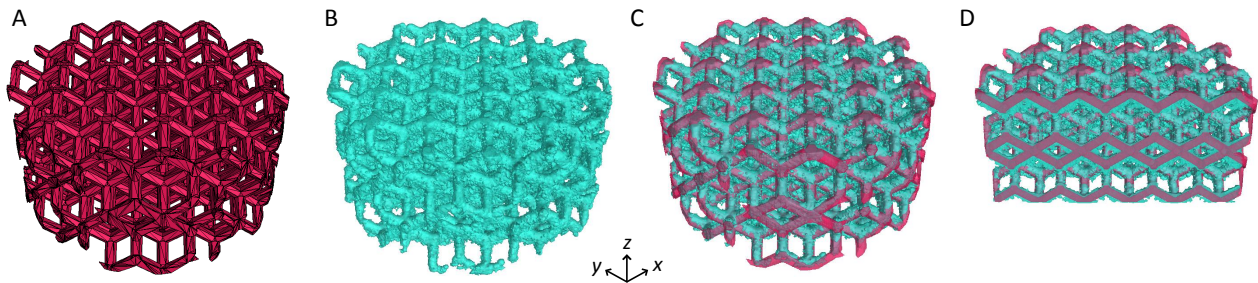

Figure 2. 3D rendering of the CAD .stl-file (A), the SRμCT scan of the non-deformed scaffold (B), overlay of the CAD file and the scaffold after registration (C), and a virtual cut through the latter (D). Diameter of the scaffold refers to 8 mm, height to 4 mm.

To quantify the morphological quality of the SLM built scaffold, we subtracted the registered SRμCT dataset from the CAD file and analyzed the resulting three-dimensional matrix regarding protruding, deficient and overlapping material in reference to the matrix of the initial CAD file [18]. For the whole scaffold, we found that (92.55 ± 0.55) % of the initial matrix overlaps with the SLM scaffold, (48.87 ± 2.30) % is protruding the initial matrix and (7.45 ± 0.42) % of the targeted volume is missing. This means that the actual scaffold is less porous than designed. The intended relative open pore volume corresponded to 84 %, whereas we find in the actual scaffold an open pore volume of about 76 %. With other words, one has to consider this phenomenon in the scaffold design.

To gain closer insight into the material distribution within the scaffold, we analyzed the difference in the registered datasets by the local determination of excess, missing or overlapping material for each slice of voxels along the *x*-, *y*- and *z*-axis, respectively. The results are displayed in Figure 3 for the *z*- and *x*-axis, whereas excess, missing or overlapping material is represented as percentage of the corresponding targeted volume determined from the CAD file. As evident from Figure 3, the overlap of both matrices as well as the deficiency of material is more or less constant along the different axis of the scaffold. Exceptions are the outer boarders of the scaffold where material deficiency usually increases (not represented in Figure 3A) because the tiniest struts at the outside (see Figure 3B, cross sections z2, z3) break away easily during handling of the specimen. The analysis of the protruding material along the scaffolds individual axis on the other hand reveals strong variations, which represent the symmetric lattice shape with a repeating unit of half a unit cell. The scaffold features are repeated twice as much as the original repeating unit of 2 mm, because the rhombic cells are staggered by half unit cell width, as indicated in Figure 3, cross section x2. Each half unit, i. e. 1 mm, the amount of protruding material increases abruptly, independent of the scaffold axis. Nevertheless, the variation of the protruding material along the *z*-direction is higher, covering a range of 25 % to 140 %, than the variation along the *x*- and *y*-axis, which covers a range of 35 % to 120 %.

Reason for the variations in protruding material especially along the *z*-axis is the anisotropic SLM fabrication process. During the additive manufacturing process of SLM, subsequent layers of powder are selectively molten and solidified. Each melting process involves re-heating and re-melting of the already solidified material layers below and heat flux from the topmost layer to the bottom of the scaffold. This, for each layer repeated, process causes additional powder to adhere at the lower surface of struts and knots. Especially the lower surfaces of areas having small inclination angles with respect to the powder layer (*x*-*y*-plane) are susceptible for increased surface roughness [19] due to partly fused powder particles of different size. Also, stalactite formation at down facing faces decreases the surface quality [20]. Nevertheless, we find the highest percentage of protruding material exact in the middle of the knots where the struts merge (cp. Figure 2B, cross section z1, x1, x2). These peaks in protruding material correlate with the slices of the CAD file, which exhibit the lowest absolute volume (cp. Figure 2B, cross section z1). This minimum in absolute volume repeats after 1 mm because the unit cells are staggered by half unit cell width. The peaks of up to 140 % for protruding material are therefore caused by the data representation, which is relative to the targeted volume of the CAD file. Nevertheless, the main geometrical mismatch between CAD file und SLM-fabricated part is excess material at the down-facing surfaces caused by adhering powder particles and stalactite formation.
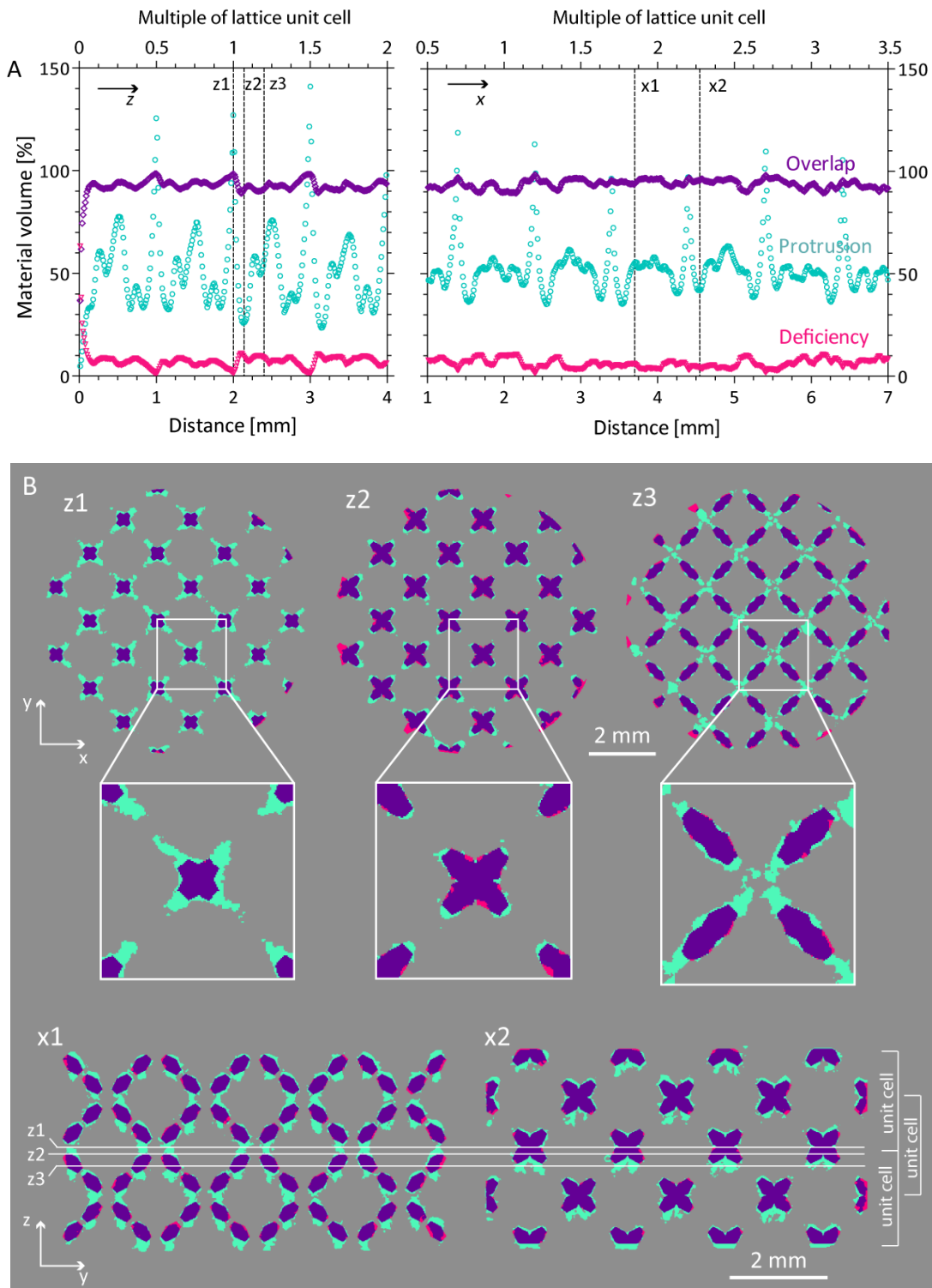
Figure 3. A: Volume of overlapping, protruding and deficient material in percentage of the target volume along the *z*- and the *x*-axis of the scaffold, respectively. B: Virtual cross sections as indicated in the graphs above along the *z*- and *x*-axis of the registered matrix, representing the overlapping (blue), protruding (light blue) and absent (pink) material.

Quality assessment for additive manufactured parts is usually done via investigations of closed porosity and surface roughness [21], both difficult to apply onto filigree and complex-shaped parts with inner structures inaccessible from the outside without specimen destruction. Therefore, the presented method of 3D data registration and analysis is a suitable tool for the quantification of the morphological quality of additive-manufactured scaffolds. Also, the method could be important for the optimization of process parameters, which play a major role for resulting properties in SLM-manufactured parts [5, 22].

3.2 Quantification of the one-way shape memory effect

To quantify the shape recovery of a pseudoplastically deformed SLM-built NiTi scaffold, seven out of the eleven datasets obtained from the continuous SRμCT measurement were registered with the CAD file as described above. The overall quantities for overlapping, protruding and deficient material depend on the temperature, as can be seen from the data summarized in Table 1. The quantities are represented relative to the CAD file, whereas the deviations were estimated to be ±0.6 % for the overlap, ±4.7 % for the protrusion and ±5.7 % for the deficiency.

Table 1. Overall quantities for overlap, protrusion and deficiency relative to the CAD file at different time and temperature points, respectively, before and during the shape recovery process.

	Dataset	Mean temperature	Overlap [%]	Protrusion [%]	Deficiency [%]
0	Prior to deformation	Ambient	92.55 ± 0.55	48.87 ± 2.30	7.45 ± 0.42
1	Deformed scaffold	18.0 °C	77.04 ± 0.46	69.89 ± 3.28	22.96 ± 1.31
2		26.9 °C	79.51 ± 0.48	66.62 ± 3.13	20.49 ± 1.17
3		28.7 °C	82.51 ± 0.49	62.47 ± 2.94	17.49 ± 1.00
4	Shape recovery during heating	30.4 °C	87.70 ± 0.53	57.55 ± 2.70	12.30 ± 0.70
5		32.1 °C	91.08 ± 0.55	53.68 ± 2.52	8.92 ± 0.51
6		32.9 °C	92.30 ± 0.55	51.06 ± 2.40	7.70 ± 0.44
7	Shape recovered	34.0 °C	92.36 ± 0.55	51.68 ± 2.42	7.64 ± 0.43

After completion of the shape recovery, the initial values of dataset #0 are almost entirely recovered. As evident from the data in Table 1, the shape recovery process is accomplished already in dataset #6, referring to a mean temperature of 32.9 °C. Even though each dataset was obtained over a temperature interval covering 3.0 to 4.5 K the evolution of the quantities for overlap, protrusion and deficiency with increasing temperature matches the progression of the scaffold height during temperature increase determined by a conventional TMA measurement, as exemplarily displayed for the quantity of overlapping material with temperature in Figure 4A. The thermoelectrically acquired temperature during the SRμCT measurement was corrected downwards by 7.5 K in accordance with the TMA investigations, which worked on a calibrated temperature sensor.

The temperature interval for the phase transformation from martensite to austenite measured with DSC at 10 K per minute differs from the temperature interval for the shape recovery observed via SRμCT, which has been conducted at a heating rate of 0.067 K per minute. The DSC revealed an A_f value of 41 °C, whereas we observed the fully recovered shape at 32.9 °C in the SRμCT experiment, meaning that the phase transformation is terminated at lower temperatures in the SRμCT investigation. The difference is caused by the distinct heating rates applied in the two experiments. Decreasing the heating rate results in decreased temperatures for the austenitic phase transformation whereas A_s is less heating rate sensitive than A_f [23, 24].

Figure 4B displays the progression of the overlapping material along the scaffolds *z*-axis for the datasets prior and subsequent to deformation as well as after the completed shape memory effect. The data clearly show the almost exact matching of the scaffolds shape prior to deformation and after conducted shape memory effect.
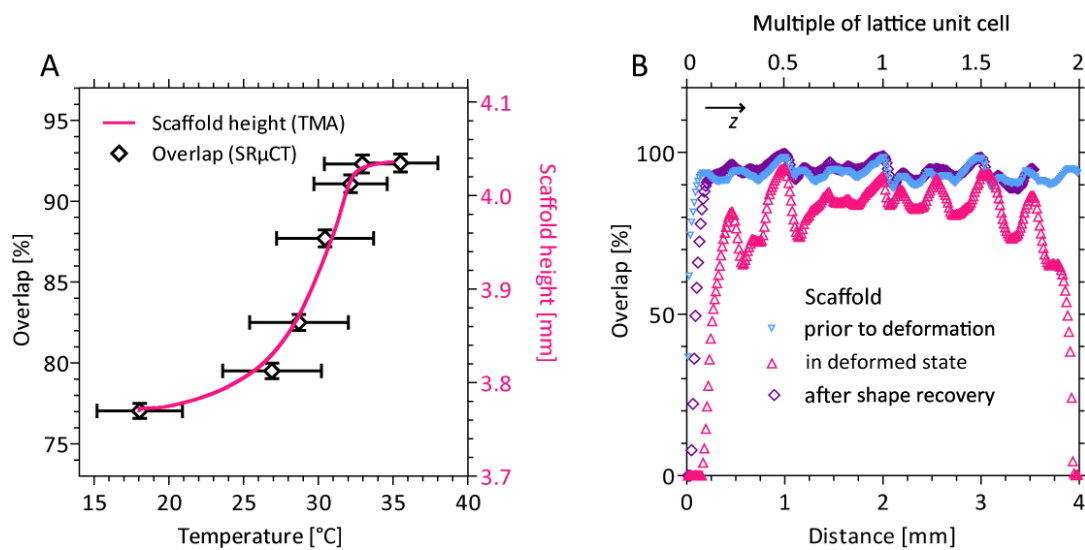
Figure 4A. Overall overlap of the initial file with the seven datasets reconstructed from the SRμCT data obtained during heating of the deformed scaffold and TMA curve of the deformed scaffold. The deviations for the temperature in the SRμCT measurements cover the temperature interval during data acquisition and the assumed measuring inaccuracy. B: Overlap along the *z*-axis for the non-deformed and deformed scaffold as well as the scaffold after completed shape recovery.

4.   CONCLUSIONS

The morphology of parts fabricated by selective laser melting can be assessed and quantified by registration of SRμCT and CAD data. The evaluation of 3D data is in particular expedient for complex-shaped parts, whose porous structure cannot be analyzed without sectioning. Continuously acquired SRμCT data or radiograph recording has proven to be a suitable technique to analyze the temperature-dependent deformation of NiTi scaffolds. Even though the reconstructed datasets initially showed artifacts caused by slight movement of the specimen, we found that progression of the extracted quantities with time and temperature, respectively, agrees well with the progression of the macroscopic parameter scaffold height vs. temperature determined by conventional TMA measurements. The data will serve for the determination of local deformations within scaffolds and the evaluation of cell-response in presence of mechanical stimuli. Based on this approach, scaffold design and loading regime should be refined and optimized with respect to the actual physiological situation.

REFERENCES

[1]   Bansiddhi, A., T.D. Sargeant, S.I. Stupp, and D.C. Dunand, "Porous NiTi for bone implants: a review," Acta Biomater. 4(4), 773-82 (2008).
[2]   Liu, X., S. Wu, K.W.K. Yeung, Y.L. Chan, T. Hu, Z. Xu, X. Liu, J.C.Y. Chung, K.M.C. Cheung, and P.K. Chu, "Relationship between osseointegration and superelastic biomechanics in porous NiTi scaffolds," Biomaterials 32(2), 330-338 (2011).
[3]   Rucci, N., "Molecular biology of bone remodelling," Clinical Cases in Mineral and Bone Metabolism 5(1), 49-56 (2008).
[4]   Hill, P.A. and M. Orth, "Bone remodelling," J. Orthod. 25, 101-107 (1998).
[5]   Bormann, T., R. Schumacher, B. Müller, M. Mertmann, and M. de Wild, "Tailoring selective laser melting process parameters for NiTi implants," J. Mater. Eng. Perform. 21(12), 2519-2524 (2012).
[6]   Bormann, T., R. Schumacher, B. Müller, and M. de Wild, "From powder to complex-shaped NiTi structures by selective laser melting," Euro PM2012 Proceedings 1(Applications and New Processes), 193-197 (2012).

[7]   Schulz, G., H.J.A. Crooijmans, M. Germann, K. Scheffler, M. Müller-Gerbl, and B. Müller, "Three-dimensional strain fields in human brain resulting from formalin fixation," J. Neurosci. Methods 202, 17-27 (2011).

[8]   Frost, M., "A 2003 update of bone physiology and Wolff's law for clinicians," Angle Orthod. 74(1), 3-13 (2004).

[9]   Yang, P.F., G.P. Brüggemann, and J. Rittweger, "What do we currently know from in vivo bone strain measurements in humans?," J. Musculoskelet. Neuronal Interact. 11(1), 8-20 (2011).

[10]   Vandamme, K., I. Naert, J.V. Sloten, R. Puers, and J. Duyck, "Effect of implant surface roughness and loading on peri-implant bone formation," J. Periodont. 79(1), 150-157 (2008).

[11]   Zhang, X., K. Vandamme, A. Torcasio, T. Ogawa, G.H. van Lenthe, I. Naert, and J. Duyck, "In vivo assessment of the effect of controlled high- and low-frequency mechanical loading on peri-implant bone healing," J. R. Soc. Interface 9(72), 1697-1704 (2012).

[12]   Beckmann, F., J. Herzen, A. Haibel, B. Müller, and A. Schreyer, "High density resolution in synchrotron-radiation-based attenuation-contrast microtomography," Proc. of SPIE 7078, 70781D (2008).

[13]   Müller, B., P. Thurner, F. Beckmann, T. Weitkamp, C. Rau, R. Bernhardt, E. Karamuk, L. Eckert, S. Buchloh, E. Wintermantel, D. Scharnweber, and H. Worch "Three-dimensional evaluation of biocompatible materials by microtomography using synchrotron radiation," Proc. of SPIE 4503, 178-188 (2002).

[14]   Thurner, P.J., F. Beckmann, and B. Müller, "An optimization procedure for spatial and density resolution in hard X-ray micro-computed tomography," Nucl. Instrum. Methods Phys. Res. Sect. B-Beam Interact. Mater. Atoms 225, 99–603 (2004).

[15]   Kak, A.C. and M. Slaney, *Principles of Computerized Tomographic Imaging*. 1988: IEEE Press.

[16]   Müller, B., H. Deyhle, S. Lang, G. Schulz, T. Bormann, F. Fierz, and S. Hieber, "Three-dimensional registration of tomography data for quantification in biomaterials science," Int. J. Mater. Res. 103(2), 242-249 (2012).

[17]   Andronache, A., M. von Siebenthal, G. Szekely, and P. Cattin, "Non-rigid registration of multi-modal images using both mutual information and cross-correlation," Med. Image Anal. 12, 3-15 (2008).

[18]   Fierz, F.C., F. Beckmann, M. Huser, S.H. Irsen, B. Leukers, F. Witte, O. Degistirici, A. Andronache, M. Thie, and B. Muller, "The morphology of anisotropic 3D-printed hydroxyapatite scaffolds," Biomaterials 29(28), 3799-806 (2008).

[19]   Strano, G., L. Hao, R.M. Everson, and K.E. Evans, "Surface roughness analysis in selective laser melting", in: Innovative Developments in Design and Manufacturing: Advanced Research in Virtual and Rapid Prototyping. 2012, CRC Press-Taylor & Francis Group: Boca Rano. p. 561-565.

[20]   Vandenbroucke, B. and J.-P. Kruth, "Selective laser melting of biocompatible metals for rapid manufacturing of medical parts," Rapid Prototyping J. 13(4), 196-203 (2007).

[21]   Bremen, S., W. Meiners, and A. Diatlov, "Selective laser melting: a manufacturing technology for the future?," Laser Technik Journal 2, 33-38 (2012).

[22]   Kempen, K., E. Yasa, L. Thijs, J.-P. Kruth, and J. van Humbeeck, "Microstructure and mechanical properties of selective laser melted 18Ni-300 steel," Physics Procedia 12, 255-263 (2011).

[23]   Nurveren, K., A. Akdogan, and W.M. Huang, "Evolution of transformation characteristics with heating/cooling rate in NiTi shape memory alloys," J. Mater. Process. Technol. 196, 129–134 (2008).

[24]   Wang, Z.G., X.T. Zu, and Y. Huo, "Effect of heating/cooling rate on the transformation temperatures in TiNiCu shape memory alloy," Thermochim. Acta 436, 153–155 (2005).

2.2.2 Combining micro computed tomography and three-dimensional registration to evaluate local strains in shape memory scaffolds

To study the local deformation behavior of porous NiTi scaffolds, variable temperature micro computed tomography in combination with three-dimensional data registration was applied. The local strain and displacement fields in a pseudoplastic scaffold subjected to deformation and heating were determined. Uniaxial scaffold compression resulted in local strains up to a factor of 2.5 higher than the integral deformation. In addition, the local development of the shape recovery process could be visualized.

Published in Acta Biomaterialia

CrossMark

Combining micro computed tomography and three-dimensional registration to evaluate local strains in shape memory scaffolds

Therese Bormann [a,b], Georg Schulz [a], Hans Deyhle [a], Felix Beckmann [c], Michael de Wild [b], Jürg Küffer [d], Christoph Münch [d], Waldemar Hoffmann [b], Bert Müller [a,*]

[a] Biomaterials Science Center, University of Basel, c/o University Hospital Basel, 4031 Basel, Switzerland
[b] Institute for Medical and Analytical Technologies, School of Life Sciences, University of Applied Sciences and Arts Northwestern Switzerland, 4032 Muttenz, Switzerland
[c] Institute of Materials Research, Helmholtz-Zentrum Geesthacht, 21502 Geesthacht, Germany
[d] Institute of Product and Production Engineering, School of Engineering, University of Applied Sciences and Arts Northwestern Switzerland, 5210 Windisch, Switzerland

ARTICLE INFO

ABSTRACT

Appropriate mechanical stimulation of bony tissue enhances osseointegration of load-bearing implants. Uniaxial compression of porous implants locally results in tensile and compressive strains. Their experimental determination is the objective of this study. Selective laser melting is applied to produce open-porous NiTi scaffolds of cubic units. To measure displacement and strain fields within the compressed scaffold, the authors took advantage of synchrotron radiation-based micro computed tomography during temperature increase and non-rigid three-dimensional data registration. Uniaxial scaffold compression of 6% led to local compressive and tensile strains of up to 15%. The experiments validate modeling by means of the finite element method. Increasing the temperature during the tomography experiment from 15 to 37 °C at a rate of $4 \, \mathrm{K \, h^{-1}}$, one can locally identify the phase transition from martensite to austenite. It starts at ~24 °C on the scaffolds bottom, proceeds up towards the top and terminates at ~34 °C on the periphery of the scaffold. The results allow not only design optimization of the scaffold architecture, but also estimation of maximal displacements before cracks are initiated and of optimized mechanical stimuli around porous metallic load-bearing implants within the physiological temperature range.

1. Introduction

Suitable mechanical stimuli govern tissue formation [1]. The presence of a dynamic mechanical stimulus alters, among other things, mesenchymal stem cell proliferation and differentiation and, hence, regulates bone formation [2–5]. Therefore, the appropriate cyclic mechanical loading of solid and porous implants gives rise to enhanced osseointegration [6–8]. The uniaxial compressive deformation of scaffolds, for example, leads to osteogenic effects in osteoblasts [9] and increases cell differentiation and extracellular matrix synthesis [10]. To achieve an increase in bone formation within scaffolds upon mechanical stimulation, strains between 0.5 and 1.5% are usually proposed [2,11–13].

Scaffolds for load-bearing applications usually consist of metals such as stainless steel, titanium and its alloys, tantalum or NiTi, because of the required mechanical strength [14]. NiTi belongs to well-established biomaterials with distinct mechanical properties, including comparatively low elastic modulus, high damping capacity, pseudoelasticity and the possibility for shape recovery after

deformation. It was hypothesized that pseudoelasticity should allow for cyclic mechanical stimulation of tissue in the proximity of a NiTi scaffold or implant, as an induced deformation can be recovered upon unloading [15]. Also, the shape memory effect might allow for mechanical cell stimulation, as a scaffold-shape change can be thermally induced [16]. Moreover, porous NiTi shows high osteoconductivity and supports osseointegration, which is achieved faster and with better bonding than for porous Ti [17,18]. The reasons behind this phenomenon might be the pseudoelasticity and the low elastic modulus of NiTi, as they mimic the mechanical properties of healthy bone better than other metallic alloys [17].

Several techniques for manufacturing porous NiTi scaffolds are on the market: space holder methods [19,20] including metal injection molding [21,22] or self-propagating high-temperature synthesis [23–25]. These techniques, however, only entail rounded/sponge-like pore geometries. Additive manufacturing techniques such as selective laser melting (SLM) are more flexible, as a focused laser beam fuses the metal powder according to the pre-defined design in micrometer-thin layers. In this way, one can produce complex-shaped NiTi scaffolds with micrometer-sized pores based on three-dimensional (3-D) units [16,26]. It was

---

* Corresponding author. Tel.: +41 61 2659660; fax: +41 61 2659699.
  E-mail address: bert.mueller@unibas.ch (B. Müller).

recently demonstrated that SLM-built porous NiTi scaffolds are suitable carriers for mesenchymal stem cells [27]. Furthermore, arranging the units in a periodic manner offers an easy way to tailor properties via unit cell adjustments such as varying strut thickness, unit dimensions or design. One can tune, for example, the mechanical properties and cell seeding efficacy of scaffolds [28,29]. The porous architecture of such scaffolds divides compressive load applied to the entire component into local compressive and tensile strains covering a broad range of amplitudes. The evaluation of the local strains is therefore essential for understanding cell–implant interactions and improving the scaffold architecture for tissue engineering in vitro and tissue integration in vivo.

The objective of the study is to measure the 3-D displacements and strain fields occurring upon scaffold compression in porous NiTi scaffolds via synchrotron radiation-based micro computed tomography (SRμCT) and non-rigid 3-D registration. A pseudoplastic scaffold at room temperature was selected for the investigations, in order to determine the displacement fields during shape recovery. To this end, an in situ SRμCT setup was used, enabling controlled heating for a continuous and well-defined shape recovery process of the deformed NiTi scaffold.

2. Materials and methods

2.1. Specimen preparation

Selective laser melting (SLM) (SLM Realizer 100, SLM-Solutions, Lübeck, Germany) served for the fabrication of cylindrical NiTi scaffolds of height 4 mm and diameter 8 mm (cf., Fig. 1). The cubic unit cell of the scaffolds with a volume of $(2 \text{ mm})^3$ was based on a rhombic dodecahedron. As the cylindrical scaffolds were built from cubic units, the cells at the fringe of the cylinder were truncated. Two layers of six complete and nine truncated unit cells were stacked upon each other, i.e. the bottom layer reached from 0 to

2 mm of the scaffold height, the top layer from 2 to 4 mm. An integrated layer of seven complete and ten truncated unit cells, staggered about a half unit cell compared with the bottom and top layer cells, was formed in the center of the scaffold. This center layer ranged from 1 to 3 mm of the scaffold height. The struts of the architectural elements were 300 μm thick. The pre-alloyed NiTi powder (MEMRY GmbH, Weil am Rhein, Germany) with a nominal Ni-content of 55.96 wt.% consisted of spherical particles 35–75 μm in diameter. After SLM processing, the specimens exhibited phase transformation temperatures of (10 ± 9) °C for martensite start M_s, (-87 ± 6) °C for martensite finish M_f, (-44 ± 7) °C for austenite start A_s and (3 ± 3) °C for austenite finish A_f. The broad temperature difference between martensite start and finish might be an indication that there is also an R-phase transformation included. Ni evaporation during SLM processing was calculated taking the well-known relationship between the austenite finish temperature and the Ni content as well as the impurity content of the scaffolds into account [30,31]. The preferential evaporation of Ni with respect to Ti amounted to a concentration shift of ∼1 wt.% with respect to the starting material prior to atomization.

In order to obtain specimens with pseudoplastic behavior around body temperature, scaffolds were post-treated by annealing to a temperature of 500 °C for a duration of 60 min under an Ar atmosphere, followed by cooling to room temperature within 140 min. Even though exact adjustment of transformation temperatures requires further optimization of thermal treatment conditions, applied parameters were found to shift the phase transformation temperatures to the desired range. The resulting phase transformation temperatures of the scaffold investigated referred to 45 °C for R-phase start R_s, 14 °C for R-phase finish R_f, −18 °C for M_s and −39 °C for M_f upon cooling and to 25 °C for A_s and 41 °C for A_f upon heating. The phase transformation temperatures were determined by means of differential scanning calorimetry (DSC; DSC 30, Mettler-Toledo) using a heating rate of 10 K min⁻¹.
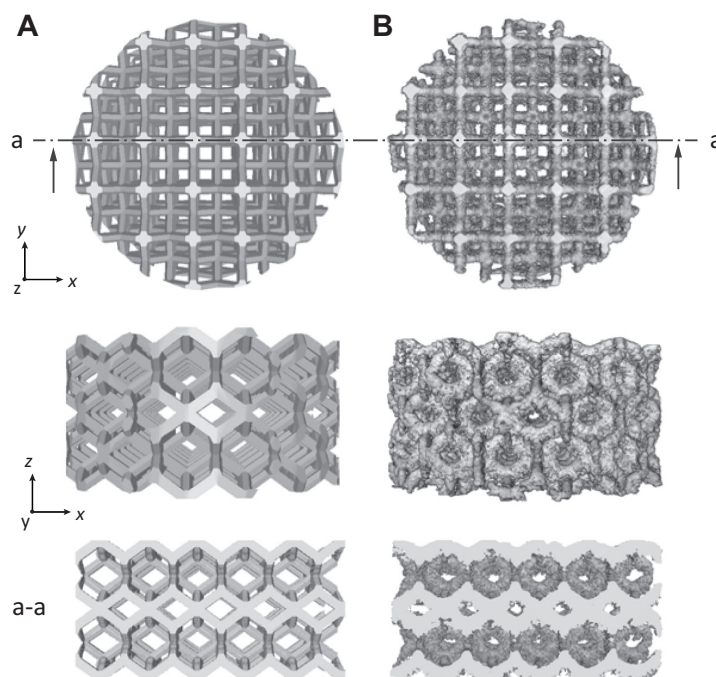
Fig. 1. Three-dimensional views of the scaffold (8 mm in diameter, 4 mm in height): column A, CAD-file used for scaffold fabrication; column B, 3-D rendering of tomography data of the SLM-built NiTi scaffold. The cross section indicated in the top view is applied for the representation of the global and local displacement fields (cf., Fig. 3).

To analyze the scaffold in deformed state and during shape recovery, the cylindrically shaped scaffold was pseudoplastically compressed between two coplanar plates by (0.40 ± 0.01) mm, leading to a pseudoplastic height reduction of (0.24 ± 0.01) mm, which corresponds to 6% of the scaffold height. In other words, upon unloading, the scaffold elastically or pseudoelastically already recovered (0.16 ± 0.02) mm of the induced deformation. In order to ensure a martensitic crystalline structure during deformation, the scaffold was immersed in liquid nitrogen prior to deformation. No difference in the final scaffold height at room temperature (20 °C) upon compression and unloading was observed for scaffold deformation directly in liquid nitrogen as well as for scaffold deformation at room temperature past immersion in liquid nitrogen.

For the SRμCT measurements, the specimen was glued to a round steel sample holder 4 mm in diameter subsequent to specimen deformation. The holder was centrally placed on the scaffolds top layer, as it supported the scaffold from above. For mounting, two-component epoxy resin was used (UHU plus schnellfest; UHU GmbH, Bühl/Baden, Germany). The resin was allowed to cure for ∼20 min prior to the start of the experiment.

2.2. Finite element method

The finite element method (FEM) was applied to simulate axial compression of the cylindrical scaffold using the ADINA 8.9 finite element analysis program (ADINA R&D, Watertown, USA). The finite element model itself was constructed by re-meshing the triangular facets and further manual meshing based on the .stl-file for SLM fabrication using the FEMAP 10 finite element pre-processor (Siemens PLM Software, Köln, Germany). The mesh was formed by 447,028 ten-node tetrahedral elements with a mean edge size of 74 μm. The superelastic and shape memory effects of NiTi were included with a shape memory alloy material model described by Roh and Bae [32], implemented in ADINA. The shape memory alloy material model required the specification of the elastic modulus, the slope of transformation and the thermal expansion coefficients for the martensite and austenite phases. The elastic moduli and slopes of transformation were reasonably assumed on the basis of static compression testing of SLM-fabricated NiTi cylinders. The derived values that were applied to the material model corresponded to 16 and 40 GPa for the elastic moduli and to 4.7 and 6.0×10^6 Pa K^{-1} for the slopes of transformation for martensite and austenite, respectively. The maximal transformation residual strain was set to 0.05. The phase transformation temperatures were chosen in agreement with the DSC measurements as $A_s = 25$ °C, $A_f = 41$ °C, $M_s = -18$ °C and $M_f = -39$ °C. Further parameters applied were taken from the literature, namely a Poisson's ratio of 0.34 for both crystalline states and coefficients of thermal expansion of 11×10^{-6} K^{-1} and 6.6×10^{-6} K^{-1} for austenite and martensite, respectively [32,33]. The temperature for the simulation corresponded to 20 °C, considering the scaffold in its martensitic phase. All nodes at the scaffold's bottom were fixed in the axial direction, including two nodes with lateral fixations to guarantee statically defined boundary conditions. To simulate the scaffold deformation, all nodes on the topside were axially displaced by 0.24 mm, in agreement with the experimental data.

2.3. SRμCT

SRμCT served for the investigation of a pseudoplastically deformed scaffold before, during and subsequent to controlled heating. The experiments were carried out at the W2 beamline operated by the Helmholtz-Zentrum Geesthacht at the DORIS III storage ring of the Deutsches Elektronen-Synchrotron DESY (Hamburg, Germany) [34]. The beamline was equipped with a

temperature-controlled water bath for in situ measurements. A photon energy of 70 keV was used for recording radiographs with an effective pixel size of 3.2 μm on a 3056 × 3056 pixel detector in angular steps of 0.2°. The spatial resolution of the projections was determined from the 10% value of the modulation transfer function of a highly X-ray absorbing edge [35] and corresponded to 7.2 μm. To investigate the NiTi scaffold during the shape recovery process, the initially deformed specimen was heated from 15 to 37 °C at a rate of 4 K h^{-1}. During heating of the specimen, 4853 radiographs were continuously recorded. A more detailed description of the SRμCT experiment was published earlier [16]. The thermoelectrically measured temperature values were corrected by ∼7.5 K according to a temperature-calibrated thermo-mechanical analysis measurement (TMA 40, Mettler-Toledo) [16].

2.4. Three-dimensional data sets

Six 3-D data sets were reconstructed by the standard filtered back-projection algorithm [36] selecting a sequence of 900 from the 4853 radiographs acquired during the heating period. The temperature intervals related to the six selected tomograms are indicated in Fig. 2. The intervals differ slightly, because the exposure time during radiograph acquisition was adjusted to achieve comparable photon statistics. The integral scaffold-height change was measured by conventional thermo-mechanical analysis using a scaffold pseudoplastically deformed by 0.265 mm, i.e. 6.5% global strain.

Tomogram #0 refers to the scaffold in its pseudoplastically deformed state. Tomogram #5 shows the scaffold after complete shape recovery, which equals to the initial, non-deformed scaffold shape, as previously shown [16]. Data sets 1–4 exhibit the scaffold in the course of the shape recovery process. As the shape recovery involves scaffold deformation during data acquisition, artifacts including blurring occur and are visible in the reconstructed data. The segmentation of the scaffolds was therefore carried out considering the conservation of NiTi volume of (46.0 ± 0.7) mm^3 within the scaffold during the SRμCT experiment, as described in more detail elsewhere [16]. The radiographs were twofold binned prior to reconstruction to improve the contrast [37]. The reconstructed data were twofold binned again to decrease the data size for easier handling. The pixel length in the analyzed 3-D data therefore corresponds to 12.93 μm.

2.5. Three-dimensional data registration

In order to quantify the local displacements within the scaffold caused either by compression or by the shape memory effect, the
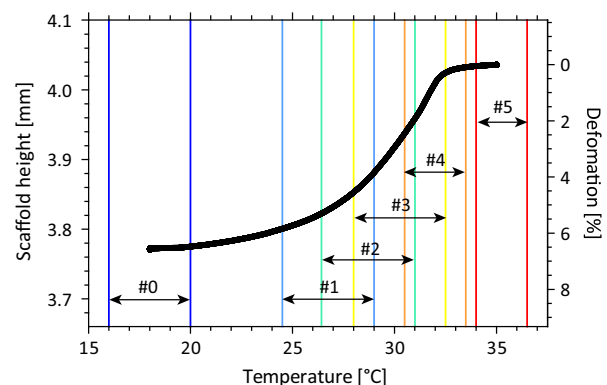

Fig. 2. Evolution of the scaffold height and relative deformation, respectively, with increasing temperature. The temperature ranges for reconstruction of the six data sets are indicated.

data sets were registered, taking advantage of a non-rigid registration approach [38,39], also termed digital volume correlation [40]. To register two data sets, one has to select the reference and the floating data set. The floating tomogram is transformed and resampled to match the reference as close as possible, and the displacement of each individual voxel is recorded [38]. As the floating data set is (virtually) transformed and the reference data set defines the shape to be matched, the floating data was chosen such that the virtual deformation matched the direction of scaffold deformation or shape recovery, respectively. This means that, for analyzing scaffold compression, the final data set of the completely recovered scaffold (#5) was set as floating, and the initial, deformed data set (#0) as reference. In contrast, to analyze the shape recovery process, the recovered state served as reference, and the deformed state as floating.

A prerequisite for extracting the local deformations is the rigid registration of the data to determine the precise location (three translational parameters) and orientation (three rotational parameters) in the 3-D space. As an intermediate level of analysis, the affine registration was applied, which additionally includes three global scaling parameters in three orthogonal directions. The local deformations are finally obtained from a non-rigid registration algorithm, which is based on the adaptive hierarchical subdivision of the 3-D data sets, where the non-rigid matching problem is decomposed into numerous local affine registrations of sub-data sets of decreasing size [41,42].

2.6. Determination of displacement and strain fields

The global and local voxel displacement fields in the scaffold subjected to deformation or heating were calculated from an affine and a non-rigid registration step. The global displacement field contains the displacements caused by scaling of the data (affine registration) as well as the local displacements from the non-rigid registration. The local displacement field contains the displacements aside from scaling.

In order to discriminate between tensile and compressive deformation within the scaffold subjected to compression, the local strain fields were determined from the local voxel displacement fields. The relative values for elongation or compression of each cubic voxel along its three orthogonal directions x, y and z were calculated using an approach suggested by Schulz et al. [41]. The scaffold was oriented such that z coincided with the cylinder axis, and x and y coincided with the rhombic faces of the dodecahedron (cf., Fig. 1). A detailed description of the geometry of the rhombic dodecahedron can be found in the literature [43].

3. Results

3.1. FEM simulation of scaffold compression

In order to get an idea of the locations and the magnitudes of local strains caused by scaffold compression, the present authors simulated a deformation of 0.24 mm, i.e. 6% global strain, on the computer-generated file of the scaffold design with the FEM. The strains were visualized according to the simulation along the three orthogonal axes of the scaffold. Fig. 3 displays the strains along the x, y and z directions. For reasons of symmetry, strains along the x and y directions were consolidated. Tensile strains are represented in yellow and red, compressive strains are represented in blue. It is evident that tension and compression were present simultaneously. The maximal strain values occurred in the rhombs oriented parallel to the z axis. Thus, cross sections through these rhombs were chosen for visualizing the strains and displacements within the 3-D scaffold. The tensile strains reached maximum val-

ues in the x and y directions of up to ~6.5% and were located at the obtuse angles inside the rhombs. In the z direction, tensile strain maxima of up to ~4.5% occurred in the areas connecting abreast the rhombs. The magnitudes of the compressive strain maxima were generally smaller than those of the tensile maxima. Compressive strains of up to ~4% were found along z at the acute angles inside the rhombs. Along x and y, compressive strain maxima reaching up to ~4% were found at the obtuse angles at the outside of the rhombs and compressive strains of up to ~2.5% occurred in the knots connecting the rhombs.

The simulation showed a symmetric deformation of the upper and the lower scaffold half, which is not surprising, because the scaffold is symmetric along its z axis. Regarding the individual unit cells, a symmetrical deformation was found along all three orthogonal scaffold axes, as long as the units were complete. The deformation behavior in the outer, truncated unit cells differed from the deformation behavior of the inner units surrounded by adjacent cells due to the discontinuity of the structure. In the truncated cells, the tensile strain maxima occurring in the obtuse angles of the rhombs cannot be observed. Furthermore, the compressive strain at the outside of the rhombs was less homogeneously distributed than in the complete units.

### 3.2. Global displacement fields

In order to validate the results of the FEM simulations, the global and local displacement fields were derived, as well as the local strain field of the materialized scaffold upon compression of 0.24 mm by SRμCT measurements and 3-D data registration. Fig. 4A shows a cross section of the global displacement field of the SLM-produced NiTi scaffold, comparing the starting, compressed state with that after the temperature-induced phase transformation. It was calculated from the 3-D registration of data set #0 (deformed scaffold) and data set #5 (completely recovered scaffold). The magnitude of the voxel displacement is color coded. The direction of the displacement in the image plane is indicated using arrowheads. The minimal voxel displacements were located on top, where the scaffold was connected to the sample holder. The maximal voxel displacements occurred at the bottom. They corresponded to 0.26 mm, which approximates well the integral scaffold deformation of 0.24 mm.

The global displacement field contains the scaling-related displacements from the affine registration and the local displacements from the subsequently performed non-rigid registration. The scaling factors of the affine registration along x, y and z corresponded to 1.025, 1.022 and 0.941, respectively. This means that the scaffold was actually compressed ~5.9% along z, and expanded along x and y by 2.5 and 2.2%, respectively.

As the displacements from the scaling were about a factor of five higher than the local ones, the global displacement field reflects mainly the scaffolds height reduction and the linked increase in its perimeter caused by compression.

3.3. Local displacement fields

In order to resolve the distortions taking place aside from the scaling-related displacements, the local displacement field was calculated from the registration of data set #0 (deformed scaffold) and data set #5 (completely recovered scaffold). Fig. 4B displays a cross section of the local displacement field of the scaffold in which, again, the magnitude of the local voxel displacement is color coded, and the direction of the local voxel displacement in the image plane is indicated by arrowheads. The average local voxel displacement amounted to ~20 μm. The maximum local displacements corresponding to ~80 μm occurred in the struts of the truncated unit cells at the periphery of the scaffold. These outer unit
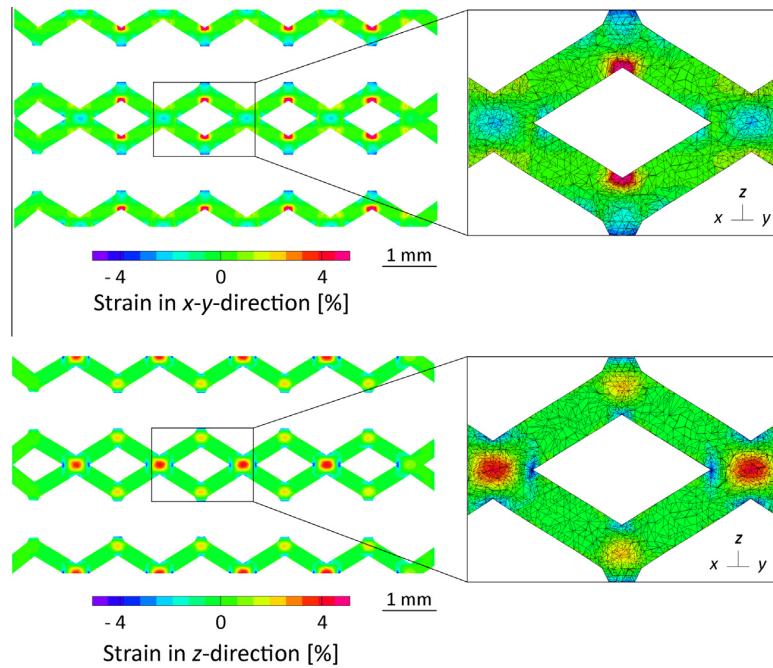
Fig. 3. Results of the FEM simulation of axial compression along the scaffold's z axis of 0.24 mm. The strains along z and along x–y are displayed separately. Strain values below zero correspond to compressive, strain values above zero to tensile strain. Along x–y, tensile strain maxima occur at the obtuse angles of the rhombic openings, compressive strains occur in the region between the individual rhombs. Along z, compressive strain maxima occur at the acute angles of the rhombic openings and tensile strain maxima occur in the region between the individual rhombs.
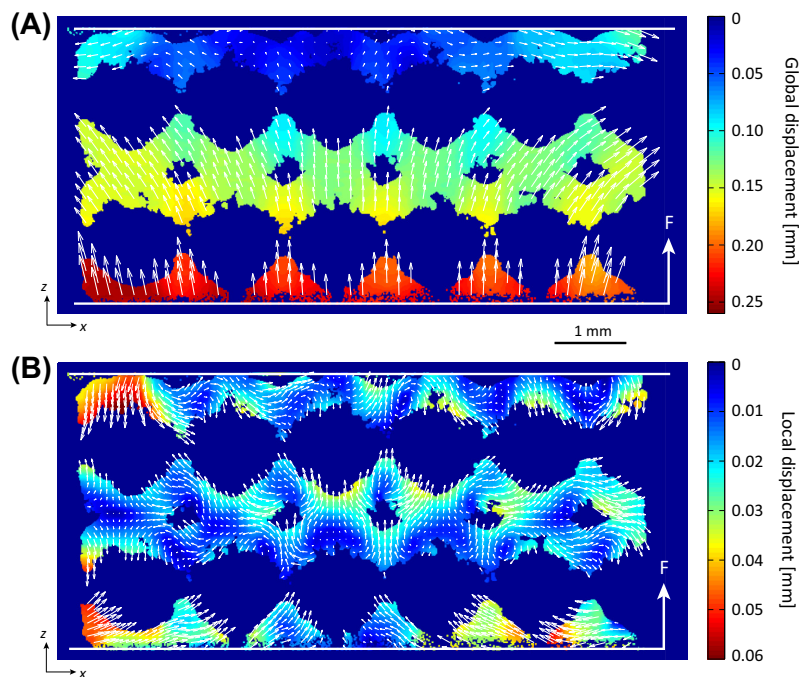
Fig. 4. Displacement fields of the SLM-produced scaffold subjected to deformation. The direction of the integral deformation is indicated by the arrow in the bottom right corner. The amplitude of the related voxel displacement is color coded. Arrowheads mark the corresponding direction of the displacement in the image plane. The length of the arrows is relative to the magnitude of the voxel displacement. The global displacement field (A) displays the overall voxel displacement owing to scaffold compression, i.e. it contains the voxel displacements from affine and non-rigid registration. It reveals the height reduction of the scaffold and the related perimeter increase. Voxel displacements were largest at the bottom, as the scaffold was connected on top of the sample holder. The local displacement field (B) pictures the distortions within the scaffold, ignoring any scaling-related displacements. The highest deformations occurred in the outer, truncated unit cells of the scaffolds. Within the individual unit cells, the highest local displacements were found in the upper part of the rhombic areas.

cells were deformed deviant from the inner unit cells, because the struts were open-ended and possessed higher degrees of freedom. The directions of the local voxel displacements indicate already distinct regions with compressive or tensile deformation, as the arrowheads point towards (compression) or away (tension) from each other, respectively.

Although it was intended to build NiTi scaffolds with identical units, deviations existed as a result of the production process. This can be seen in Fig. 5A, which depicts a single unit cell from the SLM-built scaffold, showing an irregular and rough surface with partly fused powder particles, especially underneath the struts. As a consequence, the local displacements differed slightly from cell to cell. To determine the mean local displacements within one unit cell, the mean local displacement field from six unit cells was calculated, as elucidated in Fig. 5B. These complete cells were in the center of the scaffold and surrounded by adjacent cells on each of their six faces. The mean value was determined by summing the voxel values of corresponding locations and normalizing the sum with respect to the number of voxels containing material. Owing to the irregular surface, the struts in the averaged unit cell are thickened.

Fig. 5C depicts two cross sections of the mean local displacements of the unit cell, which cut the rhombs and the central pillar of the unit cell parallel to z, as indicated in Fig. 5A. Maximum mean local displacements of up to ~35 μm were found inside the rhombic dodecahedron, as demonstrated in Fig. 5C on the right. The mean local displacements within the unit cell were mirror symmetric with respect to the z axis. In the x–y plane, asymmetries were present (cf., Fig. 5C). This means that, in the SLM-built scaffold, the upper and lower halves of the unit cell were deformed differently, despite the symmetry plane. However, the average local strains and their standard deviations in the upper and the lower half of the unit cell corresponded to $(14.4 \pm 6.8)\,\mu m$ and $(12.9 \pm 6.4)\,\mu m$, respectively, showing that the average local displacements amounted to approximately the same value for the two halves.

3.4. Local strain field

In order to identify actual strain values and to discriminate further between tensile and compressive deformation within the scaffold, the local strain field was derived from the local displacement field. Because the local strains exhibited differences between the individual unit cells, the mean strain field was determined for one unit cell in the same manner as for the mean local displacement field. Fig. 5D illustrates two virtual cross sections of the mean plane strains along the three orthogonal directions of the averaged cell. Compressive strain (blue color) equals values below zero. Tensile strain (yellow to red) corresponds to values above zero. Macroscopically, the scaffold was compressed by 6% in the z direction. In the strain field derived from 3-D data registration, values of up to ~15% were found for compression and tension. The compressive strain maxima occurred along the z direction and were localized around the opening in the rhomb parallel to z (Fig. 5D, bottom) as well as at the obtuse angles on the outside of the rhombs. The tensile strain maxima occurred along the x and y directions and resided mainly above the opening in the rhomb, as depicted in Fig. 5D. Tensile strains along z of up to ~3.5% were found in the regions connecting the rhombs. The same regions exhibited compressive strains along x and y, which ranged up to 3%. The bows above and underneath the center of the unit cell (Fig. 5D, cross sections b–b and d–d) show strain values in the range between 1 and 5% compressive and tensile strain. The striped appearance of the strain field is an artifact from the subdivision of the 3-D data during the non-rigid registration. For the compression range examined, the tensile and compressive strains of up to 15% are relatively large compared with the strain values usually suggested as mechanical stimulus for intramembranous bone formation, which lie in the range 0.5–1% [2,11–13]. Following the endochondral ossification route, however, mechanical stimuli in the strain range of 15% are favorable [44].

Tensile deformation was clearly dominant in the x and y directions, as ~84% of the voxels exhibited tensile strain along x and 87% of the voxels exhibited tensile strain along y. Along z, compressive deformation was dominant, with 92% of the voxels exhibiting compressive strain.

The general formation of regions with high strains along x and y were considered to be symmetric for the upper and lower halves of the unit cell. Nevertheless, the area for the occurrence of tensile strain maxima was clearly expanded in the upper half of the unit cell relative to the lower half. In addition, these strain maxima did not necessarily correspond to the areas of high local displacements as, above the openings, only smaller local displacements in the range 20–50 μm occurred. The strains along z were symmetric regarding all three orthogonal axes.

### 3.5. Local displacement fields during shape recovery

To temporally and spatially resolve the shape recovery, the local displacement fields were determined for five intervals during heating of the pseudoplastically deformed scaffold. Each interval covered a part of the temperature ramp, at which, for each case, two subsequent data sets were non-rigidly registered. Table 1 contains the registered data sets, the corresponding temperature regimes and the average local displacements σ for the whole scaffold as well as for the bottom, the center and the top layers of unit cells (compare Section 2.1). Fig. 6 shows projections of the local displacement fields for each of the five data sets in the x–z plane, which means that the local displacements presented were integrated along the y axis and normalized with respect to the number of voxels containing material. The scaffold was supported from above, as it was mounted on top of a cylindrical sample holder with a diameter of 4 mm. The top layer of the scaffold one may therefore also term the 'fixed layer', while the bottom layer of the scaffold may be termed the 'free to move layer'. As depicted in Fig. 6, the shape recovery process took place heterogeneously within the scaffold: In step 1, local displacements were hardly observed, with the exception of outmost struts that show slight displacements. In step 2, the local displacements became more pronounced, whereas a gradient could be observed with highest displacement values at the bottom and smallest displacement values at the inner, top part of the scaffold. Step 3 again shows a gradient in the displacements, whereas the highest displacements were still observed in the bottom region of the scaffold as well as in the outer, truncated unit cells. Comparing step 2 and step 3, increased displacement values were apparent in step 3. In step 4 and step 5, the scaffold showed a relatively homogeneous distribution of local displacements, whereas step 4 showed maxima in the truncated unit cells at the outer scaffold region. As the local displacements are caused by micro-motions of the scaffold struts, which in turn arise from the martensite to austenite phase transformation, the local displacements during the shape recovery process indicate a temporal and local variation in the phase transformation in the scaffold during the heating period.

4. Discussion

The present study confirms that the local deformation of porous scaffolds can be measured by SRμCT combined with 3-D data analysis using non-rigid registration (in the following termed '3-D registration'). SRμCT in combination with 3-D registration is well
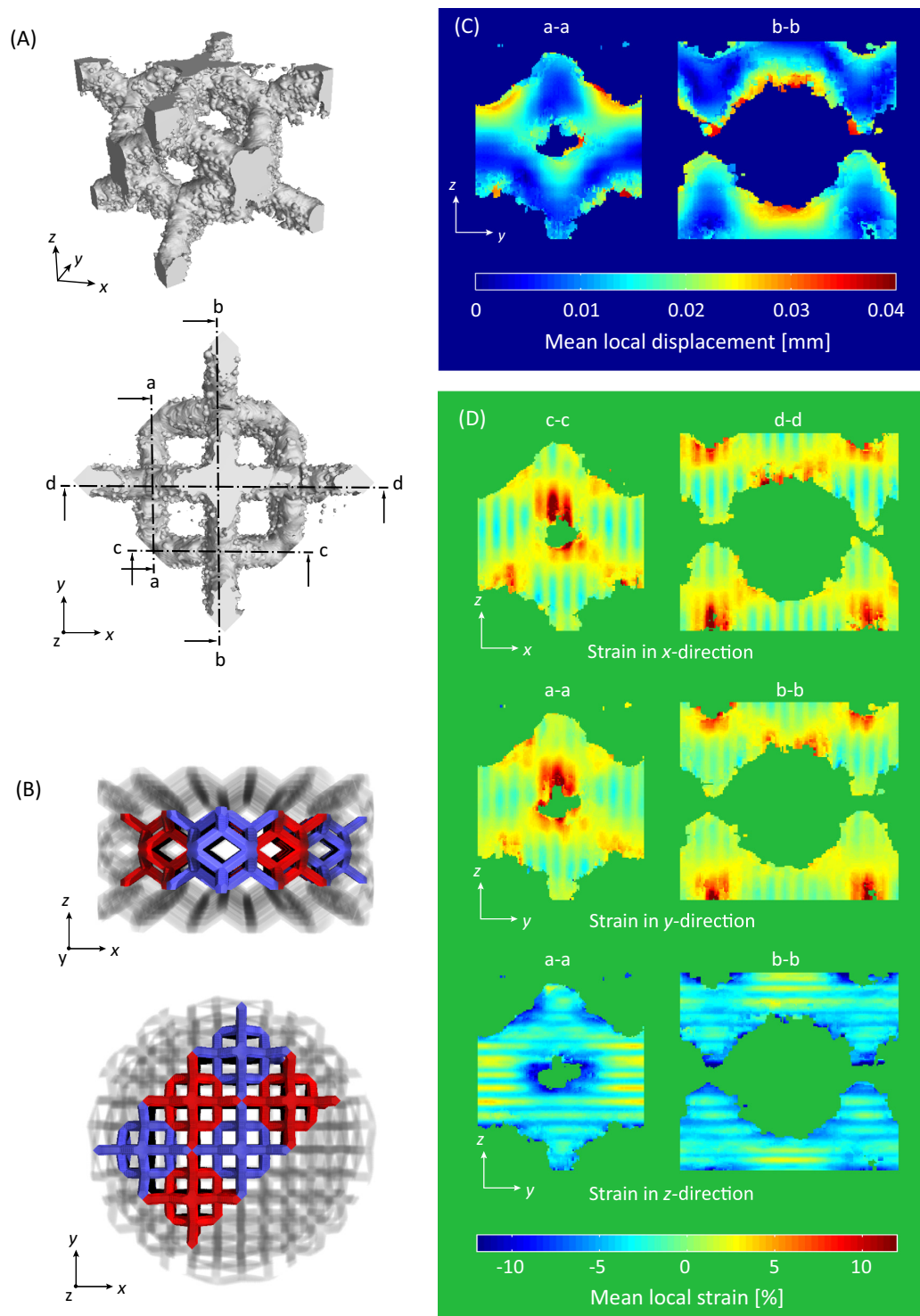
Fig. 5. (A) A 3-D rendering of one selected unit cell with dimensions ($2 \times 2 \times 2$) mm^3 of the materialized scaffold generated from tomography data. (B) A 3-D representation of the NiTi scaffold generated from the .stl-file. The six unit cells employed for averaging are highlighted in blue and red. (C) The mean local displacements owing to scaffold deformation in the averaged unit cell along two selected cross sections (see panel (B)), are symmetric with respect to the z axis, but asymmetric with respect to the x–y plane. (D) The mean local plane strains in the three orthogonal directions of the averaged unit cell are above zero (tensile strain) and below zero (compressive strain), depending on the location within the scaffold. The mean local strains around the holes in the rhombic faces reach values of up to 15%, i.e. they are about a factor of 2.5 higher than the integral scaffold deformation. The cross sections for visualization are indicated in panel (B).

Table 1

Average local displacements σ with standard deviations at five steps during the shape recovery for the bottom, center and top layer of unit cells as well as for the whole scaffold; one-way analysis of variance was performed for bottom, center and top layers; for each step, the mean values including their variances were statistically significant ($p < 0.001$).
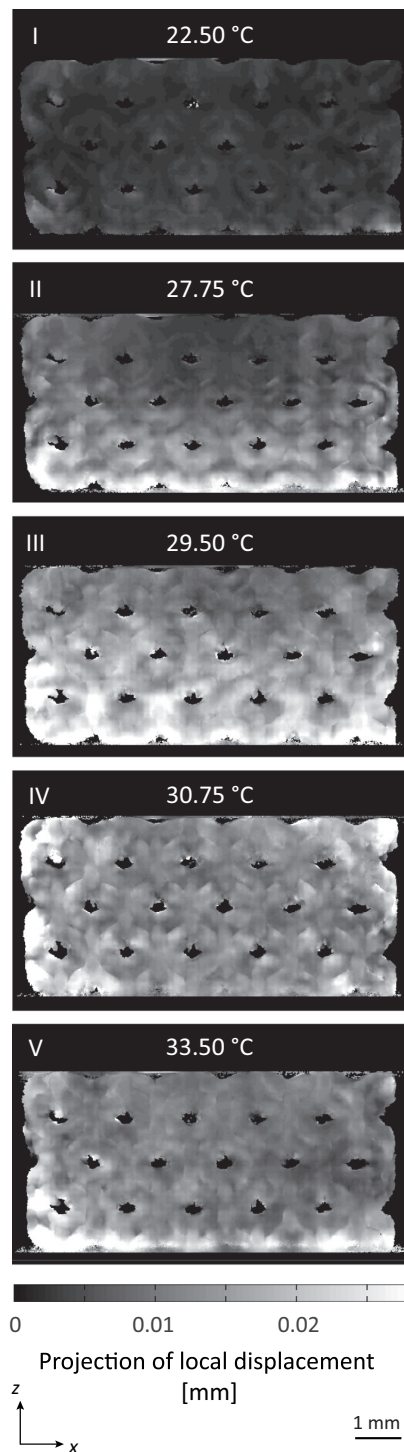
Step	Registered data sets	Temperature range (°C)	σ Bottom layer (μm)	σ Center layer (μm)	σ Top layer (μm)	σ Scaffold (μm)
I	#0 & #1	16.0–29.0	3.9 ± 2.3	3.2 ± 1.5	3.3 ± 1.9	3.6 ± 2.1
II	#1 & #2	24.5–31.0	13.2 ± 6.5	8.4 ± 4.4	6.1 ± 3.2	9.6 ± 6.2
III	#2 & #3	26.5–32.5	20.6 ± 8.5	16.0 ± 7.4	12.1 ± 6.3	16.2 ± 8.6
IV	#3 & #4	28.0–33.5	14.5 ± 7.1	13.3 ± 6.8	14.2 ± 8.0	14.3 ± 7.5
V	#4 & #5	30.5–36.5	13.9 ± 7.9	11.0 ± 5.3	11.2 ± 5.0	12.5 ± 6.7

established [38,41]. To the best of the authors' knowledge, this is currently the only approach to measuring displacements and strains for scaffolds of opaque materials such as NiTi locally in 3-D space. One study applied the approach to a polymer-based scaffold comprising irregularly arranged, rounded pores [45]. The present study relates to a metallic scaffold constructed from repeating unit cells, and quantitatively uncovers the strains and displacements within the 300-μm-thick scaffold struts. As the strain distribution is similar within the units, knowledge of local strain magnitudes and distribution should allow for the design optimization of the unit cell to optimize the mechanical stimuli for specific cell responses [2]. Such a design optimization is more difficult for scaffolds with random pore architectures. The present authors have not found any μCT studies that describe experiments on the shape recovery of NiTi-structures during continuous heating.
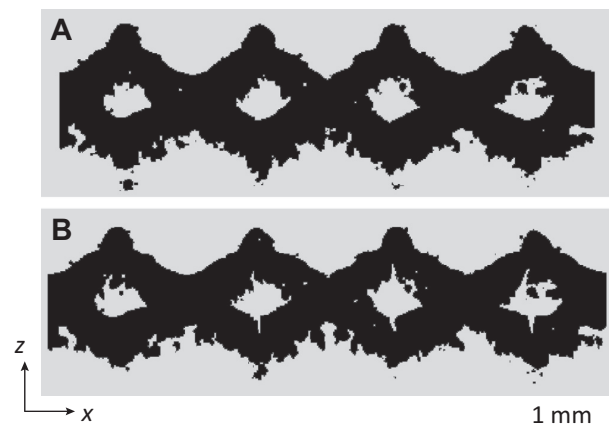
The deformation principles of the scaffold determined by FEM are validated by this experimental approach. The locations within the scaffold for maximal tensile and compressive strains are comparable. They occur in the edges of the rhombs oriented parallel to the deformation direction, i.e. the rhombs parallel to the z axis of the scaffold, and in the connections between two adjacent rhombs. In addition, the sizes of strain values are in the same order of magnitude. There are three main differences between simulation and experiment. First, the FEM simulations predicted identical deformation of the individual building units and symmetric deformation in comparable scaffold fractions. In contrast, the 3-D registration of the SRμCT data sets showed differences in displacement and strain fields between the basically identical and repeated building units. Geometrical deviations of the materialized scaffold from the computer-generated design are probably the main reason. Here, the use of the SRμCT data instead of the design file for FEM is beneficial, but was not part of this study. The deviations between design and actual scaffold shape are due to the SLM fabrication, as shown previously [16]. During manufacture, excess material is accumulated, especially on down-facing surfaces. This leads, on the one hand, to asymmetry regarding the upper and lower halves of individual units and the whole scaffold, respectively, while, on the other hand, deviations between the repeating units are caused. As variations were found in the local displacements and strains among the individual units, the mean local displacements and mean local strains were determined by averaging six centrally located individual cells. The mean local strains occurring in the averaged unit can be considered as symmetric regarding the locations, where tensile and compressive strains simultaneously occur. Nevertheless, the area for strain maxima along x and y above the opening in the rhomb in the upper half of the unit cell is considerably larger than the area below the opening in the rhomb. Second, a quantitative disparity was found concerning the maximal strain values obtained from the experimental data and FEM, as the maximal strain values determined by the 3-D registration were about a factor of two larger than the maximal strain values from the simulation. This was associated with the expanded area for tensile strains above the opening in the rhombs, as they can be attributed to

cracks present in the scaffold (cf., Fig. 7) presumably caused by multiple pseudoplastic deformations during the experimental procedure. In cyclic compression testing of such pseudoplastic SLM-built scaffolds, cracking of the struts could be observed as small kinks in the stress–strain curves between 8 and 11% global strain. As the scaffold was compressed ∼10% to induce a pseudoplastic deformation of 6%, cracks were probably induced. In tensile tests, the elongation at fracture refers to $(4.1 ± 0.5)$%. This was a lower limit, as the massive rods contained pores that promote crack initiation [46]. Upon scaffold compression and unloading, the cracks open in a tapered fashion (cf., Fig. 7B). After shape recovery and restoration of the scaffold's original shape, the cracks are closed. The voxel displacements from transforming the data set of the non-deformed scaffold into a compressed one regardless of the cracks give rise to increased strain. The cracks occur mainly in the upper part of the rhombs, which is linked again to the artifacts of SLM processing, as down-facing surfaces are much rougher than up-facing surfaces. As the inside of the upper half of the rhomb is facing down with respect to the SLM fabrication direction, crack initiation is preferred there owing to the notch effect of the irregular surface. Third, the regions for maximal strains are sharper in the FEM simulation than in the experimental data, where the areas of maximal strain appear more delocalized. This can also be attributed to the geometric deviations between the materialized scaffold and the scaffold model, as SLM leads to rounding of angles caused by discretizing the edges and therefore to a delocalized strain distribution within the real scaffold. In addition, shear deformation of the real scaffold might have played a role during deformation. In the simulation, two nodes at the base were laterally fixed to ensure compression as the sole deformation mode. In the experiment, the materialized scaffold was compressed between two coplanar plates, which may result in shearing of the scaffold during deformation. Another important reason for the generic discrepancies between model and experiment is the inhomogeneous material itself, since SLM causes an anisotropic microstructure, with grains elongated in the z direction and defects such as pores [16,26,47]. As the FEM model is based upon an isotropic, homogeneous material, material inhomogeneity and anisotropy are ignored. However, as the locations of maximal strain are geometry determined, the basic principles for the deformation are material independent.

By analysis of the strain distribution along three orthogonal axes of the averaged unit cell, mostly compressive strains were found along the z direction, and mostly tensile strains along the x and y directions. In regions of maxima, the strain rose to 15% for compression as well as for tension. As the integral scaffold deformation corresponded to 6%, the local strain is up to a factor of 2.5 higher than the global one. Compressive deformation of trabecular bone also leads to regions with larger local strains than the exerted one. However, the trabecular architecture shows shear bands due to compression with buckling and collapsing of small rods as a failure mechanism [48]. Investigations on porous calcium phosphate and glass scaffolds [49,50] subjected to compression revealed local strains of about a factor of two higher than the

Fig. 7. Parts of virtual cross sections of the scaffold prior (top) and subsequent (bottom) to deformation show the cracks caused by the local strains of up to 15%.

Fig. 6. Projections of the local displacement fields in a pseudoplastically deformed scaffold at five steps during the shape recovery process, i.e. during temperature increase. For each step, the median of the temperature interval covered is denoted. The shape recovery takes place heterogeneously. It starts at the bottom of the scaffold (I, II), followed by the outer regions (III, IV), before a relatively homogeneous shape recovery is reached (IV, V). The scaffold is mounted on the sample holder (diameter 4 mm) at its top.

integral scaffold deformation, although the geometry with irregularly interconnected pores of these scaffolds differs from the present lattice-based scaffold geometry.

Often, the deformation behavior of complex-shaped objects such as scaffolds is studied by FEM simulations, in which the model for the simulation is based on CT data [2,11,49–51]. The present authors chose another approach for two reasons. First, proper fine meshing of such a complex-shaped object with an irregular and rough surface is not trivial and time-consuming. Second, and even more important, a simulation cannot consider material anisotropies or artifacts including residual pores, both associated with the SLM fabrication of NiTi scaffolds [16,26].

Besides the analysis of the scaffold deformation upon compression, the shape recovery of the deformed scaffold during heating with variable-temperature SRμCT was analyzed. As the shape recovery process took place continuously, artifacts such as blurring due to the scaffold's shape recovery during the μCT measurements were present in the 3-D data sets. The maximal amount of blurring was determined by measuring the maximal pixel shift within 180° specimen rotation around the maximum of the shape recovery rate. The maximum pixel shift corresponded to (22 ± 3) pixels and was determined from two radiographs at the same viewing angles. This value consists of the pixel shift in the vertical and horizontal directions of the projections. Sinograms, however, would provide for the shift of pixels just along the horizontal direction, while the larger portion of the pixel shift occurring in the vertical direction would be neglected. Nevertheless, 3-D registration of the tomograms has proved to work well, if carried out with segmented data taking into account the conservation of the mass of the scaffold [16]. Regarding the shape memory effect of the scaffold, a complete shape recovery of the specimen in the x–y as well as the z direction was found by measuring the height and diameter with a slide gauge with an accuracy of 0.01 mm.

The temporal and local evaluation of the shape memory effect revealed a heterogeneous evolution of the shape recovery, starting from the bottom of the scaffold. This observed sequence of the shape recovery might have been caused by the experimental setup, as the metallic sample holder on top of the scaffold could have led to a temperature gradient in its proximity. Still, since the present study was worked near room temperature and with a reasonably small heating rate, temperature gradients should be less dominant. A similar effect, however, was recently reported by Watkins et al.

[52], who investigated the shape recovery process of a two-dimensional honeycomb NiTi structure. In image II of Fig. 6, a feature related to relatively small local displacements occurs in the central zone of the scaffold directly underneath the specimen holder. One could expect that the rigid fixation of the scaffold on the holder caused the reduced values for displacement, as the fixation hindered deformations of the struts.

For repeated mechanical stimulation of cells, pseudoelasticity and the two-way shape memory effect could be employed. In this study, however, a pseudoplastic effect was selected. The present findings regarding the localization and distribution of displacements and strains upon compression of the pseudoplastic scaffold can predict the pseudoelastic ones, since the local strain distribution depends mainly on the scaffold's geometry.

The one-way shape memory effect could be employed in scaffolds to enhance the primary fixation, improving a press-fit, as heating of the compressed device above A_f leads to its expansion upon implantation.

The registration regarding the scaffold compression was repeated, applying the SRµCT data set of the initial, non-deformed and the compressed scaffold (data set #0). The occurrence and distribution of local displacements and strains within the scaffold is analogous to the local displacements, which have been found applying the data sets of the scaffold after completed shape recovered (data set #5) and after compression (data set #0). Therefore, applying the data sets obtained at the beginning and at the end of the shape recovery process is reasonable to also investigate the scaffold compression process. To compare the (temporal) process of scaffold compression and shape recovery, one would have to collect several data sets at different stages during the compression process, involving an in situ compression device in the experimental setup, as used by Madi et al. [45].

Actual compressive strains occurring in bone in a physiological situation during physical activity are referred to be between 0.004 and 0.320% [53–55]. For intramembranous bone formation within scaffolds, however, compressive or tensile strains ranging from 0.5 to 1.5% are usually proposed [2,11–13]. Mechanical stimuli in the strain range of 15% are favorable if the endochondral ossification route is pursued [44]. As strains of up to 15% were detected around the opening in the rhombs, while the bows above and underneath the center of the unit cell (Fig. 5D, cross sections b–b and d–d) showed strain values between 1 and 5%, the combination of small (<5%) and moderate strain ranges (<15%) might lead to a combined ossification process with intramembranous bone tissue in the vicinity of the bows and endochondral tissue along the struts.

As SRµCT combined with 3-D registration gives insight into the local strain distribution and allows for an approximation of the relation between integral and actual local strains, the approach presented enables investigation of local displacements and strains upon deformation in scaffolds and other porous biomaterials with even more complex architectures. For example, the local deformation behavior of CaP-based scaffolds and polyurethane-based scaffolds, both applied for mechanical cell stimulation [6,56,57], could be investigated with an in situ mechanical deformation device incorporated in the experimental setup [45]. If a polymer-based and cell-seeded scaffold was investigated with such a setup, it should also become possible to directly measure the local strains acting on the cell assemblage during mechanical stimulation of the scaffold. The cells would, however, have to be stained prior to the µCT investigation (e.g. with osmium tetroxide) in order to increase their absorption coefficient [58]. One could further imagine local and temporal study of cell-mediated scaffold shrinkage, which is undesirable, but often associated with collagen-based scaffolds [59].

5. Conclusions

The present study presents an approach to measuring local displacements and strains within complex-shaped scaffold architectures upon deformation by SRµCT, in combination with non-rigid 3-D registration. Compressive deformation of a pseudoplastic NiTi scaffold and the one-way shape memory effect were analyzed. The latter was resolved locally and temporally during scaffold heating at a rate of $4\,K\,h^{-1}$. The integral scaffold compression of ~6% led to local strains of up to 15%, while tensile and compressive strains occurred simultaneously. The shape recovery process started from the bottom of the scaffold and proceeded towards the scaffold top. Principles for the deformation derived from FEM simulations were verified. Deviations between both techniques can be attributed mainly to deviations in geometry and inhomogeneous material properties, both the result of SLM processing. In contrast to FEM, the SRµCT-based approach also incorporates geometric irregularities and material inhomogeneity. The data will help in understanding how mechanical stimuli act on cells within porous 3-D scaffolds and therefore support scaffold design and loading-range optimization of implants with enhanced osteoinductivity.

Acknowledgements

Appendix Figures. with essential colour discrimination

Certain figures in this article, particularly Figs. 2–5, are difficult to interpret in black and white. The full colour images can be found in the on-line version, at doi: 10.1016/j.actbio.2013.11.007.

References

[1] Prendergast PJ, Huiskes R, Soballe K. Biophysical stimuli on cells during tissue differentiation at implant interfaces. J Biomech 1997;30(6):539–48.

[2] Stops AJF, Heraty KB, Browne M, O'Brien FJ, McHugh PE. A prediction of cell differentiation and proliferation within a collagen–glycosaminoglycan scaffold subjected to mechanical strain and perfusive fluid flow. J Biomech 2010;43(4):618–26.

[3] Byrne EM, Farrell E, McMahon LA, Haugh MG, O'Brien FJ, Campbell VA, et al. Gene expression by marrow stromal cells in a porous collagen–glycosaminoglycan scaffold is affected by pore size and mechanical stimulation. J Mater Sci Mater Med 2008;19:3455–63.

[4] McMahon LA, Reid AJ, Campbell VA, Prendergast PJ. Regulatory effects of mechanical strain on the chondrogenic differentiation of MSCs in a collagen–GAG scaffold: experimental and computational analysis. Ann Biomed Eng 2008;36(2):185–94.

[5] Lambers FM, Schulte FA, Kuhn G, Webster DJ, Müller R. Mouse tail vertebrae adapt to cyclic mechanical loading by increasing bone formation rate and decreasing bone resorption rate as shown by time-lapsed in vivo imaging of dynamic bone morphometry. Bone 2011;49:1340–50.

[6] Roshan-Ghias A, Lambers FM, Gholam-Rezaee M, Mueller R, Pioletti DP. In vivo loading increases mechanical properties of scaffold by affecting bone formation and bone resorption rates. Bone 2011;49(6):1357–64.

[7] Long JP, Hollister SJ, Goldstein SA. A paradigm for the development and evaluation of novel implant topologies for bone fixation: in vivo evaluation. J Biomech 2012;45(15):2651–7.

[8] Wazen RM, Currey JA, Guo H, Brunski JB, Helms JA, Nanci A. Micromotion-induced strain fields influence early stages of repair at bone–implant interfaces. Acta Biomater 2013;9:6663–74.

[9] Rath B, Nam J, Knobloch TJ, Lannutti JJ, Agarwal S. Compressive forces induce osteogenic gene expression in calvarial osteoblasts. J Biomech 2008;41(5):1095–103.

[10] Meyer U, Buchter A, Nazer N, Wiesmann HP. Design and performance of a bioreactor system for mechanically promoted three-dimensional tissue engineering. Brit J Oral Max Surg 2006;44(2):134–40.

[11] Sandino C, Lacroix D. A dynamical study of the mechanical stimuli and tissue differentiation within a CaP scaffold based on micro-CT finite element models. Biomech Model Mechanobiol 2011;10:565–76.

[12] Milan J-L, Planell JA, Lacroix D. Simulation of bone tissue formation within a porous scaffold under dynamic compression. Biomech Model Mechanobiol 2010;9:583–96.

[13] Bölgen N, Yang Y, Korkusuz P, Güzel E, El Haj AJ, Piskin E. Three-dimensional ingrowth of bone cells within biodegradable cryogel scaffolds in bioreactors at different regimes. Tissue Eng A 2008;14(10):1743–50.

[14] Alvarez K, Nakajima H. Metallic scaffolds for bone regeneration. Materials 2009;2(3):790–832.

[15] Bansiddhi A, Sargent TD, Stupp SI, Dunand DC. Porous NiTi for bone implants: a review. Acta Biomater 2008;4(4):773–82.

[16] Bormann T, de Wild M, Beckmann F, Müller B. Assessing the morphology of selective laser melted NiTi-scaffolds for a three-dimensional quantification of the one-way shape memory effect. Proc SPIE 2013;8689:868914.

[17] Liu X, Wu S, Yeung KWK, Chan YL, Hu T, Xu Z, et al. Relationship between osseointegration and superelastic biomechanics in porous NiTi scaffolds. Biomaterials 2011;32(2):330–8.

[18] Gotman I, Ben-David D, Unger RE, Böse T, Gutmanas EY, Kirkpatrick CJ. Mesenchymal stem cell proliferation and differentiation on load-bearing trabecular Nitinol scaffolds. Acta Biomater 2013;9(9):8440–8.

[19] Bansiddhi A, Dunand DC. Shape-memory NiTi foams produced by replication of NaCl space-holders. Acta Biomater 2008;4(6):1996–2007.

[20] Bram M, Köhl M, Buchkremer HP, Stöver D. Mechanical properties of highly porous NiTi alloys. J Mater Eng Perform 2011;20(4–5):522–8.

[21] Köhl M, Bram M, Moser A, Buchkremer HP, Beck T, Stöver D. Characterization of porous, net-shaped NiTi alloy regarding its damping and energy-absorbing capacity. Mater Sci Eng, A 2011;528(6):2454–62.

[22] Bram M, Bitzer M, Buchkremer H, Stöver D. Reproducibility study of NiTi parts made by metal injection molding. J Mater Eng Perform 2012;21(12):2701–12.

[23] Li BY, Rong LJ, Li YY, Gjunter VE. Synthesis of porous NiTi shape-memory alloys by self-propagating high-temperature synthesis: reaction mechanism and anisotropy in pore structure. Acta Mater 2000;48(15):3895–904.

[24] Kaya M, Orhan N, Tosun G. The effect of the combustion channels on the compressive strength of porous NiTi shape memory alloy fabricated by SHS as implant material. Curr Opin Solid State Mater 2010;14(1):21–5.

[25] Wisutmethangoon S, Denmud N, Sikong L. Characteristics and compressive properties of porous NiTi alloy synthesized by SHS technique. Mater Sci Eng, A 2009;515:93–7.

[26] Bormann T, Schumacher R, Müller B, Mertmann M, de Wild M. Tailoring selective laser melting process parameters for NiTi implants. J Mater Eng Perform 2012;21(12):2519–24.

[27] Habijan T, Haberland C, Meier H, Frenzel J, Wittsiepe J, Wuwer C, et al. The biocompatibility of dense and porous nickel–titanium produced by selective laser melting. Mater Sci Eng, C 2013;33(1):419–26.

[28] van Bael S, Chai YC, Truscello S, Moesen M, Kerckhofs G, van Oosterwyck H, et al. The effect of pore geometry on the in vitro biological behavior of human periosteum-derived cells seeded on selective laser-melted Ti6Al4V bone scaffolds. Acta Biomater 2012;8:2824–34.

[29] Sobral JM, Caridade SG, Sousa RA, Mano JF, Reis RL. Three-dimensional plotted scaffolds with controlled pore size gradients: effect of scaffold geometry on mechanical performance and cell seeding efficiency. Acta Biomater 2011;7:1009–18.

[30] Frenzel J, George EP, Dlouhy A, Somsen C, Wagner MF-X, Eggeler G. Influence of Ni on martensitic phase transformations in NiTi shape memory alloys. Acta Mater 2010;58:3444–58.

[31] Bormann T. Structure and thermomechanics of selective laser melted nickel–titanium. Basel, Switzerland: Biomaterials Science Center, University of Basel; 2013.

[32] Roh J-H, Bae J-S. Thermomechanical behaviors of Ni–Ti shape memory alloy ribbons and their numerical modeling. Mech Mater 2010;42(8):757–73.

[33] van Humbeeck J, Stalmans R, Besselink PA. Shape memory alloys. In: Helsen JA, Breme HJ, editors. Metals as Biomaterials. John Wiley & Sons; 1998. p. 80.

[34] Beckmann F, Herzen J, Haibel A, Müller B, Schreyer A. High density resolution in synchrotron-radiation-based attenuation-contrast microtomography. Proc SPIE 2008;7078:70781D.

[35] Müller B, Thurner P, Beckmann F, Weitkamp T, Rau C, Bernhardt R, et al. Three-dimensional evaluation of biocompatible materials by microtomography using synchrotron radiation. Proc SPIE 2002;4503:178–88.

[36] Kak AC, Slaney M. Principles of computerized tomographic imaging. New York: IEEE Press; 1988.

[37] Thurner PJ, Beckmann F, Müller B. An optimization procedure for spatial and density resolution in hard X-ray micro computed tomography. Nucl Instrum Methods B 2004;225:599–603.

[38] Müller B, Deyhle H, Lang S, Schulz G, Bormann T, Fierz F, et al. Three-dimensional registration of tomography data for quantification in biomaterials science. Int J Mater Res 2012;103(2):242–9.

[39] Bormann T, Friess S, de Wild M, Schumacher R, Schulz G, Müller B. Determination of strain fields in porous shape memory alloys using micro computed tomography. Proc SPIE 2010;7804:78041M.

[40] Liu L, Morgan EF. Accuracy and precision of digital volume correlation in quantifying displacements and strains in trabecular bone. J Biomech 2007;40(15):3516–20.

[41] Schulz G, Crooijmans HJA, Germann M, Scheffler K, Müller-Gerbl M, Müller B. Three-dimensional strain fields in human brain resulting from formalin fixation. J Neurosci Meth 2011;202:17–27.

[42] Andronache A, von Siebenthal M, Szekely G, Cattin P. Non-rigid registration of multi-modal images using both mutual information and cross-correlation. Med Image Anal 2008;12:3–15.

[43] Babaee S, Jahromi BH, Ajdari A, Nayeb-Hashemi H, Vaziri A. Mechanical properties of open-cell rhombic dodecahedron cellular structures. Acta Mater 2012;60:2873–85.

[44] Claes LE, Heigele CA. Magnitudes of local stress and strain along bony surfaces predict the course and type of fracture healing. J Biomech 1999;32(3):255–66.

[45] Madi K, Tozzi G, Zhang QH, Tong J, Cossey A, Au A, et al. Computation of full-field displacements in a scaffold implant using digital volume correlation and finite element analysis. Med Eng Phys 2013;35(9):1298–312.

[46] Howald C. Institute for medical and analytical technologies. Muttenz: University of Applied Sciences; Unpublished data.

[47] Thijs L, Verhaeghe F, Craeghs T, Humbeeck JV, Kruth J-P. A study of the microstructural evolution during selective laser melting of Ti–6Al–4V. Acta Mater 2009;58(9):3303–12.

[48] Nazarian A, Müller R. Time-lapsed microstructural imaging of bone failure behavior. J Biomech 2004;37:55–65.

[49] Lacroix D, Chateau A, Ginebra M-P, Planell JA. Micro-finite element models of bone tissue-engineering scaffolds. Biomaterials 2006;27(30):5326–34.

[50] Sandino C, Planell JA, Lacroix D. A finite element study of mechanical stimuli in scaffolds for bone tissue engineering. J Biomech 2008;41:1005–14.

[51] Milan J-L, Planell JA, Lacroix D. Computational modelling of the mechanical environment of osteogenesis within a polylactic acid–calcium phosphate glass scaffold. Biomaterials 2009;40:4219–26.

[52] Watkins RT, Shaw JA, Grummon DS. Shape memory thermal lag and superelastic rate sensitivity of SMA cellular structures. Proc SPIE 2013;8689:86890R.

[53] Burr DB, Milgrom C, Fyhrie D, Forwood M, Nyska M, Finestone A, et al. In vivo measurement of human tibial strains during vigorous activity. Bone 1997;18(5):405–10.

[54] Milgrom C, Simkin A, Eldad A, Nyska M, Finestone A. Using bone's adaptation ability to lower the incidence of stress fractures. Am J Sport Med 2000;28(2):245–51.

[55] Yang PF, Brüggemann G-P, Rittweger J. What do we currently know from in vivo bone strain measurements in humans? J Musculoskel Neuron 2011;11(1):8–20.

[56] Sharifpoor S, Simmons CA, Labow RS, Santerre JP. A study of vascular smooth muscle cell function under cyclic mechanical loading in a polyurethane scaffold with optimized porosity. Acta Biomater 2010;6(11):4218–28.

[57] Liu C, Abedian R, Meister R, Haasper C, Hurschler C, Krettek C, et al. Influence of perfusion and compression on the proliferation and differentiation of bone mesenchymal stromal cells seeded on polyurethane scaffolds. Biomaterials 2012;33(4):1052–64.

[58] Thurner P, Müller B, Beckmann F, Weitkamp T, Rau C, Müller R, et al. Tomography studies of human foreskin fibroblasts on polymer yarns. Nucl Instrum Methods B 2003;200:397–405.

[59] Engelhardt E-M, Micol LA, Houis S, Wurm FM, Hilborn J, Hubbell JA, et al. A collagen–poly(lactic acid-co-ε-caprolactone) hybrid scaffold for bladder tissue regeneration. Biomaterials 2011;32(16):3969–76.

3 Conclusions

Selective laser melting allows fabricating NiTi parts with functional pseudoelastic and pseudoplastic properties.

The phase transformation temperatures can be shifted during the processing towards higher temperature values. The shift is induced by a preferential evaporation of Ni during the processing and it allows for the fabrication of NiTi entities with either pseudoelastic or pseudoplastic properties for example at room or body temperature from the same lot of powder.

The process parameters laser power and scanning speed impact the resulting material properties in a distinct manner. The scanning speed determines the amount of evaporated Ni, i.e. with an extension of the laser irradiation the amount of evaporated Ni increases. The laser power on the other hand impacts the microstructure of NiTi. With the laser power, the grain size increases about a factor of three for grain width and about a factor of ten for grain length. In addition, a preferred <111> orientation of crystallites parallel to the building direction evolves and further increase with the laser power.

The grain size increases until the grains reach a maximum width, which is defined by the distance of the laser scanning paths.

The increase in grain size occurs due to Ostwald-ripening of the crystallites during the SLM process. The Ostwald-ripening process can be assessed from the shape of the size distribution, as it exhibits a characteristic negative skew towards smaller crystallite sizes.

If the processing parameters are selected properly, NiTi parts in accordance to the ASTM2063-05 can fabricated by selective laser melting. In order to fully meet the requirements, the oxygen contents have to be reduced in the future.

Porous shape memory scaffolds built by selective laser melting meet the demands of a compression bio-reactor system. The (future) investigations *in-vivo* and *in-vitro* will reveal the potential of NiTi-scaffolds for mechanical tissue stimulation.

The uniaxial compression of scaffolds results in simultaneously occurring local compressive and tensile strains. The local strains exceed the actual induced overall scaffold deformation about a factor of 2.5. The local strains and displacements can be quantified and visualized by three-dimensional non-rigid registration of micro-computed tomography data comprising data sets of the scaffold in deformed and initial state.

Synchrotron-radiation based micro-computed tomography in combination with a setup for temperature variation allows the continuous data acquisition during the heating-induced shape recovery process of a pseudoplastic scaffold. From the continuous recorded radiographs, individual data sets referring to several stages of the shape recovery can be reconstructed despite the slight movement of the scaffold during data recording. Three-dimensional non-rigid data registration reveals a locally heterogeneous shape recovery. It proceeds from the scaffolds bottom towards the top and terminates at the scaffolds periphery.

Bibliography

[1] Elahinia M.H., Hashemi M., Tabesh M., Bhaduri S.B.: Manufacturing and processing of NiTi implants: A review. Prog Mater Sci 57(5) (2011) 911-46.

[2] Wen C.E., Xiong J.Y., Li Y.C., Hodgson P.D.: Porous shape memory alloy scaffolds for biomedical applications: A review. Physica Scripta (T139) (2010) 014070.

[3] Bansiddhi A., Sargeant T.D., Stupp S.I., Dunand D.C.: Porous NiTi for bone implants: A review. Acta Biomater 4(4) (2008) 773-82.

[4] Wagner M.F.X., Windl W.: Lattice stability, elastic constants and macroscopic moduli of NiTi martensites from first principles. Acta Mater 56 (2008) 6232-45.

[5] Fung Y.C.: Biomechanics - Mechanical Properties of Living Tissues, second ed. New York: Springer-Verlag Inc. (1993).

[6] Köhl M., Bram M., Moser A., Buchkremer H.P., Beck T., Stöver D.: Characterization of porous, net-shaped NiTi alloy regarding its damping and energy-absorbing capacity. Mater Sci Eng A-Struct 528(6) (2011) 2454-62.

[7] Otsuka K., Ren X.: Physical metallurgy of TiNi-based shape memory alloys. Prog Mater Sci 50 (2005) 511678.

[8] Duerig T.W., Pelton A.R.: Materials properties handbook: Titanium alloys. Materials Park, OH: ASM International (1994).

[9] Liu Y., Xiang H.: Apparent modulus of elasticity of near-equiatomic NiTi. J Alloy Compd 270 (1998) 154-59.

[10] Rajagopalan S., Little A.L.: Elastic modulus of shape-memory NiTi from in situ neutron diffraction during macroscopic loading,

instrumented indentation, and extensometry. Appl Phys Lett 86 (2005) 081901.

[11] van Humbeeck J., Stalmans R., Besselink P.A.: Shape memory alloys. In: Helsen JA, Breme HJ, editors. Metals as Biomaterials. John Wiley & Sons (1998).

[12] Kaack M.: Elastische Eigenschaften von NiTi-Formgedächtnis-Legierungen. Fakultät für Physik und Astronomie. Bochum: Ruhr-Universität Bochum (2002).

[13] Mullen L., Stamp R.C., Brooks W.K., Jones E., Sutcliffe C.J.: Selective laser melting: A regular unit cell approach for the manufacture of porous, titanium, bone in-growth constructs, suitable for orthopedic applications. J Biomed Mater Res B 89(2) (2009) 325-34.

[14] Tolosa I., Garciandia F., Zubiri F., Zapirain F., Esnaola A.: Study of mechanical properties of AISI 316 stainless steel processed by selective laser melting, following different manufacturing strategies. Int J Adv Manuf Technol 51 (2010) 639-47.

[15] Pattanayak D.K., Fukuda A., Matsushita T., Takemoto M., Fujibayashi S., Sasaki K., Nishida N., Nakamura T., Kokubo T.: Bioactive Ti metal analogous to human cancellous bone: Fabrication by selective laser melting and chemical treatments. Acta Biomater 7(3) (2010) 1398-406.

[16] Murr L.E., Esquivel E.V., Quinones S.A., Gaytan S.M., Lopez M.I., Martinez E.Y., Medina F., Hernandez D.H., Martinez E., Martinez J.L., Stafford S.W., Brown D.K., Hoppe T., Meyers W., Lindhe U., Wicker R.B.: Microstructures and mechanical properties of electron beam-rapid manufactured Ti-6Al-4V biomedical prototypes compared to wrought Ti-6Al-4V. Mater Charact 60(2) (2009) 96-105.

[17] Vandenbroucke B., Kruth J.-P.: Selective laser melting of biocompatible metals for rapid manufacturing of medical parts. Rapid Prototyping J 13(4) (2007) 196-203.

[18] Fukuda A., Takemoto M., Saito T., Fujibayashi S., Neo M., Pattanayak D.K., Matsushita T., Sasaki K., Nishida N., Kokubo T.,

Nakamura T.: Osteoinduction of porous Ti implants with a channel structure fabricated by selective laser melting. Acta Biomater 7 (2001) 2327-36.

[19] Thijs L., Verhaeghe F., Craeghs T., Humbeeck J.V., Kruth J.-P.: A study of the microstructural evolution during selective laser melting of Ti-6Al-4V. Acta Mater 58(9) (2010) 3303-12.

[20] Murr L.E., Martinez E., Pan X.M., Gaytan S.M., Castro J.A., Terrazas C.A., Medina F., Wicker R.B., Abbott D.H.: Microstructures of Rene 142 nickel-based superalloy fabricated by electron beam melting. Acta Mater 61(11) (2013) 4289-96.

[21] Thijs L., Montero Sistiaga M.L., Wauthle R., Xie Q., Kruth J.-P., van Humbeeck J.: Strong morphological and crystallographic texture and resulting yield strength anisotropy in selective laser melted tantalum. Acta Mater 61(12) (2013) 4657-68.

[22] Chlebus E., Kuznicka B., Kurzynowski T., Dybala B.: Microstructure and mechanical behaviour of Ti-6Al-7Nb alloy produced by selective laser melting. Mater Charact 62(5) (2011) 488-95.

[23] Yadroitsev I., Krakhmalev P., Yadroitsava I., Johansson S., Smurov I.: Energy input effect on morphology and microstructure of selective laser melting single track from metallic powder. J Mater Process Tech 213 (2013) 606-13.

[24] Frenzel J., George E.P., Dlouhy A., Somsen C., Wagner M.F.-X., Eggeler G.: Influence of Ni on martensitic phase transformations in NiTi shape memory alloys. Acta Mater 58 (2010) 3444-58.

[25] Allafi J.K.: Mikrostrukturelle Untersuchungen zum Einfluss von thermomechanischen Behandlungen auf die martensitischen Phasenumwandlungen an einer Ni-reichen NiTi-Formgedächtnislegierung. Bochum: Ruhr-Universität Bochum (2002).

[26] Zhou N., Shen C., Wagner M.F.X., Eggeler G., Mills M.J., Wang Y.: Effect of Ni4Ti3 precipitation on martensitic transformation in Ti-Ni. Acta Mater 58(20) (2010) 6685-94.

[27] Haberland C.: Additive Verarbeitung von NiTi-Formgedächtnis-werkstoffen mittels Selective Laser Melting. Fakultät für Maschinenbau. Bochum: Ruhr-Universität Bochum (2012).

[28] Dudziak S.: Beeinflussung der funktionellen Eigenschaften aktorische Nickel-Titan-Legierungen durch die aktiven Parameter im Mikrolaserschmelzprozess. Fakultät für Maschinenbau. Hannover: Universität Hannover (2012).

[29] Dudziak S., Gieseke M., Haferkamp H., Barcikowski S., Kracht D.: Functionality of laser-sintered shape memory micro-actuators. Proceedings of the Lane Part 2(5) (2010) 607-15.

[30] Meier H., Haberland C., Frenzel J.: Structural and functional properties of NiTi shape memory alloy produced by selective laser melting. In: Innovative Developments in Design and Manufacturing: Advanced Research in Virtual and Rapid Prototyping. Boca Raton: CRC Press-Taylor Francis Group (2012) 291-96.

[31] Habijan T., Haberland C., Meier H., Frenzel J., Wittsiepe J., Wuwer C., Greulich C., Schildhauer T.A., Köller M.: The biocompatibility of dense and porous Nickel-Titanium produced by selective laser melting. Mat Sci Eng C-Mater 33(1) (2013) 419-26.

[32] Bormann T., Schumacher R., Müller B., Mertmann M., de Wild M.: Tailoring selective laser melting process parameters for NiTi implants. J Mater Eng Perfom 21(12) (2012) 2519-24.

[33] Stops A.J.F., Heraty K.B., Browne M., O'Brien F.J., McHugh P.E.: A prediction of cell differentiation and proliferation within a collagen-glycosaminoglycan scaffold subjected to mechanical strain and perfusive fluid flow. J Biomech 43(4) (2010) 618-26.

[34] Byrne E.M., Farrell E., McMahon L.A., Haugh M.G., OBrien F.J., Campbell V.A., Prendergast P.J., OConnell B.C.: Gene expression by marrow stromal cells in a porous collagenglycosaminoglycan scaffold is affected by pore size and mechanical stimulation. J Mater Sci Mater Med 19 (2008) 3455-63.

[35] Lambers F.M., Schulte F.A., Kuhn G., Webster D.J., Müller R.: Mouse tail vertebrae adapt to cyclic mechanical loading by increasing bone formation rate and decreasing bone resorption rate as

shown by time-lapsed in vivo imaging of dynamic bone morphometry. Bone 49 (2011) 1340-50.

[36] Roshan-Ghias A., Lambers F.M., Gholam-Rezaee M., Mueller R., Pioletti D.P.: In vivo loading increases mechanical properties of scaffold by affecting bone formation and bone resorption rates. Bone 49(6) (2011) 1357-64.

[37] Long J.P., Hollister S.J., Goldstein S.A.: A paradigm for the development and evaluation of novel implant topologies for bone fixation: In vivo evaluation. J Biomech 45(15) (2012) 2651-57.

[38] Wazen R.M., Currey J.A., Guo H., Brunski J.B., Helms J.A., Nanci A.: Micromotion-induced strain fields influence early stages of repair at boneimplant interfaces. Acta Biomater 9 (2013) 6663-74.

[39] Habijan T., Glogowski T., Kühn S., Pohl M., Wittsiepe J., Greulich C., Eggeler G., Schildhauer T.A., Köller M.: Can human mesenchymal stem cells survive on a NiTi implant material subjected to cyclic loading? Acta Biomater 7(6) (2011) 2733-39.

Acknowledgements

First of all, I want to thank my supervisors Bert Müller and Michael de Wild. Thanks a lot for giving me the opportunity to do this work! Thank you for the continuous support, guidance and the invaluable discussions throughout the last years. I really learned a lot! And special thanks for your dedication and help in this very last week before submitting the thesis!

Martin Bram and Thomas Jung, thank you for acting as co-referees and for evaluating this work.

Ralf Schumacher, thanks a lot for introducing me to selective laser melting and for all the support regarding technical problems with the *small SLM.*

Felix Beckmann, thanks for supporting all beamtimes at the DESY in Hamburg and the related data with expertise and practical advice.

Georg Schulz and Hans Dehyle, many thanks for all your input and assistance, particularly (but not exclusively) regarding registration and Matlab! I also want to say thanks for the many laughter-ful lunch breaks. I very much enjoyed working with you.
This applies as well for all other colleagues from the BMC: Thanks for all discussions and the nice and fruitful working atmosphere!

The FH-team: It was a pleasure working with you! Thanks for all support especially in and around the work shop. Special thanks to Sandro Fabbri and Metthias Jeker for all practical help and debates.

Marcus Textor, thank you for supporting this work with the helpful advices, your time for discussions and motivation.

Peter Uggowitzer and Michael Schinhammer, thanks for your expertise regarding specific metal-related questions and the opportunity to carry out SEM and EBSD-investigations at the ETH Zürich.

Curriculum Vitae

Family Name: Bormann
First Name: Anna Therese
Citizenship: Germany
Date of Birth: 03.12.1982
Place of Birth: Erfurt, Germany

Education

2009-2013   Doctor of philosophy (PhD) in nanosciences,
University of Basel, Switzerland (Prof. B. Müller)
2003-2009   Diploma in materials sciences,
Martin-Luther-Universität Halle-Wittenberg, Germany
2001   University-entrance diploma,
Ratsgymnasium Erfurt, Germany

Professional Experience

2009-2013   PhD work at Biomaterials Science Center,
University of Basel, Switzerland;
University of applied Sciences Northwestern Switzerland,
School of Life Sciences, Muttenz, Switzerland
2009   Research assistant,
Fraunhofer-Institute for Mechanics of Materials,
Halle/Saale, Germany
2007-2008   Intern,
Aristotech Implant Technologies,
Luckenwalde, Germany